Defense Threat Reduction Agency
8725 John J. Kingman Road, MS 6201
Fort Belvoir, VA 22060-6201

TECHNICAL REPORT

Advanced Simulator Development for Power Flow and Sources

February 2006

Phil Spence, et al.

Prepared by:
Titian Corporation
2700 Merced Street
San Leandro, CA 94577-0599

DESTRUCTION NOTICE

FOR CLASSIFIED documents, follow the procedures in DoD 5550.22-M, National Industrial Security Program Operating Manual, Chapter 5, Section 7 (NISPOM) or DoD 5200.1-R, Information Security Program Regulation, Chapter 1X.

FOR UNCLASSIFIED limited documents, destroyed by any method that will prevent disclosure of contents or reconstruction of the document.

Retention of this document by DoD contractors is authorized in accordance with DoD 5220.22-M, Industrial Security Manual.

PLEASE NOTIFY THE DEFENSE THREAT REDUCTION AGENCY, ATTN: BDLMI, 8725 JOHN J. KINGMAN ROAD, MS-6201, FT BELVOIR, VA 22060-6201, IF YOUR ADDRESS IS INCORRECT, IF YOU WISH IT DELETED FROM THE DISTRIBUTION LIST, OR IF THE ADDRESSEE IS NO LONGER EMPLOYED BY YOUR ORGANIZATION.

DISTRIBUTION LIST UPDATE

This mailer is provided to enable DTRA to maintain current distribution lists for reports. (We would appreciate you providing the requested information.)

- ☐ Add the individual listed to your distribution list.

- ☐ Delete the cited organization/individual.

- ☐ Change of address.

> Note:
> Please return the mailing label from the document so that any additions, changes, corrections or deletions can be made easily. For distribution cancellation or more information call DTRA/BDLMI (703) 767-4725.

NAME: _____

ORGANIZATION: _____

OLD ADDRESS	**NEW ADDRESS**
_____	_____
_____	_____
_____	_____

TELEPHONE NUMBER: (   ) _____

DTRA PUBLICATION NUMBER/TITLE	**CHANGES/DELETIONS/ADDITONS, etc.** *(Attach Sheet if more Space is Required)*
_____	_____
_____	_____
_____	_____

DTRA or other GOVERNMENT CONTRACT NUMBER: _____

CERTIFICATION of NEED-TO-KNOW BY GOVERNMENT SPONSOR (if other than DTRA):

SPONSORING ORGANIZATION: _____

CONTRACTING OFFICER or REPRESENTATIVE: _____

SIGNATURE: _____

DEFENSE THREAT REDUCTION AGENCY
ATTN: BDLMI
8725 John J Kingman Road, MS 6201
Fort Belvoir, VA 22060-6201

REPORT DOCUMENTATION PAGE

Public reporting burden for this collection of information is estimated to average 1 hour per response, including the time for reviewing instructions, searching existing data sources, gathering and maintaining the data needed, and completing and reviewing the collection of information. Send comments regarding this burden, estimate or any other aspect of this collection of information, including suggestions for reducing this burden, to Washington Headquarters Services, Directorate for Information Operations and Reports, 1215 Jefferson Davis Highway, Suite 1204, Arlington, VA 22202-4302, and to the Office of Management and Budget, Paperwork Reduction Project (0704-0188), Washington, DC 20503.

1. AGENCY USE ONLY (Leave blank)	2. REPORT DATE 060200	3. REPORT TYPE AND DATES COVERED Technical – 150999 - 140900

4. TITLE AND SUBTITLE
Advanced Simulator Development for Power Flow and Sources

5. FINDING NUMBERS
C – DTRA 01-99-D-0042
PE - 0602715BR
PR – AB
TA – GE
WU - 00839

6. AUTHOR(S)
William Rix, Richard Miller, Peter Sincerny, Eduardo Waisman
Charles Gilbert, Phil Spence, Ian Smith, Pat Corcoran, Lee Schlitt

7. PERFORMING ORGANIZATION NAME(S) AND ADDRESS(ES)
Titan Corporation
2700 Merced Street
San Leandro, CA   94577-0599

8. PERFORMING ORGANIZATION REPORT NUMBER
MTSD300-356

9. SPONSORING/MONITORING AGENCY NAME(S) AND ADDRESS(ES)
Defense Threat Reduction Agency
8725 John J. Kingman Road, STOP-6201
Ft. Belvoir, VA 22060-6201

10. SPONSORING/MONITORING AGENCY REPORT NUMBER
DTRA-TR-01-3

11. SUPPLEMENTARY NOTES
This work was sponsored by the Defense Threat Reduction Agency RDT&E RMSS Codes B E61D D K112 BH AC 09870 25904D.

12a. DISTRIBUTION/AVAILABILITY STATEMENT
Approved for public release; distribution is unlimited

12b. DISTRIBUTION CODE

13. ABSTRACT (Maximum 200 words)
The objective of this effort was to identify, develop, and evaluate conceptual design options for an affordable full certification simulator. To limit the scope of our study, we focused on systems capable of delivering 400 kJ of krypton k-shell (~13 keV lines) radiation from imploding plasma radiation sources (PRS). We were primarily concerned with selecting pulsed power drivers and the associated pulsed power technology needed to drive PRS implosions of 100 and 250 ns at 30 to 60 MA levels. Our approach used a system analysis to locate stored energy minimums in the parameter space of driver $\sqrt{L \bullet C}$-time and vacuum inductance. We developed mechanical sketches of point designs for Marx Generator Driver and Linear Transformer Driver options that appear to be feasible with reasonable improvements in capacitor and switch components and vacuum power flow inductance. We recommend DTRA conduct an R&D Program to develop fast and ultra-fast drivers and minimize vacuum inductance. These developments could also enable beneficial upgrades to existing simulator facilities.

14. SUBJECT TERMS
Marx Generator Plasma Radiation Source   Pulsed Power Drivers
Plasma Radiation Source   Vacuum Power Flow

15. NUMBER OF PAGES 109

16. PRICE CODE

17. SECURITY CLASSIFICATION OF REPORT	18. SECURITY CLASSIFICATION OF THIS PAGE	19. SECURITY CLASSIFICATION OF ABSTRACT	20. LIMITATION OF ABSTRACT
UNCLASSIFIED	UNCLASSIFIED	UNCLASSIFIED	SAR

Standard Form 298 (Rev. 2-89)
Prescribed by ANSI Sta. 239-18
298-102

CONVERSION TABLE

Conversion Factors for U.S. Customary to metric (SI) units of measurement.

MULTIPLY ──────────────► BY ──────────────► TO GET

TO GET ◄────────────── BY ◄────────────── DIVIDE

angstrom	$1.000\ 000 \times E -10$	meters (m)
atmosphere (normal)	$1.013\ 25\ \times E +2$	kilo pascal (kPa)
bar	$1.000\ 000 \times E +2$	kilo pascal (kPa)
barn	$1.000\ 000 \times E -28$	meter^2 (m^2)
British thermal unit (thermochemical)	$1.054\ 350 \times E +3$	joule (J)
calorie (thermochemical)	$4.184\ 000$	joule (J)
cal (thermochemical/cm^2)	$4.184\ 000 \times E -2$	mega joule/m^2 (MJ/m^2)
curie	$3.700\ 000 \times E +1$	*giga bacquerel (GBq)
degree (angle)	$1.745\ 329 \times E -2$	radian (rad)
degree Fahrenheit	$t_k = (t°f + 459.67)/1.8$	degree kelvin (K)
electron volt	$1.602\ 19\ \times E -19$	joule (J)
erg	$1.000\ 000 \times E -7$	joule (J)
erg/second	$1.000\ 000 \times E -7$	watt (W)
foot	$3.048\ 000 \times E -1$	meter (m)
foot-pound-force	$1.355\ 818$	joule (J)
gallon (U.S. liquid)	$3.785\ 412 \times E -3$	meter^3 (m^3)
inch	$2.540\ 000 \times E -2$	meter (m)
jerk	$1.000\ 000 \times E +9$	joule (J)
joule/kilogram (J/kg) radiation dose absorbed	$1.000\ 000$	Gray (Gy)
kilotons	4.183	terajoules
kip (1000 lbf)	$4.448\ 222 \times E +3$	newton (N)
kip/inch^2 (ksi)	$6.894\ 757 \times E +3$	kilo pascal (kPa)
ktap	$1.000\ 000 \times E +2$	newton-second/m^2 (N-s/m^2)
micron	$1.000\ 000 \times E -6$	meter (m)
mil	$2.540\ 000 \times E -5$	meter (m)
mile (international)	$1.609\ 344 \times E +3$	meter (m)
ounce	$2.834\ 952 \times E -2$	kilogram (kg)
pound-force (lbs avoirdupois)	$4.448\ 222$	newton (N)
pound-force inch	$1.129\ 848 \times E -1$	newton-meter (N-m)
pound-force/inch	$1.751\ 268 \times E +2$	newton/meter (N/m)
pound-force/foot^2	$4.788\ 026 \times E -2$	kilo pascal (kPa)
pound-force/inch^2 (psi)	$6.894\ 757$	kilo pascal (kPa)
pound-mass (lbm avoirdupois)	$4.535\ 924 \times E -1$	kilogram (kg)
pound-mass-foot^2 (moment of inertia)	$4.214\ 011 \times E -2$	kilogram-meter^2 (kg-m^2)
pound-mass/foot^3	$1.601\ 846 \times E +1$	kilogram-meter^3 (kg/m^3)
rad (radiation dose absorbed)	$1.000\ 000 \times E -2$	**Gray (Gy)
roentgen	$2.579\ 760 \times E -4$	coulomb/kilogram (C/kg)
shake	$1.000\ 000 \times E -8$	second (s)
slug	$1.459\ 390 \times E +1$	kilogram (kg)
torr (mm Hg, 0° C)	$1.333\ 22\ \times E -1$	kilo pascal (kPa)

*The bacquerel (Bq) is the SI unit of radioactivity; 1 Bq = 1 event/s.
**The Gray (GY) is the SI unit of absorbed radiation.

TABLE OF CONTENTS

TABLE OF CONTENTS (Continued)

Figures

Figures (Continued)

Figures (Continued)

Figures (Continued)

Figures (Continued)

Tables

SECTION 1
OVERVIEW

This report presents the results of work completed under Contract DTRA01-99-D-0042, Delivery Order Number 2, entitled, "Power Flow Development For Advanced X-ray Simulation Capabilities." The objective of this effort was to identify, develop, and evaluate conceptual design options for an affordable full certification simulator. To simplify our scope, we focused on systems capable of delivering 400 kJ of krypton k-shell (~ 13 keV lines) radiation from imploding plasma radiation sources (PRS). We were primarily concerned with selecting pulsed power drivers and the associated pulsed power technology needed to drive PRS implosions of 100 and 250 ns at the 30 to 60 MA level.

Prior to commencing this effort, MPI had completed an IR&D funded concept study for a Next Generation Machine[1]. The concept developed is shown in Figure 1. We selected a four-modular source configuration to minimize cost for large dose X area products. Based upon simple scaling from existing pulsed power simulators, we assumed that we could achieve yields of 300 kJ of radiation between 1 to 13 keV from a 250 ns, 20 to 25 MA implosion. When our concept designs were translated into simple circuit models, we found that a direct-drive configuration using a fast Marx with an intrinsic $\sqrt{L \bullet C} = 300$ ns required about twice the stored energy as a configuration using the fast Marx and water-line pulse compression. The limited scope of the concept study raised many issues and motivated the broader approach undertaken in this effort to identify the most promising driver technologies for an affordable full certification simulator.
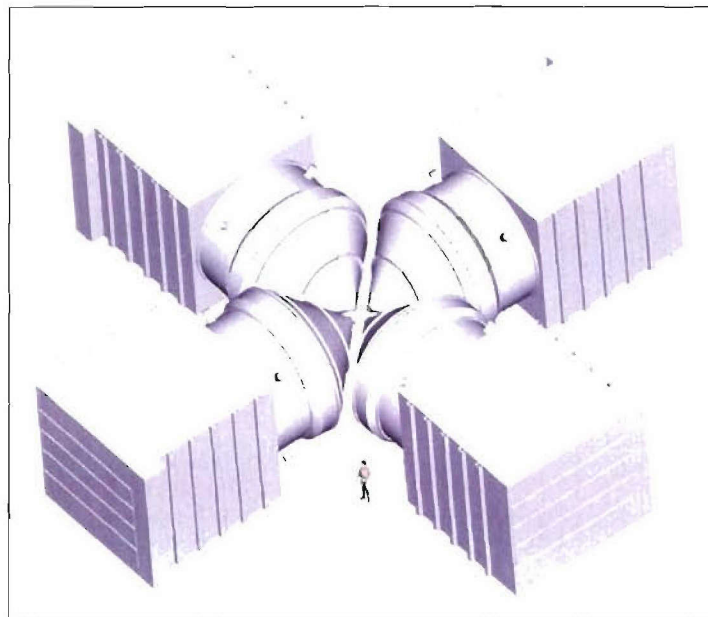
Figure 1. The MPI IR&D concept for a Next Generation Machine consisted of four 25 MA PRS, requiring a total of 120 MJ stored at an estimated cost of $2/J.

Several study kick-off meetings involving our MPI-PSI Team, the AASC Team, NRL, and DTRA produced the following ground rules for the effort:

- Focus on the pulse power technology of the PRS drivers point designs. Candidates for investigation included conventional Marx Generator Drivers (MGD) and Linear Transformer Drivers (LTD), with consideration for improved switch and capacitor components.
- Design the full system to deliver 400 kJ of Kr k-shell in one of two configurations;
  - Four 100 kJ modules (modular).
  - One 400 kJ module (monolithic).
- No plasma vacuum pulse compression in the point designs.
- Perform a system analysis to develop the parameters for each point design.
- Translate the point designs into models for analysis/trade studies.

A schematic diagram of our planned approach is shown in Figure 2. We intended to begin by looking at the state-of-the-art and feasible near-term extensions of pulse power component technology. Based on component performance projections, we would sketch point designs for the simulator sufficient to uncover fundamental design flaws and develop reasonable models for predicting simulator performance and cost. The output predictions from the models could then be used to revise component requirements as necessary to minimize cost while maintaining acceptable performance.
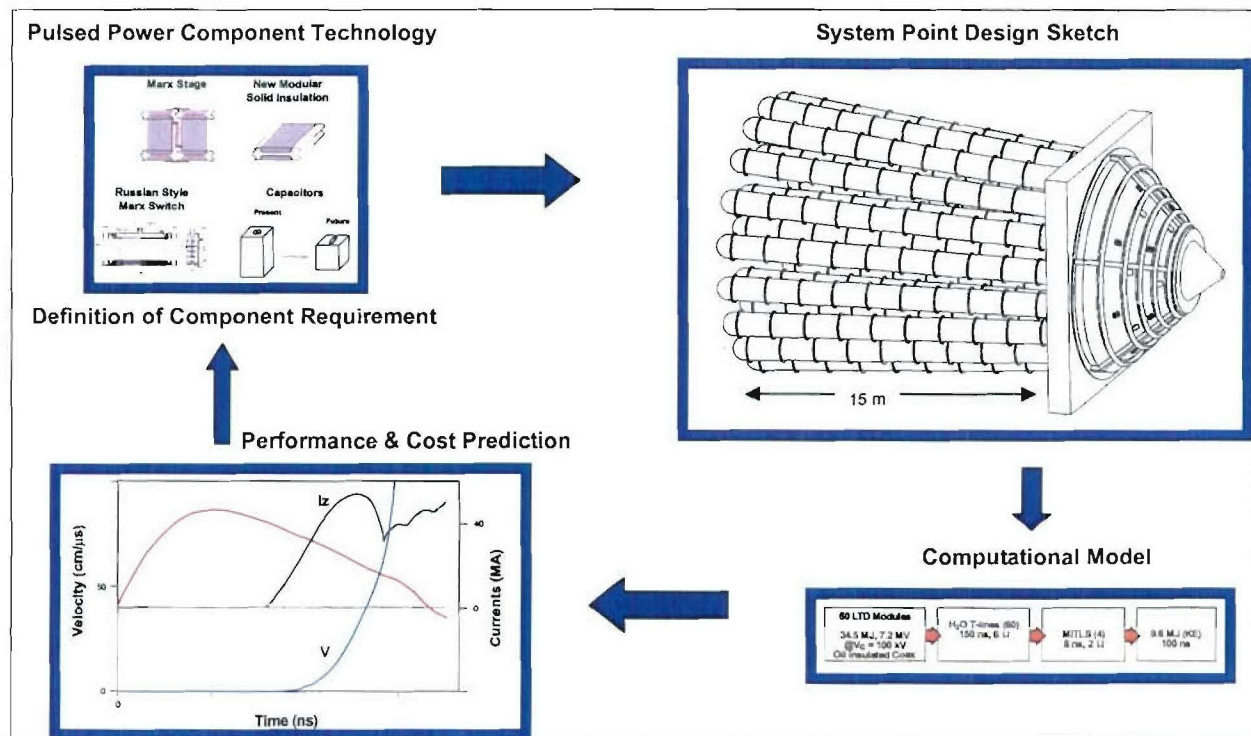
Figure 2. Planned method of pulsed power technology development (Linear Transformer Driver example).

One of our initial tasks was to adopt a better model for the krypton k-shell yield than the simple I^4 scaling used in the MPI concept study. Experiments completed by MPI on ACE 4, Double-Eagle, and Saturn demonstrated that yield scaled inversely with implosion time. This meant that instead of the 20 to 25 MA assumed in the MPI concept study, at least 30 MA would be needed to produce 100 kJ of krypton k-shell radiation. Extensive numerical modeling in 2-D and 3-D at NRL also indicated lower efficiency than the 1/Z assumed in the MPI concept study. For the system study we modified the simple O-D M-Q-K model that already incorporated the experimentally confirmed $1/\tau$ dependence to agree with the lower efficiency derived from NRL's calculations. (See Section 4 of this report for more details of the model.) Applying the model to the problem of obtaining 100 kJ of krypton k-shell x-rays from a 250 ns implosion increased the required current to ~ 37 MA (with an uncertainty approaching 100%).

A second issue addressed during the initial phase of this study was the comparison between modular and monolithic configurations. Figure 3 illustrates the different configurations. In the MPI concept design, we had selected the modular configuration to take advantage of the geometrical gain factor illustrated in Figure 4 to reach the highest dose-area product for a fixed total source strength. However several factors not addressed in the MPI IR&D concept such as peak dose capability, module-to-module variability, and debris-shield compatibility can complicate the choice.
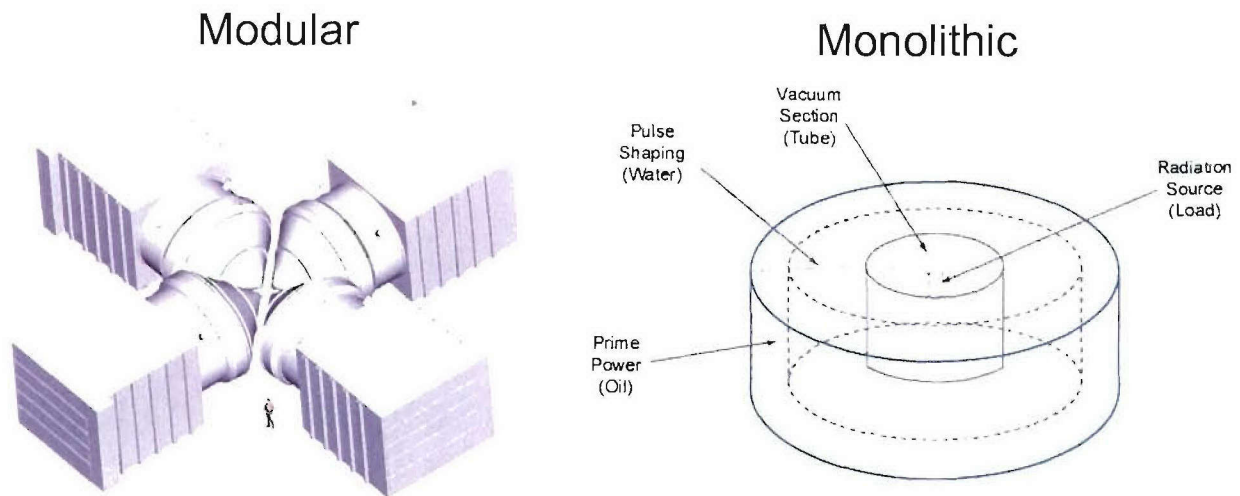
Figure 3. Modular and Monolithic source configurations.

Analyses of these configurations performed independently by the MPI-PSI and AASC Teams agreed on the following conclusions:

- Modular systems can illuminate larger areas for fluences of 1 cal/cm^2 or less. For higher fluences, the monolithic system can have an advantage. The modular system can reach the higher fluences by moving the test object close to one of the sources, but the area for uniform exposure is smaller (by a factor of 4).

- Variability in source output and timing decrease the advantage of the modular system. To maintain its advantage, the reproducibility of the modular sources must be around ±10% or better. (See Figure 4.)
- Debris shields may be easier to construct for the monolithic configuration, but the options for debris shield technology must be defined before an evaluation can be completed.
- While the total stored energy required for the monolithic configuration may be less (~60 MJ versus ~120 MJ for the combined sources), four 30 to 40 MJ modules may be more affordable than a 60 MA monolithic system. The modular approach also has programmatic advantages in risk and cost management.
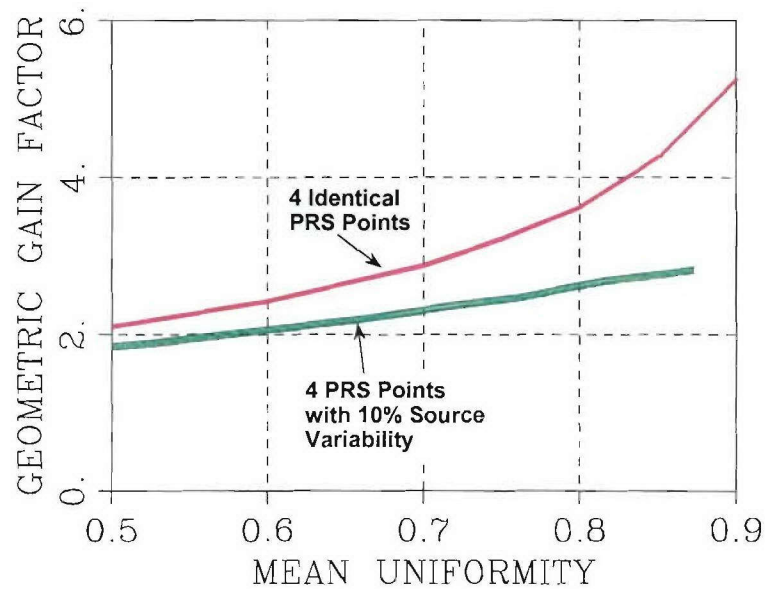
Figure 4. Ratio of the source strength required from one PRS point to the sum of the source strengths from four PRS points to obtain a fluence area product of 10^4 cal.

Our study developed the trade-analysis tools (See Section 4.2) to enable DTRA to make the choice between monolithic and modular configurations. The down select will require a clear definition of the requirements for the simulator. Until the ultimate application is definitized, we elected to develop point designs for both configurations.

In parallel with our efforts to incorporate a more realistic PRS model and address the issue of modular versus monolithic configurations, we attempted to apply the methodology of Figure 2 to a single module of the MPI IR&D concept shown in Figure 1. We began with a reasonable set of component requirements: we assumed a "fast" pulsed power driver with $\sqrt{L \bullet C}$ = 300 ns (state-of-the-art is $\sqrt{L \bullet C}$ = 500 ns) and a front-end vacuum inductance of 22 nH. As in the DECADE Module design, a water transmission line was used to connect the MGD and the front-end vacuum section. The electrical length of the water line was set at ~75 ns by the "Schlitt" condition to take advantage of reflections to increase the load current. A self-consistent vacuum

power flow mechanical sketch was developed that was just able to meet the stress and geometrical constraints. However we were unable to complete a sketch for connecting the pulsed power driver:

- For the MGD, we found no solution in the current range from 25 to 40 MA.
- For the LTD, we found a solution for currents as high as 30 MA, but when the estimate for current required increased to 37 MA, this approach also required more area than was available at the driver transmission line interface.

This initial result motivated us to adopt a more general systems analysis approach.

In our systems analysis approach, instead of starting with component specifications, we begin with generic circuit elements connected as shown in Figure 5:

- Driver (Direct Drive Marx, Marx + water compression stages, or LTD) characterized by

$$\tau \, (= \sqrt{L \bullet C}) \text{ and } Z \, (= \sqrt{L/C}).$$

- No resistive losses; energy is forward-going.
- Transmission Line $Z_{H2O} = Z$ (not a Schlitt Line which implies $\sim$ 20% efficiency penalty).
- Vacuum front end including PRS with revised M-Q-K model
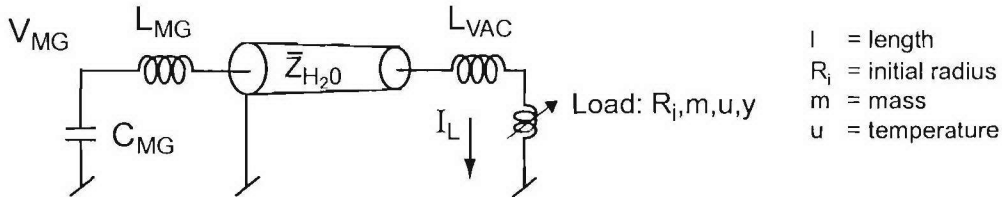
Figure 5. Generic element model used in system analysis.

We used the circuit model to perform a set of calculation according to the following algorithm:

- Specify a yield (100 kJ or 400 kJ of krypton k-shell) and an implosion time (100 or 250 ns).
- Fix temperature (u) = 2/7 (- minimizes KE and stored energy) in the M-Q-K model.
- Vary Driver $Z = \sqrt{L/C}$, Driver $\tau = \sqrt{L \bullet C}$, front-end vacuum inductance L_{vac}, and implosion length ℓ.
- Exercise code to find R_i, m, and V_{MG} (hence Marx energy required).

We scanned over a reasonable parameter space to find the values of ℓ, τ, and, Z that for a given L_{vac} minimized the required stored energy. Our system analysis indicated large pay-offs in two areas (see Figure 6):

- Lowering front-end inductance from 24 to 8 nH reduced the required energy stored by a factor of 2.
- Lowering driver time from 300 to 175 ns nH reduced the required energy stored by a factor of 2.5.
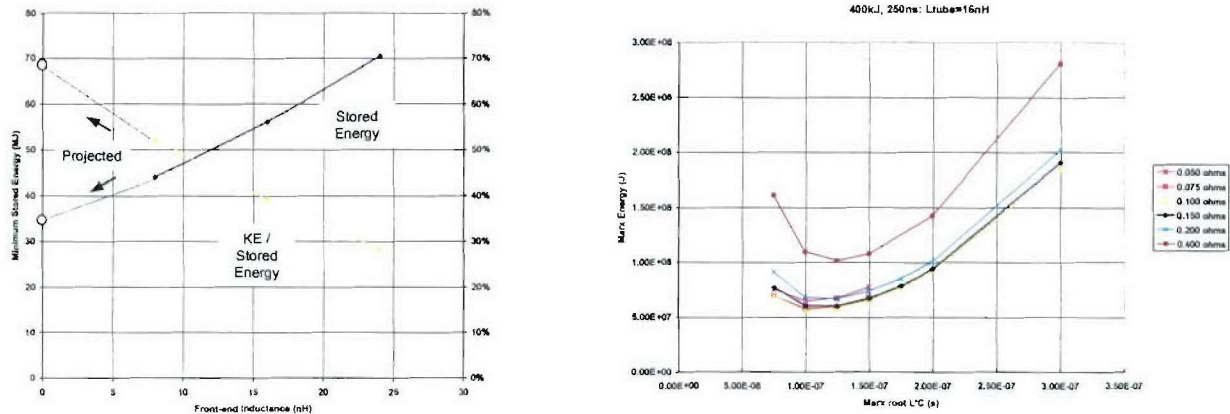
Figure 6. System analysis results indicating large pay-offs for reducing front-end inductance and Driver t for the 400 kJ/250 ns point designs.

In contrast to the original methodology of Figure 2, we then used the optimum values of Driver Z, Driver τ, and front-end vacuum inductance L_{vac} to set goals for component specifications. This led to an evaluation of the state of component technology to see which specifications were feasible or could be achieved with limited developmental efforts.

For L_{vac} we developed estimates for three point designs based on reasonable extensions of work performed on Saturn and Z at SNLA:

- 8 nH for a 400 kJ/250 ns design
- 15 nH for a 100 kJ/250 ns design
- 16 nH for a 400 kJ/100 ns design.

It should be noted that all of these values for L_{vac} are less than the 22 nH used in our initial attempt at a point design.

For Driver τ, we began with the "slow" state-of-the-art (SOA) for capacitors and switches, which sets $\sqrt{L \bullet C} \sim 500$ ns. We then envisioned the process shown in Figure 7 to take component

6

technology from the SOA of 500 ns to 300 and 175 ns. Assuming success in this technology development process, we generated in Table 1 a set of specifications for components that could be used in point designs. Sketches of the components and the resulting MGD are shown in Figure 8.
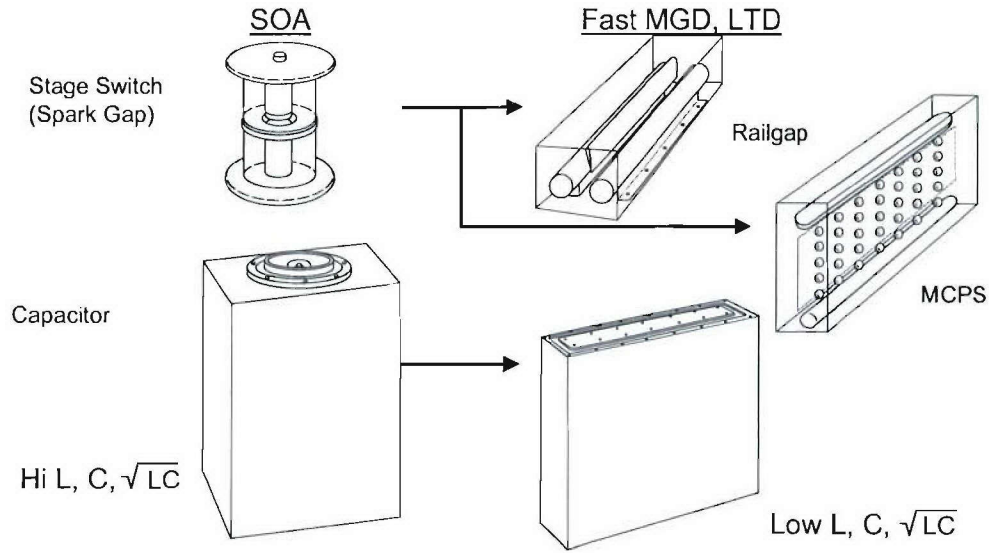
Figure 7. Evolution of component technology required to go from "slow" (~500 ns) state-of-the-art to "fast" (~300 ns) and "ultra-fast" (~175 ns).

Table 1. Component specifications for fast and ultra-fast Marx stages.

$\sqrt{LC}$	175 ns	300 ns
V_{STAGE}	100 kV	180 kV
C_{STAGE}	600 nF	750 nF
L_{CAP}	10 nH	40 nH
L_{GAP}	10 nH	45 nH
I_{STAGE}	160 kA	270 kA
W_{STAGE}	3 kJ	12 kJ
Dimensions		
d	2.5 in.	5 in.
w	24 in.	24 in.
h	20 in.	36 in.
dia	1.5 m	2.3 m
L	5.1 m	4.2 m
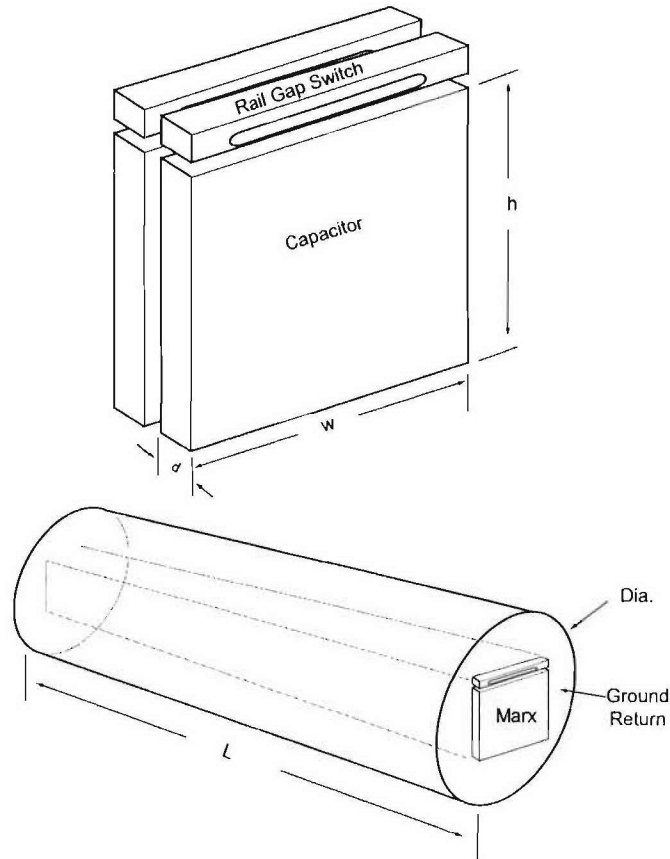
Figure 8. Sketches of Marx stages and arrays constructed from component development efforts recommended by this study.

Based on these component specifications, we developed mechanical "Point Designs" for the following 250 ns cases:

- Slow Marx Generator Driver + Transfer Caps (monolithic only)
- Fast MGD (300 ns) + Peaking Caps
- UltraFast MGD (175 ns) Direct Drive
- UltraFast LTD (125 ns - 175 ns) Direct Drive.

Except for the first bullet, point designs for both the monolithic and modular configurations were developed, but it was noted that the conical geometry of 100 kJ modules is challenging. Table 2 summarizes the progression in the point designs for the monolithic configuration.

Table 2. Progression of point designs for monolithic option.

	LTD	Slow Marx + Transfer Cap	Faster Marx + Peaker	UltraFast Marx
Overall Size	Largest	Next Largest	Medium	Smallest
Energy in Water	N/A	All	<1/2	None
Number of Modules Needed for 400 kJ	64	60	96	256

Based upon the results of this study, we recommend DTRA consider the following areas for future R&D:

- DTRA conduct whatever research is required to define application requirements to resolve modular vs. monolithic configuration issues
- PRS R&D to reduce uncertainty in warm photon yield scaling for 100 ns and 250 ns implosions
- Identification of effective and practical debris reduction/mitigation configurations
- Power flow research to validate the assumptions made in this study and to further minimize vacuum inductance
- Pulse power component and subsystem development to reduce driver time from 500 ns to fast and ultra-fast levels
- Construct a ~ 5 MA prototype LTD/MGD system for demonstration/validation of the technology developments
- Pursue high risk / high pay-off approaches in parallel
  - Increase implosion time to > 250 ns
  - Plasma vacuum power multiplication schemes.

In the absence of the R&D recommended above, DTRA's only option for building a 400 kJ krypton k-shell source for simulation would be the Slow-Marx + Transfer Capacitor configuration. This approach is equivalent to SNLA's current proposal for upgrading Z to the 30 MA level.

The estimated time required for the recommended R&D program to develop the technology required to enable the other, more affordable options is three to five years. An additional benefit is that the new advanced pulsed power technology can also be utilized to upgrade existing DTRA and DoE simulators. Specific beneficiaries of the recommended R&D include:

- Decade Quad and CTEIP Upgrades
  - Pulsed power opening switch and power flow development will provide the technology to achieve high fidelity bremsstrahlung capability on the existing Decade Quad.
  - New fast energy storage technology can be utilized to bring the second quad and the gamma machine in the CTEIP plan on-line with enhanced capabilities at a lower cost.

- San Leandro Facility Upgrades
  - As aging facilities (PITHON, Double-EAGLE) are upgraded, the new, fast energy storage technology could provide improved reliability and output performance at a lower cost.
  - The demonstration test bed could serve as an upgrade of PITHON or Double-EAGLE.
- Sandia Z Upgrade
  - Fast capacitors and switches could be used to support the goals of the Z upgrade program.

The details of the work, conclusions, and recommendations summarized in this overview are contained in the following sections of this report.

SECTION 2
REQUIREMENTS AND CONSTRAINTS

2.1   STATEMENT OF WORK CHARTER.

The Defense Threat Reduction Agency (DTRA) has developed a class of pulsed power radiation simulators for the Services, DoD agencies, and other government agencies, which are used to simulate the x-ray environment caused by nuclear weapons in order to evaluate the survivability and performance of electronic assemblies and optical structures under various threat scenarios. Over the past thirty years, numerous simulators have been designed, acquired, operated, and upgraded to satisfy the evolving user test requirements. Full certification simulator capabilities will require significantly higher power and energy than existing simulators and will become more feasible if effective, affordable technologies can be developed.

Our objective was to complete assessments of power generation, power amplification, and power flow techniques for advanced full certification x-ray radiation source capabilities. Included are concept development and evaluation, conceptual design definitions, and physics design to support advanced power flow development for both plasma radiation sources and bremsstrahlung affordable full certification simulator technology. We have collaborated substantially with other DTRA contractors and relevant DoD and DoE agencies in performing these tasks.

We identified, developed, and evaluated conceptual design options for an affordable full certification simulator. These designs were capable of driving radiation sources for minimum yields of 100 kJ of 15 keV, and 350 kJ of 5 keV radiation.

Our statement of work consisted of three tasks:

Task 1: Design Studies for Affordable Full Certification Capability

We identified a complete set of candidate energy storage and power flow designs to meet the above goals. These included:

- Direct drive with fast Marx generators
- Conventional Marx generators using advanced parallel water capacitors as intermediate stores
- Linear transformer driver (LTD) designs including Russian and French approaches, as well as developing an alternative, more appropriate LTD design
- Conventional water-line pulse forming line systems
- Inductive store/opening switch systems.

Task 2: System Evaluation and Risk Assessment

We employed selection criteria, based on our experience in developing simulators, to down-select to a minimal set of candidate designs. In performing this down-select, each identified design was sufficiently evaluated using a consistent set of engineering criteria. Since one

machine may not drive all the loads, independent candidate drivers were considered. For multi-module approaches, consideration was given to temporal and spectral reproducibility and jitter.

Task 3: Tech Transfer and Reporting

We identified critical R&D needed for each of the selected designs and developed recommendations for risk reduction, and coordinated and participated in Integrated Product Team working meetings that included key representatives from other DTRA contractors and relevant DoD and DoE agencies.

2.2   CONSTRAINTS.

Because the potential parameter space for an advanced simulator (sometimes referred to as a Next Generation Machine (NGM) or a Full Threat Simulator (FTS)) is gigantic, DTRA imposed some ground rules on the study.

During a 9-30-99 Planning Meeting, DTRA provided initial guidance for the required capabilities for one of 4 sources:

- PRS capability: 100 kJ at 15 keV, 350 kJ at 5 keV
- Warm BRS capability: 300 kV endpoint, 30 ns pulsewidth, 0.5 cal/cm^2 over 500 cm^2
- Hot BRS capability: 1.5 MV endpoint, 20 ns pulsewidth, 4 x 10^{12} rad/s (Si) over 2000 cm^2.

During the 10-14-99 teleconference the CTM directed the IPT to focus on PRS requirements only.

On 11-2-99 DTRA circulated the following comments on a summary prepared by MPI of the Radiation, Electrical, and Operational Requirements.

- **Radiation Requirement:** *The radiation requirement is 400 kJ of Krypton K. A four-module approach at 100 kJ per module is acceptable.*

- **Technology Requirement – Consider two cases:**

Case 1. Build now with existing technology.
Case 2. Ready to build on demand after a five year R&D program.

   If the design is modular, then synchronization is important.

- **Operational Requirements:** *Facility should be capable of one shot per 8 hour shift.*

SECTION 3
FULL THREAT SIMULATOR POINT DESIGNS

Our study assumed the objective was to produce 400 kJ of krypton k-shell radiation from a plasma radiation source (PRS). After an initial attempt to create a point design for meeting the objective encountered problems, we recognized the need to perform a system analysis employing simplified models to create a set of specifications for sub-system (primary energy store, water pulse compression/transmission lines, vacuum power flow) design. Using our experience with pulsed power system design, we then created point designs capable of meeting the specifications. In this section, we will first present the System Analysis that was used to generate specifications for the pulsed power sub-systems and then present the point designs that we have selected for more detailed development and analysis.

3.1   SYSTEM ANALYSIS.

3.1.1   Introduction and Overview.

Argon implosions have demonstrated performance in the 100 ns and 250 ns implosion regimes on Double Eagle. Consequently we have taken these two implosion times as the starting point for our system design analysis of driver specifications for a simulator capable of providing 400 kJ of krypton k-shell radiation. We considered two source configurations:

- One single (monolithic) source generating the 400 kJ
- A distributed (modular) four-source-circular array with each individual source generating 100 kJ and the associated driver taking up an angle of $\pi/2$ radians.

In order to estimate the load current required to produce 400 kJ, we have used the simple 0-D Mosher model that will be discussed in Section 4, producing the results shown in Table 3.

Table 3. 0-D estimates of load currents required for 400 kJ krypton systems.

	Implosion Times	
Krypton k-shell Yield	**100 ns**	**250 ns**
Module Load Current for 100 kJ (4 source configuration)	30 MA	37 MA
Load Current for 400 kJ (Monolithic configuration)	42 MA	52 MA

Initial analysis eliminated the 100 kJ/100 ns modular design point. (Our design algorithm diverged, i.e., the high LdI/dt voltage at the insulator stack caused increased insulator dimension, which in turn drove increased vacuum inductance, resulting in even greater LdI/dt voltages, etc.) We adopted a system analysis approach to set requirements for sub-system design for the other three cases:

- 400 kJ/250 ns
- 400 kJ/100 ns
- 100 kJ/250 ns.

13

A generic circuit was developed to be representative of potential driver technologies. A wide range of parameters could be scanned using this model until the underlying trends became obvious. The modeling results for the 400 kJ/250 ns monolithic load will be discussed at some length in Section 3.1.3. The broadest range of system parameters was scanned for this load. Results will also be shown for the 400 kJ/100 ns monolithic load and the 100 kJ/250 ns Modular load in Section 3.1.3. General conclusions and observations will be made on the basis of these results.

3.1.2 Analysis Approach.

Generic Circuit. The generic circuit is shown in Figure 9. It consisted of a driver, a connecting transmission line, a front-end (vacuum region) inductance, and an imploding shell load model. The krypton radiation was calculated using Mosher's model. The elements will be described in the next few sub-sections and the solution method will be described in the last sub-section.
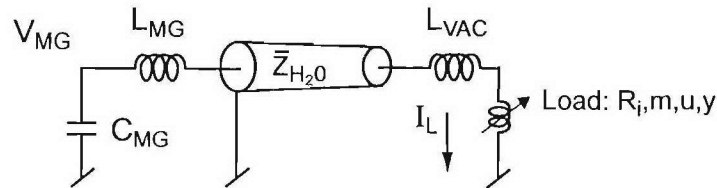
Figure 9. Simplified circuit used for system studies.

Driver. A capacitor and an inductor model the driver to produce a generic sinusoidal pulse shape. Although the driver was often referred to as a "Marx," since it consists of only a C and an L, it really represents any pulse power circuit that produces a similar pulse shape. For the purposes of these scans, the driver was characterized by its impedance ($\sqrt{L/C}$) and its time constant ($\sqrt{L \bullet C}$). The driver pulse length could be varied directly by changing the time constant. Both impedance and time constant were free parameters for these scans. The drive energy is approximated as the initial energy stored in the capacitor. The transmission line down stream impedance was always matched to the driver for greatest efficiency.

While this driver produces a generic pulse shape, it does not accurately represent a real driver since it does not contain any resistive elements to represent switches and charging chains and nor does it have any transit time due its physical length and breadth. Therefore, the driver energy in this generic model should be viewed as that at the output terminal of a real driver. The actual stored energy will be approximately 20% greater depending on the technology.

A real driver also need not be matched in impedance to the transmission line downstream. An impedance step up can lower the charge voltage needed on the driver but will lower the system efficiency depending on the size of the step.

Transmission Line. This element represents the electrical connection between the driver and the front end/load. It was assumed to be a loss-less transmission line element that was characterized by its impedance and its one way transit time. As mentioned above, its impedance was matched to the driver, although the particular value was allowed to vary. It was assumed to be constant impedance for most of the runs in order to reduce the number of free parameters. A few runs were made using a geometrically increasing impedance that resulted in lower overall system efficiencies, however, there may still be benefits of a taper that are as yet undiscovered. Its transit time was made greater than half the implosion time in order to transit time isolate the driver from the front-end inductance. Thus, any longer length could have been used since this transmission line was loss-less. The line length was allowed to vary in some scans.

A real transmission line will of course have resistive losses due to the conductivity of the dielectric and the skin effects of the metal that may ultimately result in an optimal length. And, while the model makes no explicit assumption about the dielectric itself, the low impedance makes water the only practical choice.

Front End Inductance. The front-end inductance was represented by a 4 ns long transmission line rather than a lumped inductance in order to more accurately model the actual efficiency of its coupling to the load during the final few nanoseconds of the implosion when parts of the front end are transit time isolated from the load. A constant impedance line was used to evenly distribute the inductance along its length. This element was used to represent the entire initial inductance from the end of a constant impedance drive line all the way through to the initial position of the imploding liner. It, therefore, was assumed to include the extra inductance in the water flare leading into the insulator stack, the inductance of the insulator stack, its vacuum flare, the MITLs, convolutes, final feeds, and the load region inductance between the anode return posts and the initial position of the liner. The initial load region was included so that it was decoupled from changes to the load itself. The front-end inductance could be held constant while scanning the load's initial radius and length.

A realistic front-end design is subject to a large number of constraints such as insulator flashover and MITL insulation limits. The front-end design for the 400 kJ/250 ns monolithic load will be presented in greater detail in Section 5.

When "tube voltage" is cited, it refers to the voltage just upstream of the front-end inductance. It should not be confused with the insulator/vacuum interface voltage that will generally be about 3/4 of the tube voltage depending on details of the design. Such details are beyond the intended resolution of this model.

Load Model. The load in the generic circuit was assumed to be an imploding shell whose length, initial radius, mass, and compression ratio are specified. The krypton k-shell yield was calculated using Mosher's radiation model. The compression ratio was fixed at 10:1 while the other parameters were free variables. Since we were using the radiation model to calculate the yield, we gave no particular value to load's length or initial radius other than how they changed the load's coupling to the rest of the circuit. For example, large radii were scanned since they were the most efficient radiators even though consideration of Raleigh-Taylor instabilities would undoubtedly limit the radius of a real load one might design today. A scan will be presented for

15

the 400 kJ/250 ns case which shows the effect of changing the load radius alone. Similarly, the length was allowed to vary without regard to possible end effects.

Implosion times of 250 ns were studied without regard to instabilities, similarly, the radius was allowed to vary in order to preserve the optimal temperature according to Mosher's model (u = 2/7). The hope was that this would also provide the most efficient system as well. [A simple scan suggested that this was true, for at least one set of conditions (see 400 kJ/250 ns monolithic results).]

Solution Algorithm. This circuit was modeled using PSI's proprietary circuit code TLCODE. The input/free parameters for each run were:

- Driver Z and T
- Transmission line Z and T (Z transmission line = Z driver)
- Front-end inductance
- Load length
- Implosion time
- Kr K-shell yield
- Load temperature parameter u=2/7.

The driver Z and T are $\sqrt{L/C}$ and $\sqrt{L \bullet C}$ respectively. The implosion time was calculated from the beginning of the pulse to the time of implosion. The beginning time was determined by linear extrapolation from the 20% and 50% points on the load current waveform. The other parameters were described in prior sub-sections.

From these inputs, the values of driver charge voltage (stored energy), load radius, and load mass were found by iteration using a special algorithm developed for this purpose. This algorithm was embedded into the circuit code so that solutions could be found quite rapidly and accurately. A number of solutions were checked in separate calculations and two cases were checked using the MICROCAP circuit code with Mosher's model as a benchmark.

3.1.3 System Scan Results.

The following system optimization scans were made with the generic circuit shown in Figure 9. Wide ranges of parameters were scanned using this model until the underlying trends became obvious. The modeling results for the 400 kJ/250 ns monolithic load will be discussed at some length in the next paragraph where the broadest range of system parameters were scanned and the most discussion of the results is given. Results will also be shown for the 400 kJ/100 ns monolithic load and the 100 kJ/250 ns modular load in the following paragraphs.

400 kJ/250 ns Monolithic Case. Table 4 summarizes modeling results for the 400 kJ/250 ns monolithic load. A number of input parameters were held fixed for all of these runs. For all these runs the water transmission line length was fixed at 150 ns, the length of the front-end inductance was fixed at 4 ns, the load length was 4 cm and the Mosher load temperature parameter "u" was fixed at 2/7. The krypton k-shell yield and implosion time were, of course, also fixed at 400 kJ and 250 ns, respectively.

16

The table has been separated into three parts each with 14 columns of numbers on it. Each line (row) on that table represents a single circuit simulation. Some of the numbers on each row show input parameters while others show the calculated results. A total of 94 simulations are represented in this table.

First, definitions of the column headings going from left to right: The first six columns are driver parameters. The driver is also referred to as a "Marx" since it is modeled by a C and an L, however it is intended to represent a generic drive circuit which produces a sinusoidal pulse shape. The last four are load parameters.

- "Root L/C" [ohms] is the driver's dynamic impedance and was an input parameter.
- "Root L*C" [seconds] is the driver's time constant and was also an input parameter. The drive pulse width is pi times this time constant, base to base.
- "Lmarx" [henrys] and "Cmarx" are the values of the drive L and C circuit parameters and were derived directly from the input impedance and time constant. They were listed on the table as a convenience although they add little to the data analysis.

Table 4(a). Scan of Driver Time Constant and Impedance for vacuum inductance of 8 nH for the 400 kJ/250 ns case.

Root L/C	Root L*C	Lmarx	Cmarx	Vmarx	Emarx	Zwater	Vtube	Ttube	Lvac	Ipkload	Rinit	Mtotal	KE
5.00E-02	5.00E-08	2.50E-09	1.00E-06	1.33E+07	8.83E+07	5.00E-02	1.17E+07	1.97E-07	8.00E-09	1.11E+08	1.90E-01	2.68E-05	2.81E+07
5.00E-02	7.50E-08	3.75E-09	1.50E-06	8.22E+06	5.06E+07	5.00E-02	6.60E+06	2.18E-07	8.00E-09	8.15E+07	1.47E-01	2.36E-05	2.49E+07
5.00E-02	1.00E-07	5.00E-09	2.00E-06	6.64E+06	4.41E+07	5.00E-02	4.94E+06	2.37E-07	8.00E-09	7.00E+07	1.27E-01	2.19E-05	2.33E+07
5.00E-02	1.25E-07	6.25E-09	2.50E-06	6.13E+06	4.69E+07	5.00E-02	4.25E+06	2.53E-07	8.00E-09	6.51E+07	1.17E-01	2.11E-05	2.24E+07
5.00E-02	1.50E-07	7.50E-09	3.00E-06	6.01E+06	5.41E+07	5.00E-02	3.92E+06	2.69E-07	8.00E-09	6.24E+07	1.11E-01	2.05E-05	2.19E+07
5.00E-02	1.75E-07	8.75E-09	3.50E-06	6.07E+06	6.45E+07	5.00E-02	4.44E+06	4.31E-07	8.00E-09	6.10E+07	1.08E-01	2.02E-05	2.16E+07
5.00E-02	2.00E-07	1.00E-08	4.00E-06	6.24E+06	7.80E+07	5.00E-02	4.95E+06	4.32E-07	8.00E-09	5.99E+07	1.05E-01	1.99E-05	2.13E+07
5.00E-02	3.00E-07	1.50E-08	6.00E-06	7.39E+06	1.64E+08	5.00E-02	5.99E+06	4.35E-07	8.00E-09	5.81E+07	9.99E-02	1.94E-05	2.08E+07
7.50E-02	7.50E-08	5.63E-09	1.00E-06	1.03E+07	5.33E+07	7.50E-02	7.39E+06	2.13E-07	8.00E-09	8.60E+07	1.55E-01	2.42E-05	2.56E+07
7.50E-02	1.00E-07	7.50E-09	1.33E-06	8.20E+06	4.48E+07	7.50E-02	5.31E+06	2.26E-07	8.00E-09	7.20E+07	1.32E-01	2.24E-05	2.37E+07
7.50E-02	1.25E-07	9.38E-09	1.67E-06	7.48E+06	4.67E+07	7.50E-02	4.44E+06	2.37E-07	8.00E-09	6.59E+07	1.20E-01	2.13E-05	2.27E+07
7.50E-02	1.50E-07	1.13E-08	2.00E-06	7.30E+06	5.33E+07	7.50E-02	4.15E+06	4.25E-07	8.00E-09	6.28E+07	1.14E-01	2.07E-05	2.21E+07
7.50E-02	1.75E-07	1.31E-08	2.33E-06	7.37E+06	6.33E+07	7.50E-02	4.93E+06	4.27E-07	8.00E-09	6.10E+07	1.09E-01	2.03E-05	2.17E+07
7.50E-02	2.00E-07	1.50E-08	2.67E-06	7.57E+06	7.64E+07	7.50E-02	5.48E+06	4.28E-07	8.00E-09	5.98E+07	1.06E-01	2.00E-05	2.14E+07
7.50E-02	3.00E-07	2.25E-08	4.00E-06	8.90E+06	1.58E+08	7.50E-02	6.63E+06	4.31E-07	8.00E-09	5.77E+07	1.00E-01	1.95E-05	2.09E+07
1.00E-01	7.50E-08	7.50E-09	7.50E-07	1.26E+07	5.93E+07	1.00E-01	8.15E+06	2.05E-07	8.00E-09	9.01E+07	1.63E-01	2.48E-05	2.61E+07
1.00E-01	1.00E-07	1.00E-08	1.00E-06	9.83E+06	4.83E+07	1.00E-01	5.66E+06	2.21E-07	8.00E-09	7.35E+07	1.36E-01	2.27E-05	2.40E+07
1.00E-01	1.25E-07	1.25E-08	1.25E-06	8.89E+06	4.94E+07	1.00E-01	4.63E+06	2.29E-07	8.00E-09	6.65E+07	1.23E-01	2.16E-05	2.29E+07
1.00E-01	1.50E-07	1.50E-08	1.50E-06	8.62E+06	5.58E+07	1.00E-01	4.57E+06	4.22E-07	8.00E-09	6.28E+07	1.15E-01	2.08E-05	2.22E+07
1.00E-01	1.75E-07	1.75E-08	1.75E-06	8.69E+06	6.61E+07	1.00E-01	5.41E+06	4.24E-07	8.00E-09	6.09E+07	1.10E-01	2.04E-05	2.18E+07
1.00E-01	2.00E-07	2.00E-08	2.00E-06	8.89E+06	7.90E+07	1.00E-01	5.99E+06	4.26E-07	8.00E-09	5.96E+07	1.07E-01	2.01E-05	2.15E+07
1.00E-01	3.00E-07	3.00E-08	3.00E-06	1.04E+07	1.62E+08	1.00E-01	7.24E+06	4.29E-07	8.00E-09	5.74E+07	1.01E-01	1.96E-05	2.09E+07
2.00E-01	7.50E-08	1.50E-08	3.75E-07	2.23E+07	9.37E+07	2.00E-01	1.06E+07	1.94E-07	8.00E-09	1.01E+08	1.80E-01	2.61E-05	2.74E+07
2.00E-01	1.00E-07	2.00E-08	5.00E-07	1.67E+07	6.96E+07	2.00E-01	6.73E+06	2.01E-07	8.00E-09	7.68E+07	1.45E-01	2.34E-05	2.47E+07
2.00E-01	1.25E-07	2.50E-08	6.25E-07	1.47E+07	6.76E+07	2.00E-01	5.20E+06	2.05E-07	8.00E-09	6.71E+07	1.28E-01	2.20E-05	2.33E+07
2.00E-01	1.50E-07	3.00E-08	7.50E-07	1.41E+07	7.41E+07	2.00E-01	6.09E+06	4.17E-07	8.00E-09	6.25E+07	1.19E-01	2.12E-05	2.25E+07
2.00E-01	1.75E-07	3.50E-08	8.75E-07	1.40E+07	8.60E+07	2.00E-01	7.21E+06	4.17E-07	8.00E-09	6.00E+07	1.12E-01	2.06E-05	2.20E+07
2.00E-01	2.00E-07	4.00E-08	1.00E-06	1.43E+07	1.02E+08	2.00E-01	7.99E+06	4.18E-07	8.00E-09	5.84E+07	1.08E-01	2.02E-05	2.16E+07
2.00E-01	3.00E-07	6.00E-08	1.50E-06	1.66E+07	2.06E+08	2.00E-01	9.52E+06	4.21E-07	8.00E-09	5.59E+07	1.01E-01	1.95E-05	2.09E+07

Table 4(b). Scan of Driver Time Constant and Impedance for vacuum inductance of 16 nH for the 400 kJ/250 ns case.

Root L/C	Root L*C	Lmarx	Cmarx	Vmarx	Emarx	Zmean	Vtube	Ttube	Lvac	Ipkload	Rinit	Mtotal	KE
5.00E-02	7.50E-08	3.75E-09	1.50E-06	1.00E+07	7.54E+07	5.00E-02	9.23E+06	2.27E-07	1.60E-08	6.65E+07	1.23E-01	2.15E-05	2.29E+07
5.00E-02	1.00E-07	5.00E-09	2.00E-06	8.05E+06	6.47E+07	5.00E-02	7.07E+06	2.47E-07	1.60E-08	5.92E+07	1.07E-01	2.01E-05	2.15E+07
5.00E-02	1.25E-07	6.25E-09	2.50E-06	7.35E+06	6.75E+07	5.00E-02	6.18E+06	2.69E-07	1.60E-08	5.60E+07	9.85E-02	1.93E-05	2.07E+07
5.00E-02	1.50E-07	7.50E-09	3.00E-06	7.19E+06	7.75E+07	5.00E-02	5.80E+06	2.86E-07	1.60E-08	5.47E+07	9.44E-02	1.89E-05	2.03E+07
7.50E-02	7.50E-08	5.63E-09	1.00E-06	1.17E+07	6.90E+07	7.50E-02	1.01E+07	2.21E-07	1.60E-08	6.94E+07	1.29E-01	2.20E-05	2.34E+07
7.50E-02	1.00E-07	7.50E-09	1.33E-06	9.30E+06	5.77E+07	7.50E-02	7.47E+06	2.40E-07	1.60E-08	6.04E+07	1.10E-01	2.04E-05	2.18E+07
7.50E-02	1.25E-07	9.38E-09	1.67E-06	8.47E+06	5.97E+07	7.50E-02	6.41E+06	2.59E-07	1.60E-08	5.68E+07	1.01E-01	1.95E-05	2.10E+07
7.50E-02	1.50E-07	1.13E-08	2.00E-06	8.24E+06	6.79E+07	7.50E-02	5.92E+06	2.76E-07	1.60E-08	5.50E+07	9.59E-02	1.90E-05	2.04E+07
1.00E-01	7.50E-08	7.50E-09	7.50E-07	1.36E+07	6.93E+07	1.00E-01	1.09E+07	2.18E-07	1.60E-08	7.21E+07	1.34E-01	2.25E-05	2.38E+07
1.00E-01	1.00E-07	1.00E-08	1.00E-06	1.06E+07	5.63E+07	1.00E-01	7.87E+06	2.36E-07	1.60E-08	6.15E+07	1.13E-01	2.06E-05	2.20E+07
1.00E-01	1.25E-07	1.25E-08	1.25E-06	9.62E+06	5.79E+07	1.00E-01	6.65E+06	2.51E-07	1.60E-08	5.74E+07	1.03E-01	1.98E-05	2.11E+07
1.00E-01	1.50E-07	1.50E-08	1.50E-06	9.34E+06	6.55E+07	1.00E-01	6.06E+06	2.63E-07	1.60E-08	5.54E+07	9.77E-02	1.92E-05	2.06E+07
1.00E-01	1.75E-07	1.75E-08	1.75E-06	9.39E+06	7.71E+07	1.00E-01	5.74E+06	2.78E-07	1.60E-08	5.44E+07	9.45E-02	1.89E-05	2.03E+07
1.00E-01	2.00E-07	2.00E-08	2.00E-06	9.60E+06	9.21E+07	1.00E-01	6.36E+06	4.34E-07	1.60E-08	5.36E+07	9.19E-02	1.86E-05	2.00E+07
1.00E-01	3.00E-07	3.00E-08	3.00E-06	1.11E+07	1.86E+08	1.00E-01	7.84E+06	4.38E-07	1.60E-08	5.20E+07	8.63E-02	1.81E-05	1.95E+07
1.50E-01	7.50E-08	1.13E-08	5.00E-07	1.75E+07	7.68E+07	1.50E-01	1.25E+07	2.13E-07	1.60E-08	7.72E+07	1.42E-01	2.32E-05	2.45E+07
1.50E-01	1.00E-07	1.50E-08	6.67E-07	1.35E+07	6.04E+07	1.50E-01	8.70E+06	2.25E-07	1.60E-08	6.39E+07	1.19E-01	2.12E-05	2.26E+07
1.50E-01	1.25E-07	1.88E-08	8.33E-07	1.20E+07	6.02E+07	1.50E-01	7.11E+06	2.37E-07	1.60E-08	5.84E+07	1.07E-01	2.01E-05	2.15E+07
1.50E-01	1.50E-07	2.25E-08	1.00E-06	1.16E+07	6.73E+07	1.50E-01	6.34E+06	2.49E-07	1.60E-08	5.58E+07	1.00E-01	1.94E-05	2.08E+07
1.50E-01	1.75E-07	2.63E-08	1.17E-06	1.16E+07	7.89E+07	1.50E-01	6.07E+06	4.28E-07	1.60E-08	5.46E+07	9.63E-02	1.91E-05	2.05E+07
1.50E-01	2.00E-07	3.00E-08	1.33E-06	1.19E+07	9.38E+07	1.50E-01	6.87E+06	4.29E-07	1.60E-08	5.37E+07	9.34E-02	1.88E-05	2.02E+07
1.50E-01	3.00E-07	4.50E-08	2.00E-06	1.38E+07	1.90E+08	1.50E-01	8.54E+06	4.33E-07	1.60E-08	5.22E+07	8.78E-02	1.82E-05	1.96E+07
2.00E-01	7.50E-08	1.50E-08	3.75E-07	2.20E+07	9.10E+07	2.00E-01	1.43E+07	2.05E-07	1.60E-08	8.27E+07	1.52E-01	2.40E-05	2.53E+07
2.00E-01	1.00E-07	2.00E-08	5.00E-07	1.65E+07	6.78E+07	2.00E-01	9.46E+06	2.20E-07	1.60E-08	6.58E+07	1.24E-01	2.16E-05	2.30E+07
2.00E-01	1.25E-07	2.50E-08	6.25E-07	1.46E+07	6.67E+07	2.00E-01	7.59E+06	2.29E-07	1.60E-08	5.94E+07	1.10E-01	2.04E-05	2.18E+07
2.00E-01	1.50E-07	3.00E-08	7.50E-07	1.40E+07	7.36E+07	2.00E-01	6.64E+06	2.37E-07	1.60E-08	5.65E+07	1.03E-01	1.97E-05	2.11E+07
2.00E-01	1.75E-07	3.50E-08	8.75E-07	1.39E+07	8.51E+07	2.00E-01	6.54E+06	4.25E-07	1.60E-08	5.47E+07	9.81E-02	1.92E-05	2.06E+07
2.00E-01	2.00E-07	4.00E-08	1.00E-06	1.42E+07	1.00E+08	2.00E-01	7.40E+06	4.27E-07	1.60E-08	5.36E+07	9.49E-02	1.89E-05	2.03E+07
2.00E-01	3.00E-07	6.00E-08	1.50E-06	1.64E+07	2.01E+08	2.00E-01	9.21E+06	4.31E-07	1.60E-08	5.19E+07	8.87E-02	1.83E-05	1.97E+07
4.00E-01	7.50E-08	3.00E-08	1.88E-07	4.15E+07	1.61E+08	4.00E-01	1.96E+07	1.93E-07	1.60E-08	9.65E+07	1.74E-01	2.56E-05	2.70E+07
4.00E-01	1.00E-07	4.00E-08	2.50E-07	2.96E+07	1.09E+08	4.00E-01	1.19E+07	2.00E-07	1.60E-08	7.10E+07	1.36E-01	2.26E-05	2.40E+07
4.00E-01	1.25E-07	5.00E-08	3.13E-07	2.55E+07	1.01E+08	4.00E-01	9.00E+06	2.05E-07	1.60E-08	6.15E+07	1.19E-01	2.12E-05	2.25E+07
4.00E-01	1.50E-07	6.00E-08	3.75E-07	2.40E+07	1.08E+08	4.00E-01	7.54E+06	2.13E-07	1.60E-08	5.70E+07	1.08E-01	2.02E-05	2.16E+07
4.00E-01	2.00E-07	8.00E-08	5.00E-07	2.39E+07	1.43E+08	4.00E-01	9.69E+06	4.19E-07	1.60E-08	5.35E+07	9.82E-02	1.92E-05	2.06E+07
4.00E-01	3.00E-07	1.20E-07	7.50E-07	2.74E+07	2.81E+08	4.00E-01	1.19E+07	4.21E-07	1.60E-08	5.15E+07	9.00E-02	1.84E-05	1.98E+07

- "Vmarx" [volts] is the initial charge voltage on the drive C. It was determined by iteration using the solution algorithm and was adjusted as needed in order to produce the desired 400 kJ yield from the radiation model.
- "Emarx" [joules] is the initially stored energy in the drive C. Emarx was used to gauge the system efficiency.
- "Zwater" [ohms] is the impedance of the constant impedance transmission line. Zwater was always matched to the Root L/C of the driver.
- "Vtube" [volts] is the peak voltage measured just upstream of the front-end inductance.
- "Ttube" [seconds] is the time at which the peak-tube voltage occurred. T=0 was at the beginning of the simulation with the driver fully charged, when looking at Ttube it is important to remember that there is a 150 ns transmission line between the driver and the front end inductance. Ttube was used to determine if the peak voltage occurred during the current rise or as the result of the implosion dL/dt.
- "Lvac" [henrys] is the total front-end inductance at the beginning of the simulation and was an input parameter.
- "Ipkload" [amperes] is the peak load current prior to the implosion.

Table 4(c).   Scan of Driver Time Constant and Impedance for vacuum inductance of 24 nH for the 400 kJ/250 ns case.

Root L/C	Root L*C	Lmarx	Cmarx	Vmarx	Emarx	Zmean	Vtube	Ttube	Lvac	Ipkload	Rinit	Mtotal	KE
7.50E-02	7.50E-08	5.63E-09	1.00E-06	1.36E+07	9.22E+07	7.50E-02	1.25E+07	2.27E-07	2.40E-08	6.22E+07	1.16E-01	2.09E-05	2.23E+07
7.50E-02	1.00E-07	7.50E-09	1.33E-06	1.07E+07	7.69E+07	7.50E-02	9.43E+06	2.47E-07	2.40E-08	5.53E+07	9.95E-02	1.94E-05	2.08E+07
7.50E-02	1.25E-07	9.38E-09	1.67E-06	9.79E+06	7.98E+07	7.50E-02	8.22E+06	2.69E-07	2.40E-08	5.28E+07	9.18E-02	1.86E-05	2.00E+07
7.50E-02	1.50E-07	1.13E-08	2.00E-06	9.49E+06	9.01E+07	7.50E-02	7.64E+06	2.86E-07	2.40E-08	5.15E+07	8.74E-02	1.82E-05	1.96E+07
7.50E-02	2.00E-07	1.50E-08	2.67E-06	9.76E+06	1.27E+08	7.50E-02	7.33E+06	4.40E-07	2.40E-08	5.05E+07	8.27E-02	1.77E-05	1.91E+07
1.00E-01	7.50E-08	7.50E-09	7.50E-07	1.52E+07	8.66E+07	1.00E-01	1.33E+07	2.22E-07	2.40E-08	6.40E+07	1.20E-01	2.12E-05	2.26E+07
1.00E-01	1.00E-07	1.00E-08	1.00E-06	1.20E+07	7.16E+07	1.00E-01	9.89E+06	2.44E-07	2.40E-08	5.65E+07	1.03E-01	1.97E-05	2.11E+07
1.00E-01	1.25E-07	1.25E-08	1.25E-06	1.07E+07	7.30E+07	1.00E-01	8.46E+06	2.61E-07	2.40E-08	5.33E+07	9.40E-02	1.88E-05	2.02E+07
1.00E-01	1.50E-07	1.50E-08	1.50E-06	1.05E+07	8.24E+07	1.00E-01	7.80E+06	2.77E-07	2.40E-08	5.20E+07	8.94E-02	1.84E-05	1.98E+07
1.00E-01	2.00E-07	2.00E-08	2.00E-06	1.08E+07	1.16E+08	1.00E-01	7.38E+06	4.38E-07	2.40E-08	5.06E+07	8.37E-02	1.78E-05	1.92E+07
1.50E-01	1.00E-07	1.50E-08	6.67E-07	1.45E+07	6.98E+07	1.50E-01	1.07E+07	2.35E-07	2.40E-08	5.81E+07	1.07E-01	2.01E-05	2.15E+07
1.50E-01	1.25E-07	1.88E-08	8.33E-07	1.30E+07	7.04E+07	1.50E-01	8.98E+06	2.50E-07	2.40E-08	5.43E+07	9.71E-02	1.92E-05	2.05E+07
1.50E-01	1.50E-07	2.25E-08	1.00E-06	1.25E+07	7.86E+07	1.50E-01	8.12E+06	2.62E-07	2.40E-08	5.26E+07	9.19E-02	1.86E-05	2.00E+07
1.50E-01	2.00E-07	3.00E-08	1.33E-06	1.28E+07	1.09E+08	1.50E-01	7.55E+06	4.34E-07	2.40E-08	5.09E+07	8.55E-02	1.80E-05	1.94E+07
1.50E-01	3.00E-07	4.50E-08	2.00E-06	1.48E+07	2.20E+08	1.50E-01	9.45E+06	4.40E-07	2.40E-08	5.01E+07	8.13E-02	1.75E-05	1.89E+07
2.25E-01	1.00E-07	2.25E-08	4.44E-07	1.85E+07	7.61E+07	2.25E-01	1.20E+07	2.25E-07	2.40E-08	6.04E+07	1.13E-01	2.07E-05	2.20E+07
2.25E-01	1.25E-07	2.81E-08	5.56E-07	1.64E+07	7.44E+07	2.25E-01	9.68E+06	2.37E-07	2.40E-08	5.51E+07	1.01E-01	1.95E-05	2.09E+07
2.25E-01	1.50E-07	3.38E-08	6.67E-07	1.57E+07	8.24E+07	2.25E-01	8.58E+06	2.47E-07	2.40E-08	5.29E+07	9.43E-02	1.89E-05	2.03E+07
2.25E-01	2.00E-07	4.50E-08	8.89E-07	1.59E+07	1.13E+08	2.25E-01	7.92E+06	4.30E-07	2.40E-08	5.10E+07	8.75E-02	1.82E-05	1.96E+07
2.25E-01	3.00E-07	6.75E-08	1.33E-06	1.85E+07	2.28E+08	2.25E-01	1.01E+07	4.34E-07	2.40E-08	5.01E+07	8.26E-02	1.77E-05	1.91E+07
3.00E-01	1.00E-07	3.00E-08	3.33E-07	2.29E+07	8.74E+07	3.00E-01	1.32E+07	2.19E-07	2.40E-08	6.26E+07	1.18E-01	2.11E-05	2.25E+07
3.00E-01	1.25E-07	3.75E-08	4.17E-07	2.01E+07	8.44E+07	3.00E-01	1.04E+07	2.29E-07	2.40E-08	5.65E+07	1.05E-01	1.99E-05	2.13E+07
3.00E-01	1.50E-07	4.50E-08	5.00E-07	1.91E+07	9.15E+07	3.00E-01	9.06E+06	2.37E-07	2.40E-08	5.36E+07	9.74E-02	1.92E-05	2.06E+07
3.00E-01	2.00E-07	6.00E-08	6.67E-07	1.93E+07	1.24E+08	3.00E-01	8.36E+06	4.28E-07	2.40E-08	5.13E+07	8.98E-02	1.84E-05	1.98E+07
3.00E-01	3.00E-07	9.00E-08	1.00E-06	2.22E+07	2.47E+08	3.00E-01	1.08E+07	4.31E-07	2.40E-08	5.00E+07	8.36E-02	1.78E-05	1.92E+07
6.00E-01	1.00E-07	6.00E-08	1.67E-07	4.24E+07	1.50E+08	6.00E-01	1.71E+07	2.00E-07	2.40E-08	6.89E+07	1.33E-01	2.24E-05	2.38E+07
6.00E-01	1.25E-07	7.50E-08	2.08E-07	3.59E+07	1.34E+08	6.00E-01	1.27E+07	2.05E-07	2.40E-08	5.89E+07	1.14E-01	2.07E-05	2.21E+07
6.00E-01	1.50E-07	9.00E-08	2.50E-07	3.36E+07	1.41E+08	6.00E-01	1.06E+07	2.13E-07	2.40E-08	5.47E+07	1.04E-01	1.98E-05	2.12E+07
6.00E-01	2.00E-07	1.20E-07	3.33E-07	3.33E+07	1.85E+08	6.00E-01	1.07E+07	4.19E-07	2.40E-08	5.17E+07	9.40E-02	1.88E-05	2.02E+07
6.00E-01	3.00E-07	1.80E-07	5.00E-07	3.79E+07	3.58E+08	6.00E-01	1.36E+07	4.21E-07	2.40E-08	4.99E+07	8.60E-02	1.80E-05	1.94E+07

- "Rinit" is the initial load shell radius. It was determined iteratively using the solution algorithm and was adjusted to produce optimal load temperature (u=2/7) according to the radiation model.
- "Mtotal" [kilograms] is the total load mass, not mass per unit length. It was also determined iteratively using the solution algorithm and was adjusted to produce the specified implosion time.
- "KE" [joules] is the total kinetic energy delivered to the load at the time of implosion.
- All units in the table are mks unless otherwise noted.

Table 4 has been separated into three parts, one part for each of the three front-end inductances (8 nH, 16 nH and 24 nH under the column labeled L_{vac}) that were modeled. The data has been further subdivided into blocks of the same driver/water line impedance. Finally, within each block, the drive time constant is varied from shortest to longest going down the page.

System Efficiency vs. Drive Pulse Length, Drive Impedance, and Front End Inductance.
Looking at the first block on Table 4(a) (Lvac=8 nH, Zwater=0.05 ohms, and Root L*C ranging from 50 ns to 300 ns), the stored energy in the driver is seen to have a minimum of about 44 MJ somewhere between 100 ns and 125 ns $\sqrt{L \bullet C}$. The minimum Emarx on the table has been highlighted in gray for each block of data. The second block with Zwater=0.075 ohms has a minimum energy of about 45MJ and so on. Emarx has been plotted against $\sqrt{L \bullet C}$ for the 8 nH

19

front end in Figure 10. The 16 nH and 24 nH cases are plotted in Figures 11 and 12. The curves show how the required stored energy changes with drive pulse length ($\sqrt{L \cdot C}$) and how it changes with drive transmission line impedance. The most obvious trend is that there is an optimal $\sqrt{L \cdot C}$ for each drive line impedance and that the optimum is between 100 ns and 125 ns for the range of impedances. Also, there is a huge penalty for driving this load with too long a pulse (imploding during the rise of the current into the load) as in the 300 ns case. The minimum stored energy is also sensitive to the drive line impedance and there is an optimal drive line impedance for each front-end inductance. For example, in the 16 nH case, the optimal drive impedance was 0.1 Ω. The other curves for both higher and lower impedances are all above this one. The stored energy versus drive impedance has been plotted in Figure 13. The optimum drive impedance was about 0.06 Ω for the 8 nH front end, and 0.15 Ω for the 24 nH. Although the scan for the 8 nH front end didn't go low enough in impedance to see the stored energy go up again, it looks like a minimum was reached since the 0.05 Ω and 0.075 Ω curves are nearly identical. Increasing vacuum inductance also increases the required stored energy as shown in Figure 14.
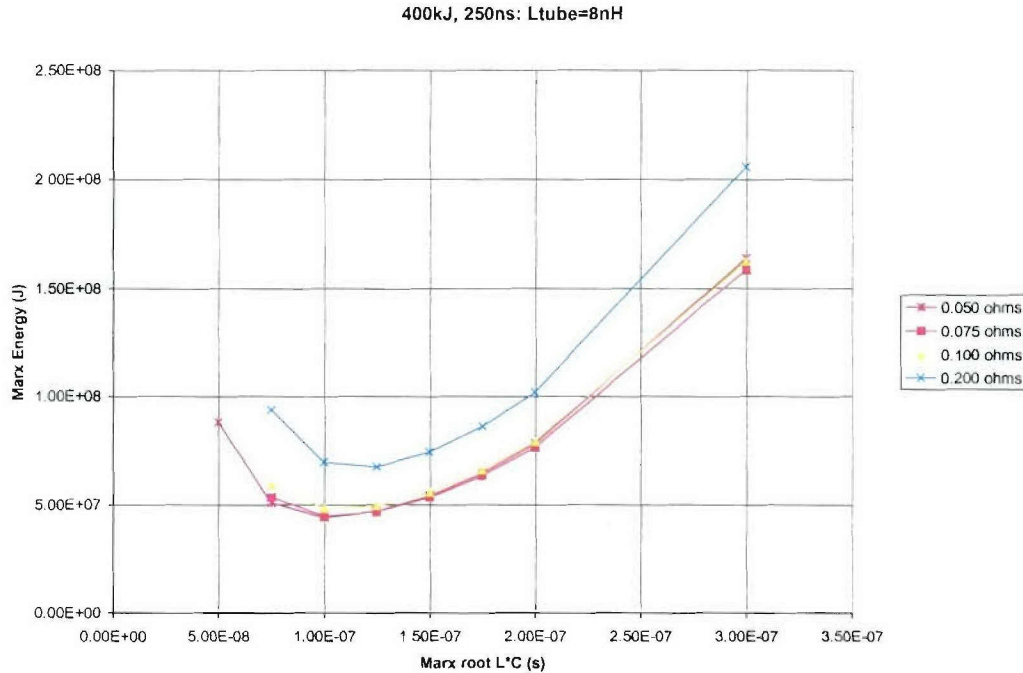
Figure 10. Marx energy required for a 250 ns imploding PRS load 400 kJ krypton k-shell output in a direct drive configuration as a function of $\sqrt{LC}$ and parameterized by $\sqrt{L/C}$ for 8 nH vacuum inductance.

20

400kJ, 250ns: Ltube=16nH
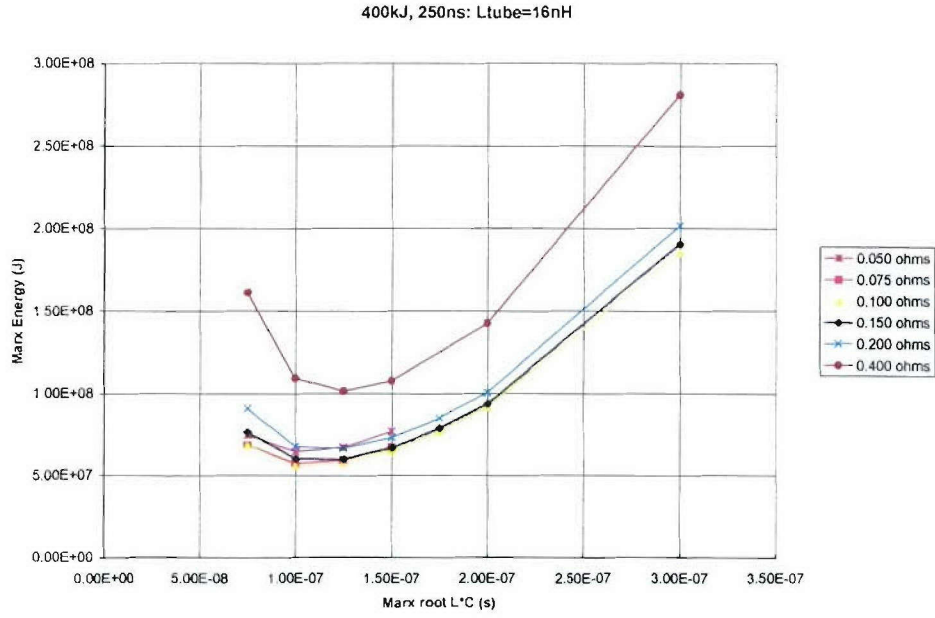
Figure 11. Marx energy required for a 250 ns imploding PRS load 400 kJ krypton k-shell output in a direct drive configuration as a function of $\sqrt{LC}$ and parameterized by $\sqrt{L/C}$ for 16 nH vacuum inductance.

400kJ,250ns: Ltube=24nH
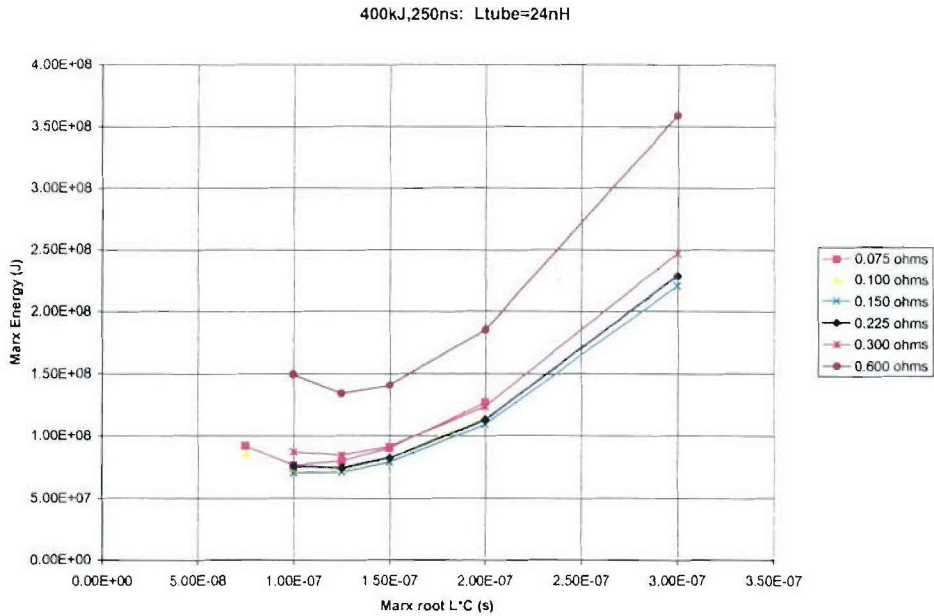
Figure 12. Marx energy required for a 250 ns imploding PRS load 400 kJ krypton k-shell output in a direct drive configuration as a function of $\sqrt{LC}$ and parameterized by $\sqrt{L/C}$ for 24 nH vacuum inductance.
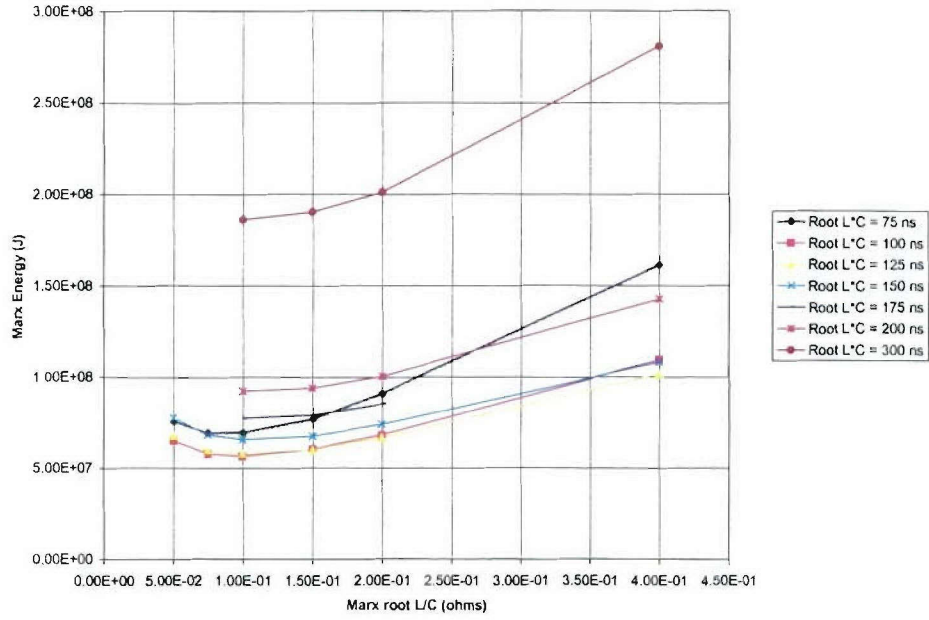
Figure 13. Marx energy required for a 250 ns imploding PRS load 400 kJ krypton k-shell output in a direct drive configuration as a function of $\sqrt{L/C}$ and parameterized by $\sqrt{L \bullet C}$ for 16 nH vacuum inductance.
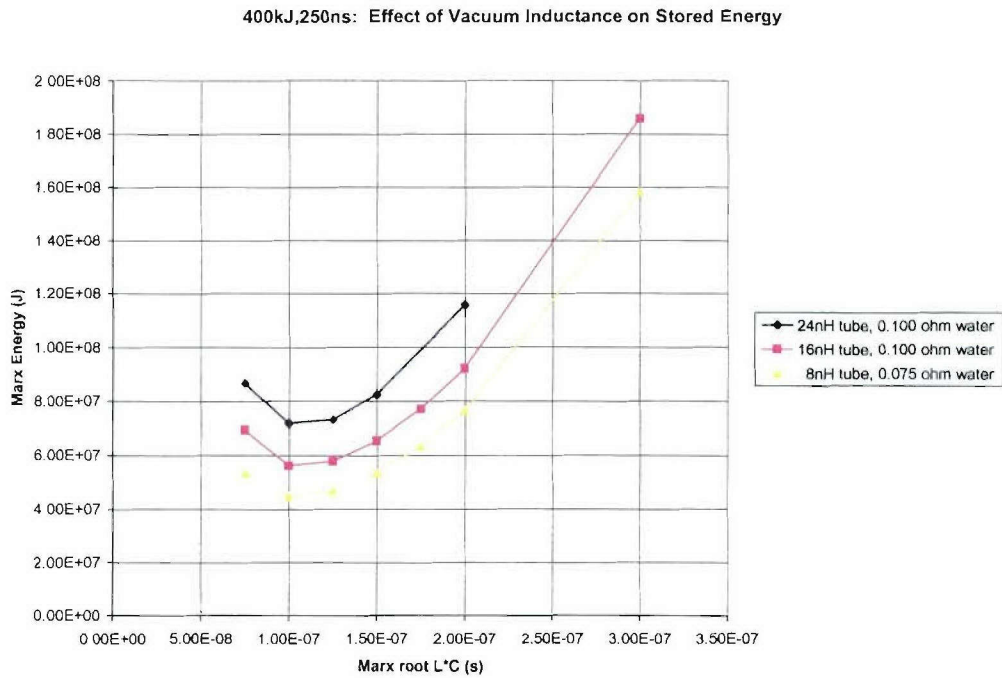
Figure 14. The Marx stored energy increases with vacuum inductance.

These results are understandable by considering the reaction time (or effective impedances) of the various elements in the circuit. The imploding shell load typically has an optimal implosion time occurring just after the time that the peak load current would have occurred with an infinite mass load. Since the implosion time is fixed, this implies an optimum time for the peak current into an infinite mass load. The drive time to peak is roughly $\pi/2$ times the $\sqrt{L \bullet C}$ time and the reaction time of the front end is roughly 2.2 times L/R, where L is the front end inductance and R is the drive line impedance. The resulting time to peak on the load can be estimated by adding these two times in quadrature. For the same drive pulse length, the same load time to peak will occur when L/R is preserved. This is seen in the results as follows: the optimal drive pulse length increases as the drive line impedance increases and the optimal drive line impedance also increases as the front-end impedance increases. (Another way to explain this is to calculate effective impedances and say that the optimums occur when the impedances are matched.)

If we extend plots of minimum stored energy or efficiency, we get an ultimate efficiency of 68% and a minimum stored energy of about 35 MJ as shown in Figure 15 for a 0 nH front end. Using these curves, a 4 nH front end would result in a minimum stored energy of about 40 MJ.
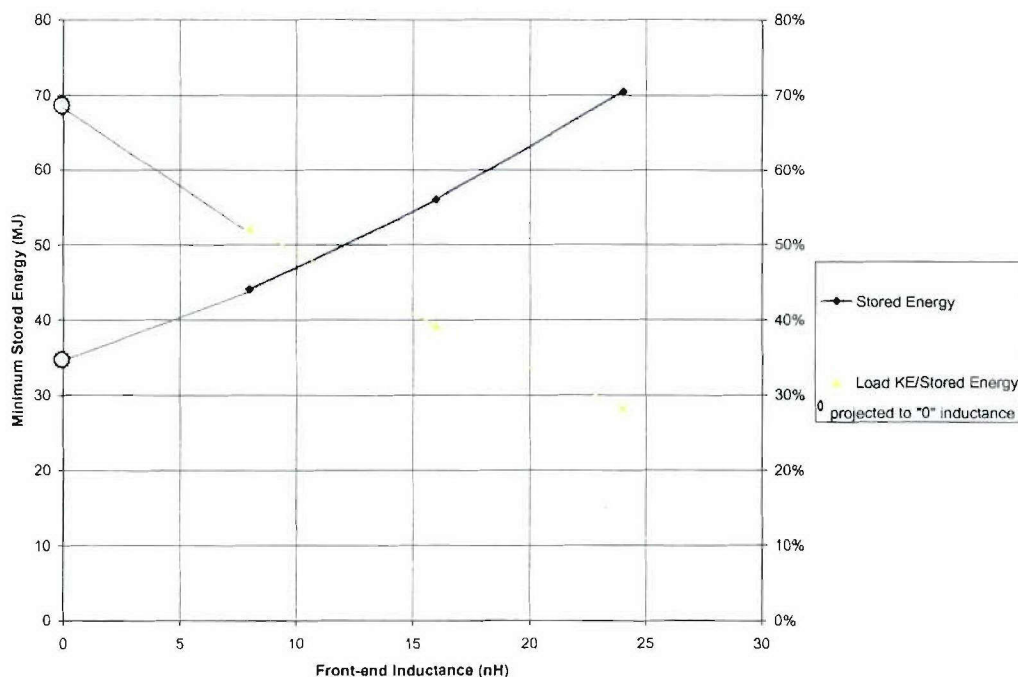
Figure 15. The minimum Marx stored energy and efficiency as a function of front-end inductance.

Peak Load Currents, Initial Load Radius, Load Mass, and Load Kinetic Energy, and Tube Voltage vs. Drive Pulse Length. Another general trend seen in the data in Table 4, is that the peak load current prior to implosion, the initial load radius needed for u=2/7, the load mass, and

the kinetic energy delivered to the load all decrease as the drive pulse $\sqrt{L \bullet C}$ increases. It should be noted that the peak load current required varies quite a lot. The most efficient (lowest stored energy) designs with 8 nH front ends required about 70MA while the lowest efficiency cases required the 50 MA called for in Table 3. The lowest peak load current cases are not necessarily the smallest systems to build!

The peak tube voltage prior to implosion is a bit more complex. Typical Vtube pulse shapes, shown in Figure 16, have two high points. The first occurs at about 250 ns and corresponds to the peak dI/dt of the load current. The second occurs later (around 425 ns for the generic circuit model and about 375 ns for the trace shown in Figure 16) and corresponds to the peak dL/dt of the load, and is typically referred to as the "implosion spike." When the drive pulse is short compared to the implosion time, the dI/dt is the peak tube voltage. The implosion spike is the highest when the drive pulse becomes relatively long. This is seen in the data in Table 4. The time that the peak occurs, Ttube, indicates which high point was the peak. The data shows that as the dI/dt steadily gets lower with increasing $\sqrt{L \bullet C}$, the implosion spike begins to dominate.
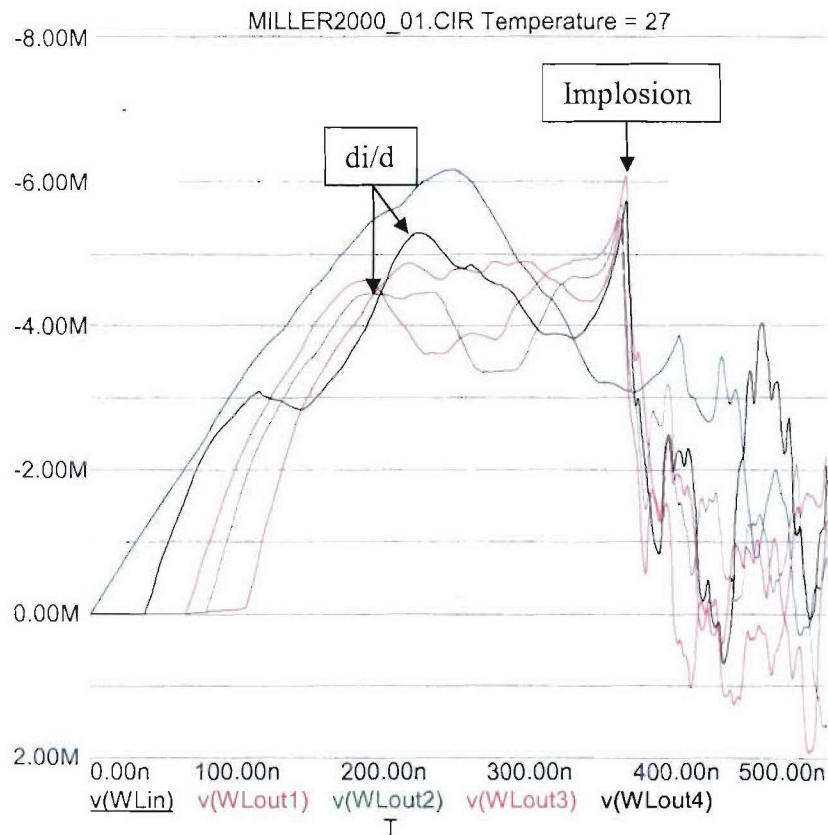
Figure 16. Typical voltage waveforms showing the earlier "di/dt spike" and the later "implosion spike."

Load Length vs. Stored Energy and Tube Voltage. The effect of changing the load length was investigated on a much smaller scale. The runs in Table 5 have the drive/water line impedance fixed at 0.075 Ω and the front-end inductance fixed at 8 nH. Only the load length and the drive pulse length $\sqrt{L \bullet C}$ were scanned. As seen under the Length column, the load length was scanned from 1 cm to 4 cm with a constant length in each block of runs. The $\sqrt{L \bullet C}$ was varied within each block as before. The required stored energy is seen to have a minimum at a 3 cm length. Also, the overall tube voltage tends to be lower for shorter lengths since the implosion spike is reduced.

Table 5. Results of varying load length for the 400 kJ/250 ns, 8 nH case.

400kJ, 250ns Monolithic:			Scan Load length and Marx root L*C									
water: 0.075 ohm constant, 150ns				vacuum: 8.0nH, 4ns			load: u=2/7					
based on runs IDIQ7												
Root L/C	Root L*C	Lmarx	Cmarx	Vmarx	Emarx	Zwater	Vtube	Ttube	Ipkload	Rinit	Length	Mtotal	KE
7.50E-02	7.50E-08	5.63E-09	1.00E-06	1.16E+07	6.72E+07	7.50E-02	8.29E+06	2.13E-07	1.05E+08	1.39E-01	1.00E-02	1.15E-05	1.29E+07
7.50E-02	1.00E-07	7.50E-09	1.33E-06	8.65E+06	4.98E+07	7.50E-02	5.59E+06	2.24E-07	8.60E+07	1.13E-01	1.00E-02	1.03E-05	1.18E+07
7.50E-02	1.25E-07	9.38E-09	1.67E-06	7.66E+06	4.89E+07	7.50E-02	4.53E+06	2.37E-07	7.93E+07	1.02E-01	1.00E-02	9.80E-06	1.13E+07
7.50E-02	1.50E-07	1.13E-08	2.00E-06	7.36E+06	5.41E+07	7.50E-02	4.01E+06	2.46E-07	7.65E+07	9.49E-02	1.00E-02	9.47E-06	1.10E+07
7.50E-02	1.75E-07	1.31E-08	2.33E-06	7.31E+06	6.24E+07	7.50E-02	3.71E+06	2.61E-07	7.48E+07	9.07E-02	1.00E-02	9.25E-06	1.08E+07
7.50E-02	2.00E-07	1.50E-08	2.67E-06	7.45E+06	7.41E+07	7.50E-02	3.53E+06	2.69E-07	7.43E+07	8.84E-02	1.00E-02	9.14E-06	1.06E+07
7.50E-02	3.00E-07	2.25E-08	4.00E-06	8.57E+06	1.47E+08	7.50E-02	4.25E+06	4.35E-07	7.27E+07	8.27E-02	1.00E-02	8.84E-06	1.03E+07
7.50E-02	7.50E-08	5.63E-09	1.00E-06	1.06E+07	5.60E+07	7.50E-02	7.57E+06	2.13E-07	9.32E+07	1.44E-01	2.00E-02	1.65E-05	1.79E+07
7.50E-02	1.00E-07	7.50E-09	1.33E-06	8.15E+06	4.43E+07	7.50E-02	5.27E+06	2.25E-07	7.74E+07	1.21E-01	2.00E-02	1.51E-05	1.65E+07
7.50E-02	1.25E-07	9.38E-09	1.67E-06	7.30E+06	4.44E+07	7.50E-02	4.32E+06	2.37E-07	7.09E+07	1.09E-01	2.00E-02	1.43E-05	1.58E+07
7.50E-02	1.50E-07	1.13E-08	2.00E-06	7.04E+06	4.96E+07	7.50E-02	3.85E+06	2.49E-07	6.79E+07	1.02E-01	2.00E-02	1.39E-05	1.54E+07
7.50E-02	1.75E-07	1.31E-08	2.33E-06	7.04E+06	5.78E+07	7.50E-02	3.68E+06	4.28E-07	6.60E+07	9.76E-02	2.00E-02	1.36E-05	1.50E+07
7.50E-02	2.00E-07	1.50E-08	2.67E-06	7.17E+06	6.85E+07	7.50E-02	4.16E+06	4.30E-07	6.49E+07	9.47E-02	2.00E-02	1.34E-05	1.48E+07
7 50E-02	3.00E-07	2.25E-08	4.00E-06	8.33E+06	1.39E+08	7.50E-02	5.18E+06	4.33E-07	6.31E+07	8.89E-02	2.00E-02	1.30E-05	1.44E+07
7.50E-02	1.00E-07	7.50E-09	1.33E-06	8.11E+06	4.39E+07	7.50E-02	5.25E+06	2.25E-07	7.39E+07	1.27E-01	3.00E-02	1.90E-05	2.04E+07
7.50E-02	1.25E-07	9.38E-09	1.67E-06	7.33E+06	4.48E+07	7.50E-02	4.35E+06	2.37E-07	6.75E+07	1.15E-01	3.00E-02	1.80E-05	1.94E+07
7.50E-02	1.50E-07	1.13E-08	2.00E-06	7.10E+06	5.04E+07	7.50E-02	3.89E+06	2.52E-07	6.44E+07	1.08E-01	3.00E-02	1.75E-05	1.89E+07
7.50E-02	1.75E-07	1.31E-08	2.33E-06	7.17E+06	6.00E+07	7.50E-02	4.35E+06	4.27E-07	6.29E+07	1.04E-01	3.00E-02	1.72E-05	1.86E+07
7.50E-02	7.50E-08	5.63E-09	1.00E-06	1.03E+07	5.33E+07	7.50E-02	7.39E+06	2.13E-07	8.60E+07	1.55E-01	4.00E-02	2.42E-05	2.56E+07
7.50E-02	1.00E-07	7.50E-09	1.33E-06	8.20E+06	4.48E+07	7.50E-02	5.31E+06	2.26E-07	7.20E+07	1.32E-01	4.00E-02	2.24E-05	2.37E+07
7.50E-02	1.25E-07	9.38E-09	1.67E-06	7.48E+06	4.67E+07	7.50E-02	4.44E+06	2.37E-07	6.59E+07	1.20E-01	4.00E-02	2.13E-05	2.27E+07
7.50E-02	1.50E-07	1.13E-08	2.00E-06	7.30E+06	5.33E+07	7.50E-02	4.15E+06	4.25E-07	6.28E+07	1.14E-01	4.00E-02	2.07E-05	2.21E+07
7.50E-02	1.75E-07	1.31E-08	2.33E-06	7.37E+06	6.33E+07	7.50E-02	4.93E+06	4.27E-07	6.10E+07	1.09E-01	4.00E-02	2.03E-05	2.17E+07
7.50E-02	2.00E-07	1.50E-08	2.67E-06	7.57E+06	7.64E+07	7.50E-02	5.48E+06	4.28E-07	5.98E+07	1.06E-01	4.00E-02	2.00E-05	2.14E+07
7.50E-02	3.00E-07	2.25E-08	4.00E-06	8.90E+06	1.58E+08	7.50E-02	6.63E+06	4.31E-07	5.77E+07	1.00E-01	4.00E-02	1.95E-05	2.09E+07

Load Temperature Parameter U vs. System Efficiency. The last scan performed for the 400 kJ/250 ns load was to check the system efficiency against changes to the load temperature parameter u. The runs shown in Table 6 have the driver/water line impedance fixed at 0.1 Ω, the front-end inductance fixed at 8 nH, and the load length at 4 cm. As the value of u is increased, the stored energy in the drive, Emarx, goes to a minimum at u=2/7. It is unknown if this is a general result, but it is intriguing.

400 kJ/100 ns Monolithic Case. The analysis for this shorter implosion time case was a somewhat smaller version of the 250 ns case just described. The table of runs is shown in Table 7 with the data again separated into three parts: the first with all 8 nH front end inductance, and the following two with 16 nH and 24 nH as before. This time however, the different load lengths were used with each front-end inductance, 2, 3, and 4 cm for the 8, 16, and 24 nH front

ends, respectively. A brief length scan is included for the 16 nH case. Shorter load lengths for the lower inductance front ends were preferred since they tended to reduce the tube voltage making the vacuum stack design a little easier. Again the runs for each vacuum inductance are divided into blocks of the same driver/water line impedance, and the drive pulse length $\sqrt{L \bullet C}$ is scanned within each block. Optimum combinations of $\sqrt{L \bullet C}$ and water line impedance were again found for each front-end inductance. A plot of these optimum cases was plotted in Figure 17 despite their different load lengths. The minimum stored energy for the 8 nH front end was 29 MJ, the optimal drive impedance was 0.125 Ω and the $\sqrt{L \bullet C}$ was 50 ns. For the 16 nH front end, it was 0.25 Ω and 50 ns and for the 24 nH front end, it was 0.4 Ω and still 50 ns. The needed driver energy again goes down with front-end inductance. The extrapolated energy required for 0 and 4 nH front ends is shown on Figure 17 to be 18.5 MJ and 25 MJ, respectively. The required stored energy is lower than for the 250 ns implosion drivers, although the pulse must be made twice as fast, the 100 ns implosion only requires 36% greater power from the driver if both front ends could be made 8 nH. But therein lies the rub, the peak tube voltage has increased from 2.4 MV in the 250 ns implosion optimum to about 8.4 MV in the 100 ns implosion optimum. A more self-consistent front-end inductance would be much higher. To make any practical comparison between the various load cases, practical point designs are needed.

Table 6. Load Temperature (u) scan for the 400 kJ/250 ns with 8 nH front-end inductance, $\sqrt{L/C}$ = 0.01 Ω, $\sqrt{L \bullet C}$ = 100 ns, and Load Length = 4 cm.

Root L/C	Root L*C	Lmarx	Cmarx	Vmarx	Emarx	Vtube	Ttube	Ipkload	Rinit	Mtotal	KE	U	Ufactor	Velocity
1.00E-01	1.00E-07	1.00E-08	1.00E-06	1.09E+07	5.96E+07	6.29E+06	2.21E-07	8.17E+07	1.07E-01	4.53E-05	2.96E+07	1.79E-01	6.25E-01	1.1433E+06
1.00E-01	1.00E-07	1.00E-08	1.00E-06	1.00E+07	5.05E+07	5.78E+06	2.21E-07	7.51E+07	1.21E-01	2.97E-05	2.51E+07	2.28E-01	8.00E-01	1.3000E+06
1.00E-01	1.00E-07	1.00E-08	1.00E-06	9.88E+06	4.88E+07	5.68E+06	2.21E-07	7.38E+07	1.29E-01	2.54E-05	2.42E+07	2.57E-01	9.00E-01	1.3805E+06
1.00E-01	1.00E-07	1.00E-08	1.00E-06	9.83E+06	4.83E+07	5.66E+06	2.21E-07	7.35E+07	1.36E-01	2.27E-05	2.40E+07	2.86E-01	1.00E+00	1.4556E+06
1.00E-01	1.00E-07	1.00E-08	1.00E-06	9.87E+06	4.87E+07	5.68E+06	2.21E-07	7.38E+07	1.43E-01	2.06E-05	2.42E+07	3.17E-01	1.11E+00	1.5339E+06
1.00E-01	1.00E-07	1.00E-08	1.00E-06	1.00E+07	5.01E+07	5.76E+06	2.21E-07	7.49E+07	1.52E-01	1.89E-05	2.49E+07	3.57E-01	1.25E+00	1.6253E+06
1.00E-01	1.00E-07	1.00E-08	1.00E-06	1.06E+07	5.63E+07	6.11E+06	2.21E-07	7.94E+07	1.71E-01	1.67E-05	2.80E+07	4.57E-01	1.60E+00	1.8322E+06

Table 7(a). 400 kJ/100 ns data for 8 nH front-end inductance with u = 2/7.

Root L/C	Root L*C	Lmarx	Cmarx	Vmarx	Emarx	Zwater	Vtube	Ttube	Lvac	Ipkload	Rinit	Length	Mtotal	KE
1.00E-01	2.50E-08	2.50E-09	2.50E-07	1.84E+07	4.25E+07	1.00E-01	1.62E+07	1.73E-07	8.00E-09	7.81E+07	5.97E-02	2.00E-02	1.06E-05	1.21E+07
1.00E-01	5.00E-08	5.00E-09	5.00E-07	1.10E+07	3.01E+07	1.00E-01	8.16E+06	1.91E-07	8.00E-09	5.73E+07	4.27E-02	2.00E-02	8.99E-06	1.05E+07
1.00E-01	7.50E-08	7.50E-09	7.50E-07	1.08E+07	4.39E+07	1.00E-01	7.14E+06	2.65E-07	8.00E-09	5.44E+07	3.92E-02	2.00E-02	8.60E-06	1.01E+07
1.00E-01	1.00E-07	1.00E-08	1.00E-06	1.18E+07	6.97E+07	1.00E-01	8.72E+06	2.66E-07	8.00E-09	5.31E+07	3.71E-02	2.00E-02	8.37E-06	9.89E+06
1.00E-01	2.00E-07	2.00E-08	2.00E-06	1.79E+07	3.19E+08	1.00E-01	1.07E+07	2.67E-07	8.00E-09	5.22E+07	3.51E-02	2.00E-02	8.14E-06	9.65E+06
1.50E-01	2.50E-08	3.75E-09	1.67E-07	2.37E+07	4.67E+07	1.50E-01	1.91E+07	1.73E-07	8.00E-09	8.67E+07	6.59E-02	2.00E-02	1.12E-05	1.26E+07
1.50E-01	5.00E-08	7.50E-09	3.33E-07	1.33E+07	2.94E+07	1.50E-01	8.63E+06	1.89E-07	8.00E-09	5.80E+07	4.39E-02	2.00E-02	9.11E-06	1.06E+07
1.50E-01	7.50E-08	1.13E-08	5.00E-07	1.31E+07	4.31E+07	1.50E-01	7.62E+06	2.62E-07	8.00E-09	5.44E+07	3.93E-02	2.00E-02	8.62E-06	1.01E+07
1.50E-01	1.00E-07	1.50E-08	6.67E-07	1.42E+07	6.75E+07	1.50E-01	9.18E+06	2.64E-07	8.00E-09	5.34E+07	3.79E-02	2.00E-02	8.47E-06	9.97E+06
2.00E-01	2.50E-08	5.00E-09	1.25E-07	2.91E+07	5.30E+07	2.00E-01	2.16E+07	1.72E-07	8.00E-09	9.33E+07	7 01E-02	2.00E-02	1 15E-05	1.30E+07
2.00E-01	5.00E-08	1.00E-08	2.50E-07	1.58E+07	3.12E+07	2.00E-01	9.11E+06	1.82E-07	8.00E-09	5.91E+07	4.55E-02	2.00E-02	9.28E-06	1.08E+07
2.00E-01	7.50E-08	1.50E-08	3.75E-07	1.54E+07	4.43E+07	2.00E-01	7.90E+06	2.62E-07	8.00E-09	5.46E+07	4.03E-02	2.00E-02	8.73E-06	1.02E+07
2.00E-01	1.00E-07	2.00E-08	5.00E-07	1.67E+07	6.99E+07	2.00E-01	9.71E+06	2.63E-07	8.00E-09	5.34E+07	3.84E-02	2.00E-02	8.51E-06	1.00E+07
3.00E-01	2.50E-08	7.50E-09	8.33E-08	4.12E+07	7.07E+07	3.00E-01	2.67E+07	1.67E-07	8.00E-09	1.05E+08	7.75E-02	2.00E-02	1.21E-05	1.36E+07
3.00E-01	5.00E-08	1.50E-08	1.67E-07	2.09E+07	3.65E+07	3.00E-01	9.95E+06	1.81E-07	8.00E-09	6.01E+07	4.72E-02	2.00E-02	9.45E-06	1.09E+07
3.00E-01	7.50E-08	2.25E-08	2.50E-07	2.01E+07	5.07E+07	3.00E-01	8.81E+06	2.59E-07	8.00E-09	5.45E+07	4.09E-02	2.00E-02	8.79E-06	1.03E+07
3.00E-01	1.00E-07	3.00E-08	3.33E-07	2.18E+07	7.93E+07	3.00E-01	1.09E+07	2.60E-07	8.00E-09	5.30E+07	3.85E-02	2.00E-02	8.53E-06	1.00E+07

Table 7(b). 400 kJ/100 ns data for 16 nH front-end inductance with u = 2/7.

| Root L/C	Root L*C	Lmarx	Cmarx	Vmarx	Emarx	Zwater	Vtube	Ttube	Lvac	Ipkload	Rinit	Length	Mtotal	KE
3.00E-01	5.00E-08	1.50E-08	1.67E-07	2.18E+07	3.95E+07	3.00E-01	1.41E+07	1.89E-07	1.60E-08	4.76E+07	4.30E-02	4.00E-02	1.28E-05	1.42E+07
3.00E-01	5.00E-08	1.50E-08	1.67E-07	2.20E+07	4.04E+07	3.00E-01	1.43E+07	1.89E-07	1.60E-08	4.99E+07	4.21E-02	3.00E-02	1.09E-05	1.24E+07
3.00E-01	5.00E-08	1.50E-08	1.67E-07	2.28E+07	4.34E+07	3.00E-01	1.48E+07	1.89E-07	1.60E-08	5.36E+07	4.03E-02	2.00E-02	8.73E-06	1.02E+07
3.00E-01	5.00E-08	1.50E-08	1.67E-07	2.54E+07	5.39E+07	3.00E-01	1.65E+07	1.89E-07	1.60E-08	6.26E+07	3.91E-02	1.00E-02	6.08E-06	7.61E+06
Root L/C	Root L*C	Lmarx	Cmarx	Vmarx	Emarx	Zwater	Vtube	Ttube	Lvac	Ipkload	Rinit	Length	Mtotal	KE
1.00E-01	2.50E-08	2.50E-09	2.50E-07	2.37E+07	7.00E+07	1.00E-01	2.29E+07	1.76E-07	1.60E-08	6.13E+07	5.33E-02	3.00E-02	1.23E-05	1.38E+07
1.00E-01	5.00E-08	5.00E-09	5.00E-07	1.42E+07	5.05E+07	1.00E-01	1.25E+07	1.98E-07	1.60E-08	4.79E+07	3.86E-02	3.00E-02	1.05E-05	1.20E+07
1.00E-01	7.50E-08	7.50E-09	7.50E-07	1.41E+07	7.41E+07	1.00E-01	1.14E+07	2.21E-07	1.60E-08	4.61E+07	3.52E-02	3.00E-02	1.00E-05	1.15E+07
1.00E-01	1.00E-07	1.00E-08	1.00E-06	1.54E+07	1.19E+08	1.00E-01	1.30E+07	2.67E-07	1.60E-08	4.55E+07	3.39E-02	3.00E-02	9.80E-06	1.13E+07
2.00E-01	2.50E-08	5.00E-09	1.25E-07	3.14E+07	6.17E+07	2.00E-01	2.77E+07	1.73E-07	1.60E-08	6.79E+07	5.85E-02	3.00E-02	1.29E-05	1.43E+07
2.00E-01	5.00E-08	1.00E-08	2.50E-07	1.79E+07	4.01E+07	2.00E-01	1.33E+07	1.91E-07	1.60E-08	4.85E+07	3.97E-02	3.00E-02	1.06E-05	1.21E+07
2.00E-01	7.50E-08	1.50E-08	3.75E-07	1.76E+07	5.84E+07	2.00E-01	1.15E+07	2.06E-07	1.60E-08	4.63E+07	3.63E-02	3.00E-02	1.01E-05	1.16E+07
2.00E-01	1.00E-07	2.00E-08	5.00E-07	1.92E+07	9.25E+07	2.00E-01	1.33E+07	2.66E-07	1.60E-08	4.58E+07	3.50E-02	3.00E-02	9.96E-06	1.15E+07
3.00E-01	2.50E-08	7.50E-09	8.33E-08	4.03E+07	6.77E+07	3.00E-01	3.26E+07	1.73E-07	1.60E-08	7.48E+07	6.36E-02	3.00E-02	1.34E-05	1.49E+07
3.00E-01	5.00E-08	1.50E-08	1.67E-07	2.20E+07	4.04E+07	3.00E-01	1.43E+07	1.89E-07	1.60E-08	4.99E+07	4.21E-02	3.00E-02	1.09E-05	1.24E+07
3.00E-01	7.50E-08	2.25E-08	2.50E-07	2.14E+07	5.75E+07	3.00E-01	1.18E+07	1.98E-07	1.60E-08	4.67E+07	3.73E-02	3.00E-02	1.03E-05	1.18E+07
3.00E-01	1.00E-07	3.00E-08	3.33E-07	2.34E+07	9.11E+07	3.00E-01	1.38E+07	2.64E-07	1.60E-08	4.60E+07	3.55E-02	3.00E-02	1.00E-05	1.15E+07
4.00E-01	2.50E-08	1.00E-08	6.25E-08	5.00E+07	7.80E+07	4.00E-01	3.71E+07	1.72E-07	1.60E-08	8.10E+07	6.80E-02	3.00E-02	1.39E-05	1.53E+07
4.00E-01	5.00E-08	2.00E-08	1.25E-07	2.61E+07	4.26E+07	4.00E-01	1.51E+07	1.81E-07	1.60E-08	5.02E+07	4.27E-02	3.00E-02	1.10E-05	1.25E+07
4.00E-01	7.50E-08	3.00E-08	1.88E-07	2.54E+07	6.05E+07	4.00E-01	1.21E+07	1.97E-07	1.60E-08	4.68E+07	3.77E-02	3.00E-02	1.03E-05	1.18E+07
4.00E-01	1.00E-07	4.00E-08	2.50E-07	2.73E+07	9.31E+07	4.00E-01	1.43E+07	2.63E-07	1.60E-08	4.58E+07	3.61E-02	3.00E-02	1.01E-05	1.16E+07

Table 7(c). 400 kJ/100 ns data for 24 nH front-end inductance with u = 2/7.

Root L/C	Root L*C	Lmarx	Cmarx	Vmarx	Emarx	Zwater	Vtube	Ttube	Lvac	Ipkload	Rinit	Length	Mtotal	KE
1.00E-01	2.50E-08	2.50E-09	2.50E-07	3.09E+07	1.19E+08	1.00E-01	3.11E+07	1.77E-07	2.40E-08	5.97E+07	4.76E-02	2.00E-02	9.49E-06	1.10E+07
1.00E-01	5.00E-08	5.00E-09	5.00E-07	1.82E+07	8.32E+07	1.00E-01	1.71E+07	2.02E-07	2.40E-08	4.96E+07	3.48E-02	2.00E-02	8.11E-06	9.62E+06
Root L/C	Root L*C	Lmarx	Cmarx	Vmarx	Emarx	Zwater	Vtube	Ttube	Lvac	Ipkload	Rinit	Length	Mtotal	KE
1.00E-01	2.50E-08	2.50E-09	2.50E-07	2.88E+07	1.04E+08	1.00E-01	2.90E+07	1.77E-07	2.40E-08	5.38E+07	5.09E-02	4.00E-02	1.39E-05	1.53E+07
1.00E-01	5.00E-08	5.00E-09	5.00E-07	1.74E+07	7.56E+07	1.00E-01	1.63E+07	2.02E-07	2.40E-08	4.30E+07	3.68E-02	4.00E-02	1.18E-05	1.33E+07
1.00E-01	7.50E-08	7.50E-09	7.50E-07	1.73E+07	1.12E+08	1.00E-01	1.53E+07	2.24E-07	2.40E-08	4.18E+07	3.40E-02	4.00E-02	1.13E-05	1.28E+07
1.00E-01	1.00E-07	1.00E-08	1.00E-06	1.88E+07	1.77E+08	1.00E-01	1.70E+07	2.69E-07	2.40E-08	4.13E+07	3.28E-02	4.00E-02	1.11E-05	1.26E+07
2.00E-01	2.50E-08	5.00E-09	1.25E-07	3.53E+07	7.79E+07	2.00E-01	3.31E+07	1.75E-07	2.40E-08	5.77E+07	5.40E-02	4.00E-02	1.43E-05	1.57E+07
2.00E-01	5.00E-08	1.00E-08	2.50E-07	2.06E+07	5.32E+07	2.00E-01	1.71E+07	1.97E-07	2.40E-08	4.36E+07	3.79E-02	4.00E-02	1.20E-05	1.34E+07
2.00E-01	7.50E-08	1.50E-08	3.75E-07	2.05E+07	7.90E+07	2.00E-01	1.54E+07	2.14E-07	2.40E-08	4.21E+07	3.47E-02	4.00E-02	1.15E-05	1.29E+07
2.00E-01	1.00E-07	2.00E-08	5.00E-07	2.22E+07	1.23E+08	2.00E-01	1.71E+07	2.67E-07	2.40E-08	4.15E+07	3.35E-02	4.00E-02	1.13E-05	1.27E+07
4.00E-01	2.50E-08	1.00E-08	6.25E-08	5.01E+07	7.84E+07	4.00E-01	4.16E+07	1.73E-07	2.40E-08	6.51E+07	6.00E-02	4.00E-02	1.51E-05	1.65E+07
4.00E-01	5.00E-08	2.00E-08	1.25E-07	2.77E+07	4.81E+07	4.00E-01	1.88E+07	1.89E-07	2.40E-08	4.48E+07	4.01E-02	4.00E-02	1.23E-05	1.38E+07
4.00E-01	7.50E-08	3.00E-08	1.88E-07	2.70E+07	6.83E+07	4.00E-01	1.56E+07	2.04E-07	2.40E-08	4.23E+07	3.60E-02	4.00E-02	1.17E-05	1.31E+07
4.00E-01	1.00E-07	4.00E-08	2.50E-07	2.92E+07	1.06E+08	4.00E-01	1.75E+07	2.66E-07	2.40E-08	4.17E+07	3.47E-02	4.00E-02	1.15E-05	1.29E+07
5.00E-01	5.00E-08	2.50E-08	1.00E-07	3.14E+07	4.94E+07	5.00E-01	1.95E+07	1.87E-07	2.40E-08	4.52E+07	4.09E-02	4.00E-02	1.24E-05	1.39E+07
5.00E-01	7.50E-08	3.75E-08	1.50E-07	3.05E+07	6.96E+07	5.00E-01	1.59E+07	1.97E-07	2.40E-08	4.26E+07	3.68E-02	4.00E-02	1.18E-05	1.33E+07
5.00E-01	1.00E-07	5.00E-08	2.00E-07	3.30E+07	1.09E+08	5.00E-01	1.80E+07	2.64E-07	2.40E-08	4.16E+07	3.47E-02	4.00E-02	1.15E-05	1.29E+07
6.00E-01	2.50E-08	1.50E-08	4.17E-08	6.77E+07	9.55E+07	6.00E-01	5.03E+07	1.72E-07	2.40E-08	7.34E+07	6.63E-02	4.00E-02	1.58E-05	1.73E+07
6.00E-01	5.00E-08	3.00E-08	8.33E-08	3.52E+07	5.15E+07	6.00E-01	2.03E+07	1.81E-07	2.40E-08	4.55E+07	4.17E-02	4.00E-02	1.26E-05	1.40E+07
6.00E-01	7.50E-08	4.50E-08	1.25E-07	3.42E+07	7.33E+07	6.00E-01	1.63E+07	1.97E-07	2.40E-08	4.27E+07	3.69E-02	4.00E-02	1.18E-05	1.33E+07

100 kJ/250 ns Modular Case. The analysis for this case using the generic circuit was quite limited and only intended to explore a region of the design space that might be reasonable for a point design. No attempt was made to find optimums as for the 400 kJ/250 ns case. For the runs shown in Table 8, the generic circuit modeled a single module. In these runs, two vacuum inductances were modeled: 8 nH in the first block of runs and 16 nH for all the rest. Next, two load lengths were modeled: 2 cm for all the 8 nH cases and the first two blocks of 16 nH cases, 4 cm lengths were used in the bottom two blocks. Next, two drive/water line impedances were modeled: 0.1 Ω for the 8 nH cases and both 0.1 Ω and 0.2 Ω for each load length of the 16 nH front ends.
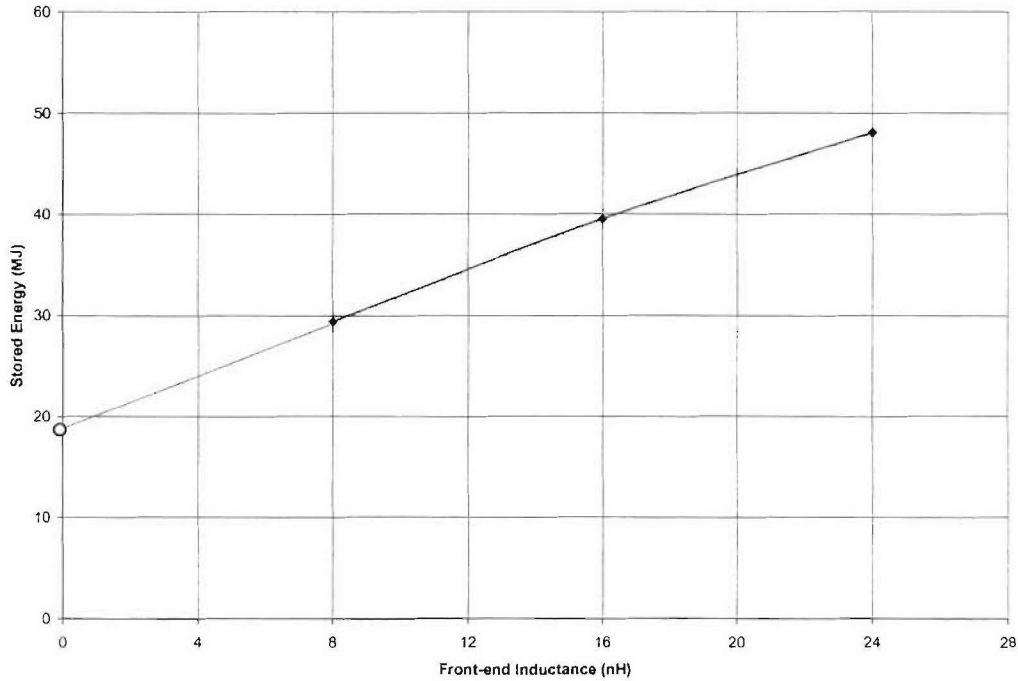
Figure 17. Minimum stored energy versus front-end inductance for the 400 kJ/100 ns case.

The required stored energy for a single module which produces 100 kJ x-rays is roughly half that of the 400 kJ monolithic case. This means that twice the stored energy will be needed in a four-module system that produces the same output.

3.1.4 Conclusion.

The generic modeling produced the following results:

- There are drive pulse lengths and drive impedances that minimize the stored energy (maximize the system efficiency) for each front-end inductance. Lowering the front-end inductance also reduces the stored energy required.
- The peak load currents, initial load radius, load mass, and load kinetic energy all decrease for longer drive pulse lengths given, of course, that the yield and the implosion time stayed fixed. The tube voltage also decreases for longer pulse lengths until the implosion spike determines the peak.
- There are load lengths that minimize the stored energy and shortening the load can greatly reduce the implosion spike seen on the tube.
- For one case, the optimum load-temperature parameter u=2/7 corresponded to the maximum system efficiency. It is unknown if this result applies generally.

28

Table 8. Scans of driver time constant, impedance, and load length for vacuum inductances of 8 and 16 nH for the 100 kJ/250 ns case.

Root L/C	Root L*C	Lmarx	Cmarx	Vmarx	Emarx	Zwater	Vtube	Ttube	Lvac	Ipkload	Rinit	Length	Mtotal	KE
1.00E-01	7.50E-08	7.50E-09	7.50E-07	9.13E+06	3.12E+07	1.00E-01	5.91E+06	2.05E-07	8.00E-09	6.85E+07	1.50E-01	2.00E-02	8.42E-06	8.73E+06
1.00E-01	1.00E-07	1.00E-08	1.00E-06	6.85E+06	2.35E+07	1.00E-01	3.94E+06	2.20E-07	8.00E-09	5.48E+07	1.23E-01	2.00E-02	7.61E-06	7.93E+06
1.00E-01	1.25E-07	1.25E-08	1.25E-06	6.04E+06	2.28E+07	1.00E-01	3.14E+06	2.29E-07	8.00E-09	4.91E+07	1.09E-01	2.00E-02	7.16E-06	7.49E+06
1.00E-01	1.50E-07	1.50E-08	1.50E-06	5.81E+06	2.53E+07	1.00E-01	2.75E+06	2.37E-07	8.00E-09	4.69E+07	1.02E-01	2.00E-02	6.94E-06	7.27E+06
1.00E-01	1.75E-07	1.75E-08	1.75E-06	5.78E+06	2.92E+07	1.00E-01	2.71E+06	4.25E-07	8.00E-09	4.53E+07	9.69E-02	2.00E-02	6.76E-06	7.09E+06
1.00E-01	2.00E-07	2.00E-08	2.00E-06	5.88E+06	3.45E+07	1.00E-01	3.07E+06	4.27E-07	8.00E-09	4.45E+07	9.38E-02	2.00E-02	6.65E-06	6.98E+06
1.00E-01	3.00E-07	3.00E-08	3.00E-06	6.82E+06	6.98E+07	1.00E-01	3.82E+06	4.30E-07	8.00E-09	4.33E+07	8.81E-02	2.00E-02	6.44E-06	6.78E+06
1.00E-01	7.50E-08	7.50E-09	7.50E-07	9.89E+06	3.67E+07	1.00E-01	7.94E+06	2.18E-07	1.60E-08	5.46E+07	1.23E-01	2.00E-02	7.61E-06	7.92E+06
1.00E-01	1.00E-07	1.00E-08	1.00E-06	7.55E+06	2.85E+07	1.00E-01	5.60E+06	2.35E-07	1.60E-08	4.64E+07	1.02E-01	2.00E-02	6.95E-06	7.28E+06
1.00E-01	1.25E-07	1.25E-08	1.25E-06	6.73E+06	2.83E+07	1.00E-01	4.65E+06	2.50E-07	1.60E-08	4.34E+07	9.23E-02	2.00E-02	6.59E-06	6.93E+06
1.00E-01	1.50E-07	1.50E-08	1.50E-06	6.46E+06	3.13E+07	1.00E-01	4.18E+06	2.62E-07	1.60E-08	4.20E+07	8.68E-02	2.00E-02	6.39E-06	6.73E+06
2.00E-01	7.50E-08	1.50E-08	3.75E-07	1.66E+07	5.18E+07	2.00E-01	1.08E+07	2.05E-07	1.60E-08	6.40E+07	1.42E-01	2.00E-02	8.18E-06	8.50E+06
2.00E-01	1.00E-07	2.00E-08	5.00E-07	1.22E+07	3.71E+07	2.00E-01	7.00E+06	2.19E-07	1.60E-08	5.06E+07	1.15E-01	2.00E-02	7.36E-06	7.68E+06
2.00E-01	1.25E-07	2.50E-08	6.25E-07	1.05E+07	3.48E+07	2.00E-01	5.47E+06	2.29E-07	1.60E-08	4.53E+07	1.01E-01	2.00E-02	6.89E-06	7.21E+06
2.00E-01	1.50E-07	3.00E-08	7.50E-07	1.00E+07	3.76E+07	2.00E-01	4.74E+06	2.37E-07	1.60E-08	4.31E+07	9.33E-02	2.00E-02	6.63E-06	6.96E+06
1.00E-01	7.50E-08	7.50E-09	7.50E-07	9.40E+06	3.31E+07	1.00E-01	7.55E+06	2.18E-07	1.60E-08	4.99E+07	1.32E-01	4.00E-02	1.11E-05	1.14E+07
1.00E-01	1.00E-07	1.00E-08	1.00E-06	7.35E+06	2.70E+07	1.00E-01	5.45E+06	2.36E-07	1.60E-08	4.26E+07	1.11E-01	4.00E-02	1.02E-05	1.05E+07
1.00E-01	1.25E-07	1.25E-08	1.25E-06	6.64E+06	2.75E+07	1.00E-01	4.59E+06	2.51E-07	1.60E-08	3.96E+07	1.01E-01	4.00E-02	9.77E-06	1.01E+07
1.00E-01	1.50E-07	1.50E-08	1.50E-06	6.44E+06	3.11E+07	1.00E-01	4.18E+06	2.63E-07	1.60E-08	3.82E+07	9.60E-02	4.00E-02	9.51E-06	9.81E+06
2.00E-01	7.50E-08	1.50E-08	3.75E-07	1.52E+07	4.36E+07	2.00E-01	9.87E+06	2.05E-07	1.60E-08	5.72E+07	1.50E-01	4.00E-02	1.19E-05	1.21E+07
2.00E-01	1.00E-07	2.00E-08	5.00E-07	1.14E+07	3.26E+07	2.00E-01	6.56E+06	2.20E-07	1.60E-08	4.56E+07	1.22E-01	4.00E-02	1.07E-05	1.10E+07
2.00E-01	1.25E-07	2.50E-08	6.25E-07	1.01E+07	3.18E+07	2.00E-01	5.24E+06	2.29E-07	1.60E-08	4.11E+07	1.08E-01	4.00E-02	1.01E-05	1.04E+07
2.00E-01	1.50E-07	3.00E-08	7.50E-07	9.67E+06	3.51E+07	2.00E-01	4.58E+06	2.37E-07	1.60E-08	3.90E+07	1.01E-01	4.00E-02	9.77E-06	1.01E+07
2.00E-01	1.75E-07	3.50E-08	8.75E-07	9.62E+06	4.05E+07	2.00E-01	4.51E+06	4.25E-07	1.60E-08	3.77E+07	9.62E-02	4.00E-02	9.52E-06	9.82E+06
2.00E-01	2.00E-07	4.00E-08	1.00E-06	9.78E+06	4.79E+07	2.00E-01	5.10E+06	4.27E-07	1.60E-08	3.70E+07	9.32E-02	4.00E-02	9.38E-06	9.67E+06
2.00E-01	3.00E-07	6.00E-08	1.50E-06	1.13E+07	9.55E+07	2.00E-01	6.34E+06	4.31E-07	1.60E-08	3.58E+07	8.70E-02	4.00E-02	9.05E-06	9.36E+06

Based on this analysis, we can generate the list of objectives for the drivers, the vacuum inductance, and PRS load length shown in Table 9.

Table 9. Sub-system design objectives derived from system analysis.

Parameter/Design Point	400 kJ/250 ns	400 kJ/100 ns	100 kJ/250 ns
$\sqrt{L \bullet C}$	100 to 125 ns	50 ns	100 to 125 ns
$\sqrt{L/C}$	"matched" to front-end L 0.06 Ω for 8 nH 0.1 Ω for 16 nH 0.15 Ω for 24 nH	"matched" to front-end L 0.125 Ω for 8 nH 0.25 Ω for 16 nH 0.4 Ω for 24 nH	"matched" to front-end L 0.1 Ω for 16 nH
Load Length	3 cm is more efficient than 1, 2 or 4 cm	3, 4 cm are more efficient than 1, 2 cm but stack voltage may be more important	4 cm is more efficient than 2 cm
Front-end L	Minimum possible	Minimum possible	Minimum possible

3.2   POINT DESIGN DESCRIPTIONS.

During the course of our study, we generated several point designs to investigate the R&D issues and trade-offs associated with realizing the sub-systems postulated in the Systems Analysis.

Each point design consisted of a sketch of the hardware containing sufficient detail to evaluate if the concept could actually be built and to provide circuit element values for subsystems (primary energy store, water pulse compression/transmission lines, vacuum power flow) for use in modeling. The various Point Designs developed are indicated in Table 10.

Initially we assumed a conservative front-end inductance (22 nH) and Marx Generator time constant ($\sqrt{L \bullet C} = 300$ ns) because we were targeting a five-year fielding schedule and did not want to depart too far from the state-of-the-art. As our work evolved, the system analysis pushed us in the direction of faster $\sqrt{L \bullet C}$ and the urgency of having a module available in five years diminished. This combination influenced us to focus on Point Designs with more aggressive front-end inductance (10 – 15 nH) and faster Marx stage time constants ($\sqrt{L \bullet C} = 175$ ns). As will be discussed in following sections, a realistic R&D program could provide the required technology in a few years of effort.

Table 10. Point Designs generated for this effort (in roughly chronological order of development).

| Case	Driver Configuration	Driver $\sqrt{L \bullet C}$	Front-end Inductance	Comment
100 kJ/250 ns	MGD-Schlitt Line	300 ns	22 nH	Unresolved connection issues
100 kJ/250 ns	LTD-Schlitt Line	300 ns	22 nH	Unresolved connection issues
100 kJ/250 ns	MGD-Transfer Capacitor-Schlitt Line	300 ns	15 nH	Unresolved connection issues
100 kJ/250 ns	MGD-Peaking Capacitor-Schlitt Line	300 ns	15 nH	feasible
100 kJ/250 ns	MGD-Schlitt Line	175 ns	15 nH	feasible
100 kJ/250 ns	LTD-Schlitt Line	175 ns	15 nH	feasible
400 kJ/250 ns	MGD-Transfer Capacitor-Schlitt Line	500 ns	8 nH	feasible
400 kJ/250 ns	MGD-Peaking Capacitor-Schlitt Line	300 ns	8 nH	feasible
400 kJ/250 ns	MGD-Schlitt Line	175 ns	8 nH	feasible

3.2.1 100 kJ/250 ns Modular Direct-Drive System Point Designs.

In this modular 250 ns implosion-time system concept, four 30-to-37 MA modules drive separate sources as illustrated in Figure 18. (At the onset of this study, 30 MA was taken to be the peak current required to produce 100 kJ of krypton k-line radiation from a 250 µs implosion.

Subsequent refinements in PRS modeling have raised that estimate, with the consensus now being ≈37 MA. This represents a marginal increase in design issues but does not rule out any of the concepts considered.) One such single module could be used for some subset of effects tests. The four-module system provides for larger area tests. Four centimeter long shell loads with a 10:1 compression ratio are assumed with the pinch axes horizontal and located around an approximately ½ meter diameter circle. This arrangement is shown schematically in Figure 19 depicting the geometrical constraint at the load that was used in the optimization of MITLs, tube and water lines back to the prime power.
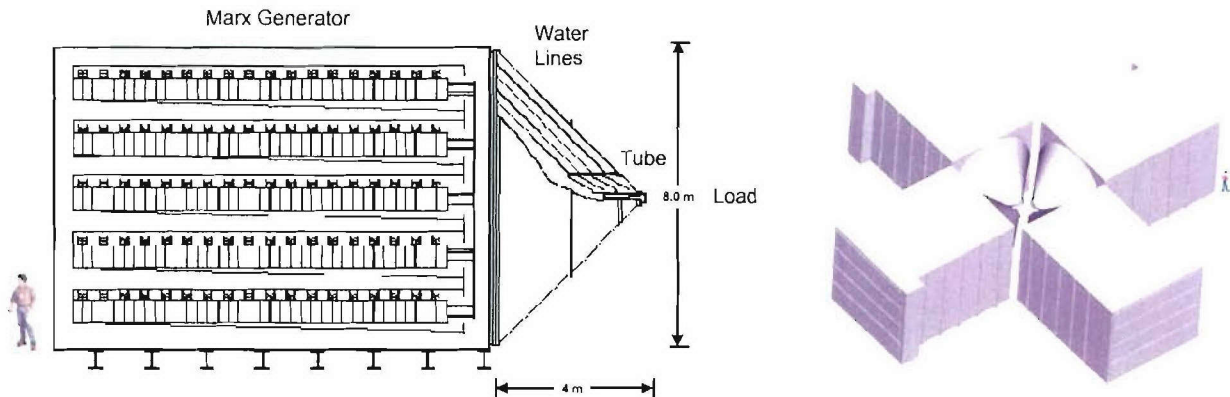

Figure 18. 100 kJ/250 ns direct drive module layout (MGD option).
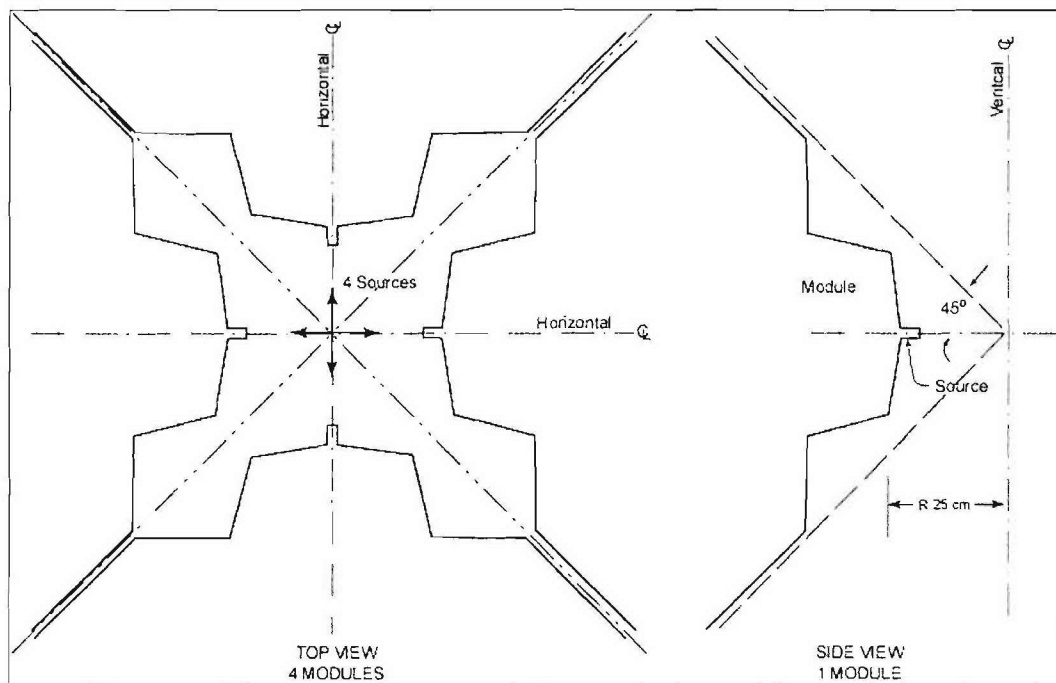
Figure 19. Module and Source Arrangement used for the 100 kJ/250 ns Point Design.

Given the energy required (25 to 50 MJ), the spatial extent of the prime energy would be too large to connect directly to the load. Its frontal area would extend outside the conical volume allocated to each module. The required power flow convergence can be accomplished by conical water transmission lines that also beneficially modify the current wave shape. During Decade machine studies it was shown that such an arrangement could produce an initial early peak in the current waveform from a relatively slow Marx generator. As Lee Schlitt first analyzed them, these water lines have been called "Schlitt lines." By using the Schlitt line and fixing the electrical length at 73 ns in our Point Design (versus the ~150 ns used in our System Analysis), the required energy stored can be reduced by ~ 15%. The constraints for the MITL length are discussed in Section 5. The result of the iterative "front-end" design process is shown in Figure 20. The resulting design has a roughly 9 x 9 m surface available for connecting to the primary energy store. As sketched in Figure 20, this system may have space for between 30 to 35 1.0 to 1.2 m diameter feed-ports.
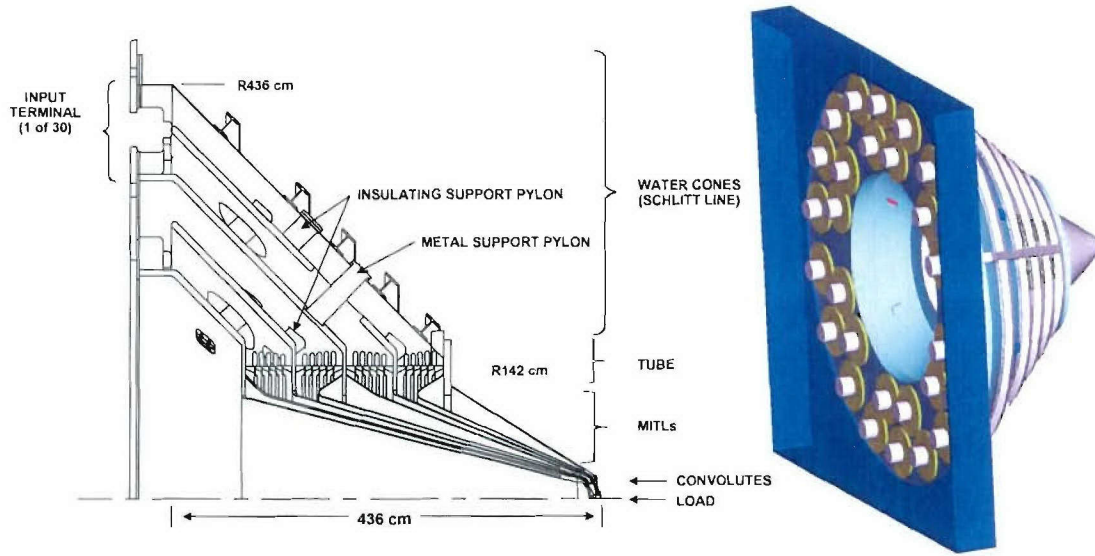
Figure 20. Front-end sketch and feed port scheme for connection to the prime power source.

Fast Marx Stage $\sqrt{L \bullet C}$ = 300 ns Point Designs. Based on concepts to be presented in Section 6, we believe the state-of-the-art for capacitor-switch stage $\sqrt{L \bullet C}$ could be rapidly advanced from 500 ns to 300 ns. This stage $\sqrt{L \bullet C}$ should be preserved as either Marx generators or LTD's are built up as needed to deliver the required energy to the load. We developed Point Designs for three technology options for the $\sqrt{L \bullet C}$ = 300 ns, 100 kJ/250 ns module:

1. Direct-drive by Marx Generator Driver (MGD)
2. Direct-drive by a linear transformer driver (LTD)
3. MGD + water pulse compression.

Direct Drive by a MGD and Schlitt Line. This was the first point design analyzed and served to set various pulsed power issues in perspective. At the time the estimated peak current to produce 100 kJ of Kr-K-line radiation from one of four such modules was 30 MA. Subsequent refinements in PRS yield modeling (the MQK model) raised the requirement for this case to 37 MA, thus further increasing some of the scale factors considered here.

The essential features of this configuration are the front end shown in Figure 20 driven by a Marx generator array attached to the input terminals shown. The Marx drive has a characteristic time of 300 ns and characteristic impedance of 0.1 Ω to match the Schlitt lines. The Schlitt line length must be maintained at ≈75 ns to preserve the early current pulse peak resulting from reflections within the lines.

The features of this configuration can be represented by the simplified circuit shown in Figure 21.
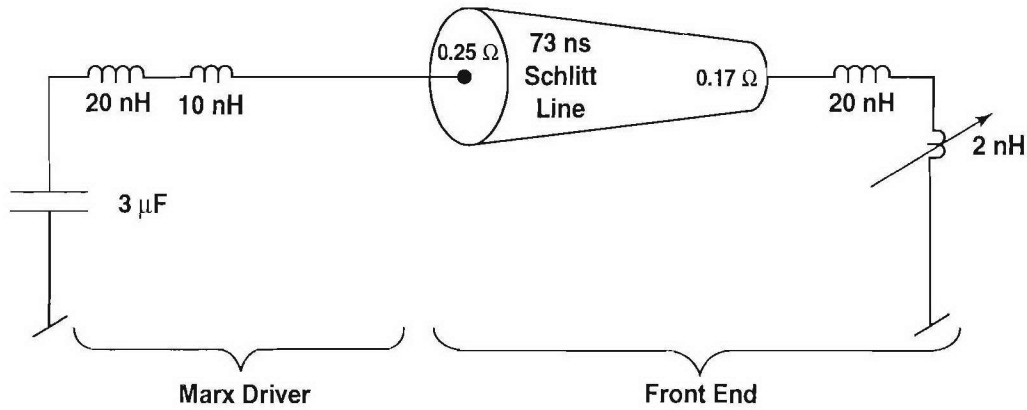
Figure 21. Circuit model for the 100 kJ/250 ns MGD Point Design.

The inductance budget for this Point Design Marx driver was 30 nH total with 10 nH set aside for buswork and connections. This Marx generator driver would be an array of parallel Marxes each comprised of series stages. The Marx array requirements set the Marx stage requirements, that is, the Marx array $\sqrt{L \bullet C}$ sets stage $\sqrt{L \bullet C}$ and stage impedance $\sqrt{L_s / C_s}$ is $\frac{m}{n}\sqrt{L_m / C_m}$ where m is the number of Marxes in parallel and n the number of series stage in a Marx. Stage inductance must be lower by the amount of reflected connection buswork inductance. Our choice of Marx $\sqrt{L \bullet C}$ of 300 ns is guided by the data in Table 11, which shows 300 ns is not far beyond the present state of the art demonstrated for large systems. Marx stage issues will be discussed in Section 6.

Table 11. Demonstrated driver characteristics.

Driver	L_s	$\sqrt{L \bullet C}$
Blackjack 5	546 nH	880 ns
Falcon	300 nH	575 ns
DECADE QUAD	400 nH	663 ns
Eagle	342 nH	500 ns
PBFA I	375 nH	512 ns
PBFA II	343 nH	480 ns
Antares	230 nH	980 ns
Hermes III	408 nH	
Hermes II	375 nH	
OWL II	392 nH	600 ns
Speed	325 nH	
ACE 4	120 nH	424 ns

This circuit model was used for initial performance estimates while a more detailed circuit code reflecting the multi-parallelism of the concept was benchmarked. This translation of the Point Design for the water and vacuum transmission lines into a fairly detailed MICROCAP design electrical model is shown in Figure 22. Further details of the water cones and vacuum transmission line will be presented in Section 5. This detailed model validated the generic modeling results of our system analysis. Waveforms associated with the model for this initial point design are shown in Figures 23 and 24.

Modeling shows the performance potential of this point design. To further evaluate feasibility the Marx driver and its connection to the front end were studied.

To determine the scale of the Marx driver, the characteristic volume of different large systems was compared as in Table 12. A scaling factor of volume (m³) per megavolt-megajoule is approximately constant over a wide range of systems. Conceptually, both voltage and total energy affect system volume. Taking the lowest scale factor (27 m³/MV-MJ) we would estimate a volume of approximately 8000 m³. (5.8 MV * 50 MJ ● 27 m³ / MV*MJ = 7,840 m³.) R&D in low inductance driver configurations and higher energy density energy storage could advantageously affect system size. Given the constraint that the prime power driver must mate to the front end and also fit within the projected volume of a truncated cone, two extremes of volume shape as shown in Figure 25, may be considered. A simple rectangular projection of an approximately 8.8 m by 8.8 m square interface with the front end results in a volume 100 m long. This length, in oil, corresponds to 500 ns and clearly rules out such a choice for a 300 ns direct drive. If use is made of the entire available projected conical volume from a 9 m diameter to a 40 m diameter 16 m back, the electrical transit time is a more reasonable ~80 ns. Utilization of this volume to package many parallel-connected Marx generators will be challenging.
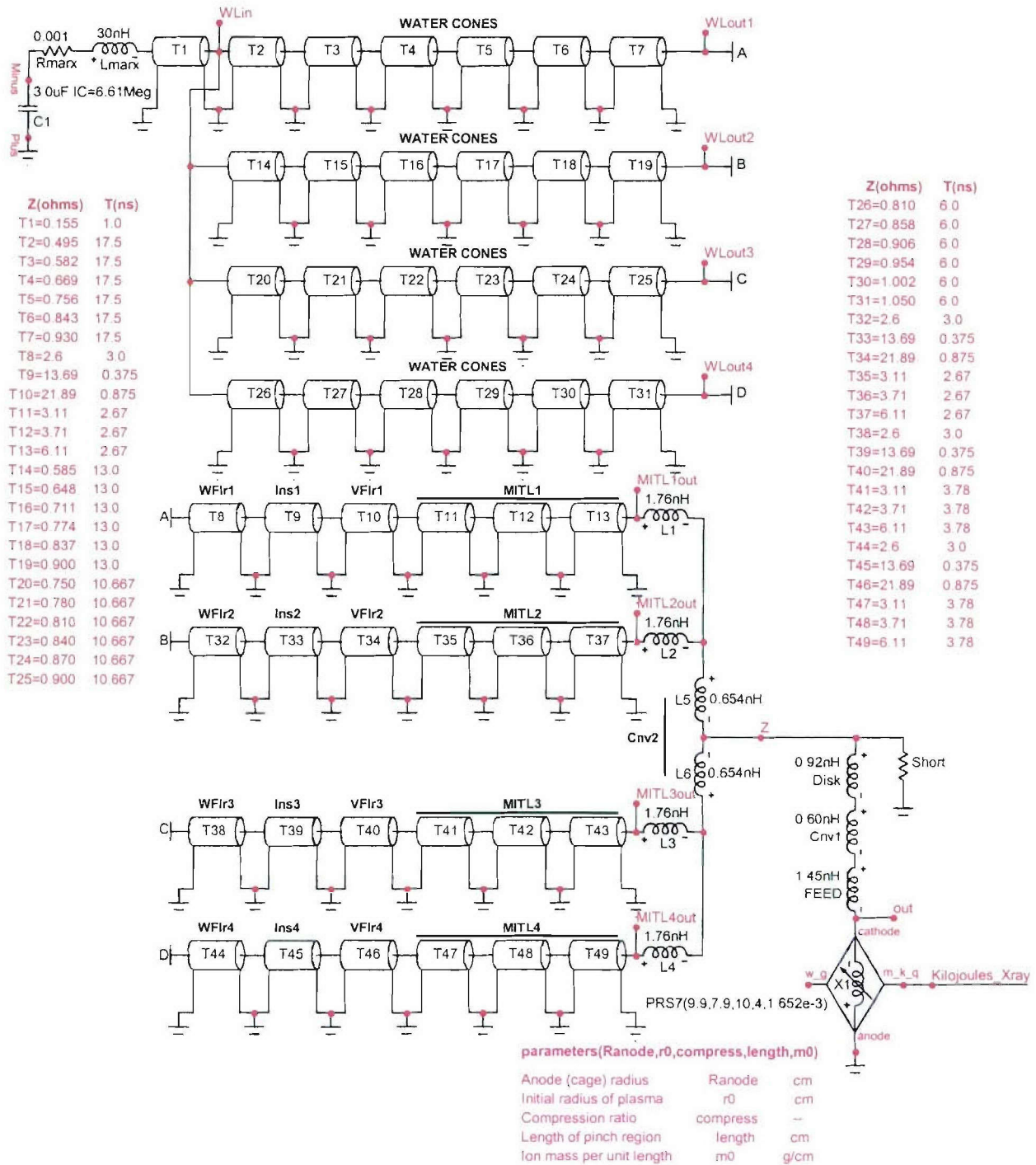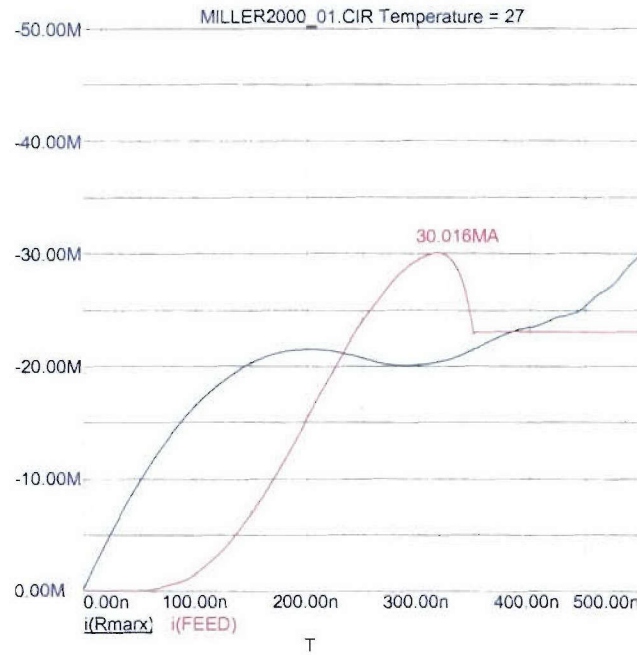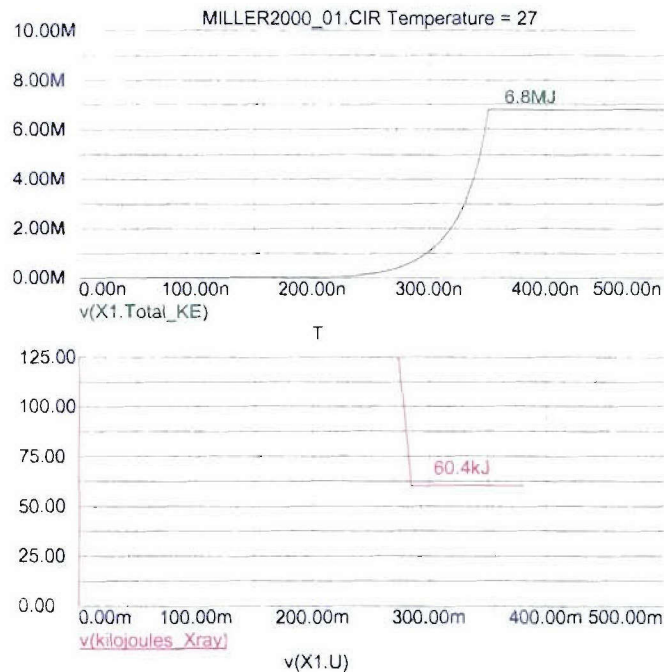
Figure 22. Circuit model for the 100 kJ/250 ns Point Design.

Figure 23. Marx current (blue trace) and load current (red trace) for the Point Design of Figure 22.


Figure 24. MICROCAP model results for Point Design of Figure 22 showing total load kinetic energy and Mosher model estimate for krypton k-shell output. Note that this result is consistent with our revised estimate that ≈37 MA will be required to generate 100 kJ of krypton k-shell radiation.

Table 12. Data used to calculate Marx volume scaling factor.

|	m³ / MV • MJ	Scaling Factor
GS1	17 m³ / 0.9 MV • 0.64 MJ	29.4
Decade Quad	138 m³ / 1.2 MV • 3.2 MJ	35.7
Eagle	100 m³ / 3.8 MV • 0.94 MJ	27.8
BJ5 (RIP)	680 m³ / 6 MV • 2.7 MJ	41.7
PBFA-Z	2.3 x 10³ m³ / 6 MV • 14 MJ	27.0
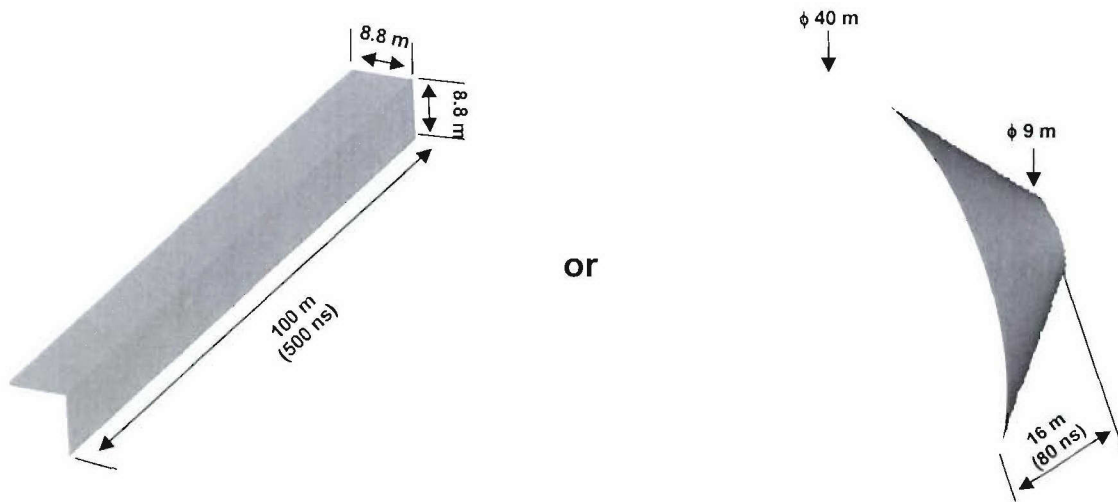
Figure 25. Possible configurations to accommodate the 8000 m³ Marx volume.

This assessment of the scale of the prime power driver shows that the present state of the art could be used but a very large system would result. Improvements in Marx driver technology (spark gap switches, capacitors, and stage configurations) could produce drivers with a figure of merit about half of the 27 m² per MV, MJ with consequent reduction in the size of the prime power for any such modules. This shall be the focus of any component development activity.

Additionally, considerations of buswork which might provide interconnection of Marxes to the front end show that simple arrangements rapidly exceed the allowed inductance budget due to convergence at the front end input terminals or the length (despite parallelism) needed to manifold a large number of Marx generators. Figures 26 and 27 provide sketches of two options that were considered for the Point Design. Neither of these options can meet the inductance and therefore, current requirements. This connection problem is unresolved in this Point Design and would have to be overcome before pursuing this approach.
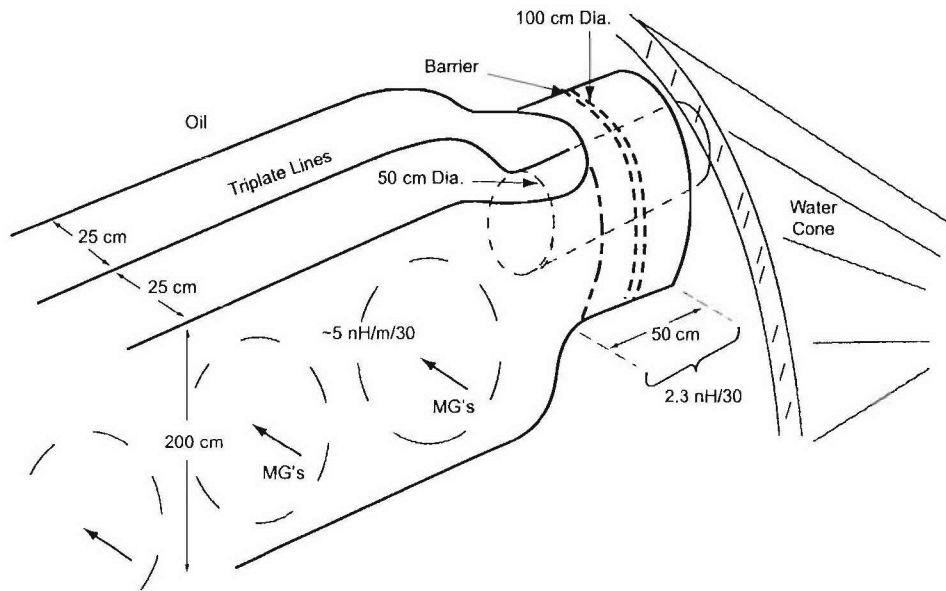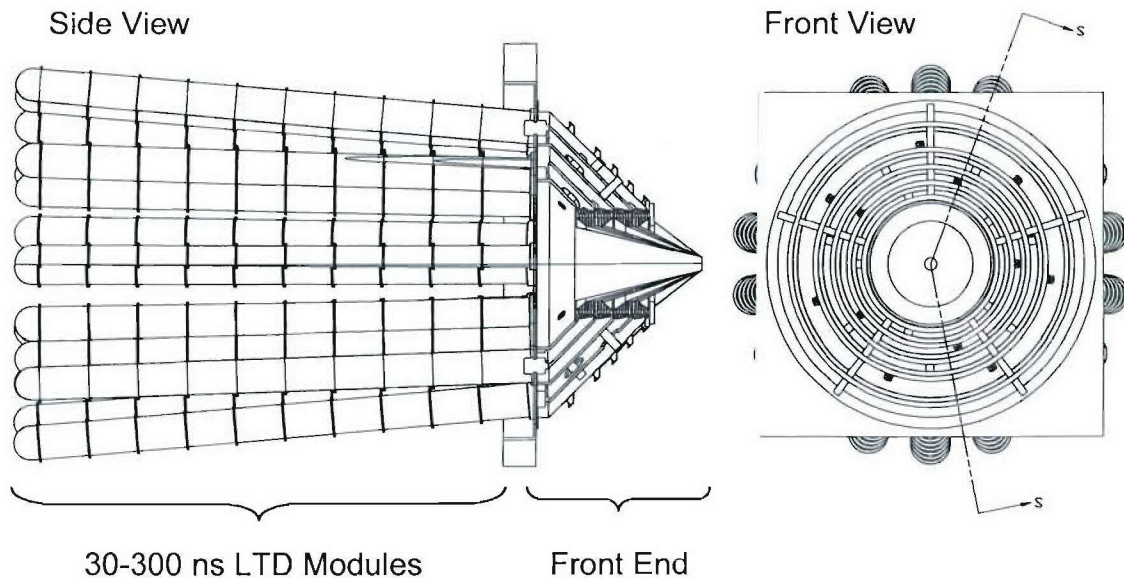
Figure 26. Marx driver buswork to front end triplate to coax – 30 terminals.
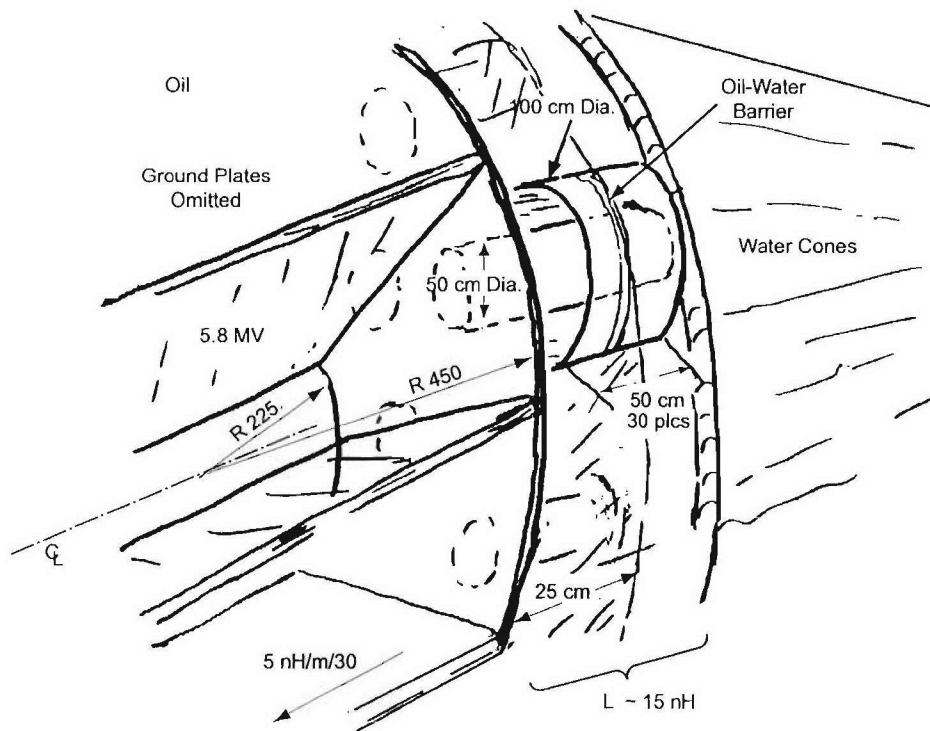
Figure 27. Marx driver buswork to front end: radial plates to disc to coax – 30 terminals.
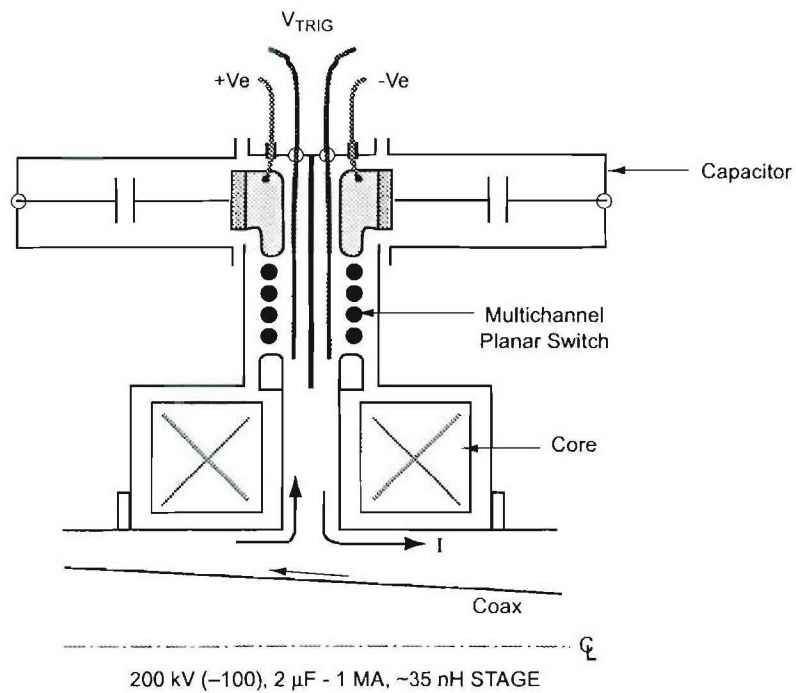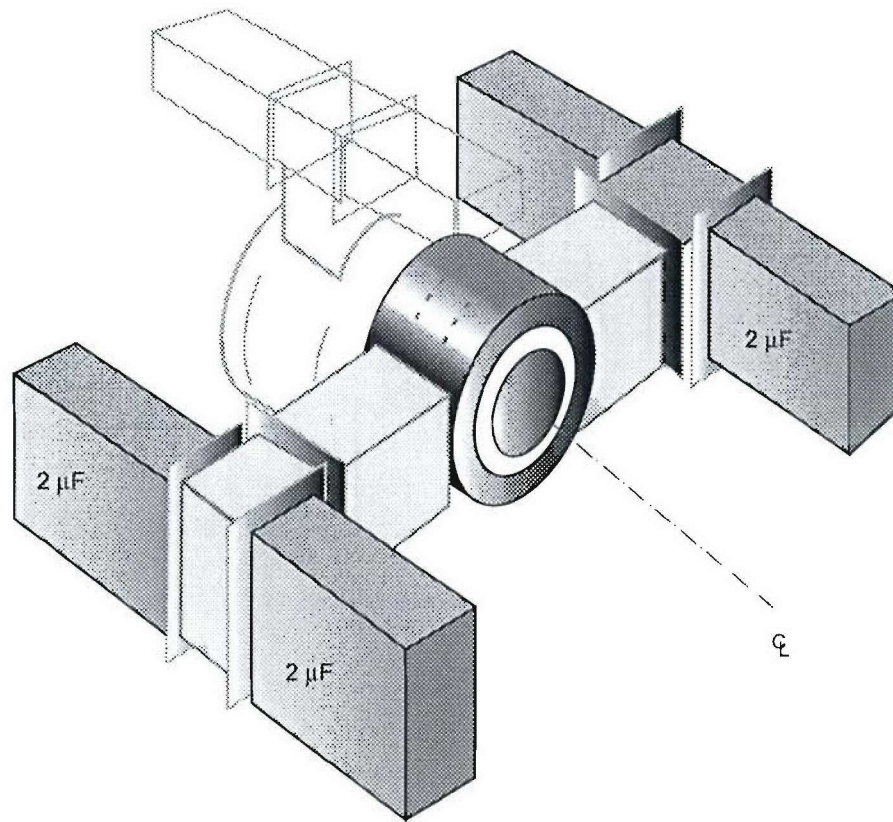
38

Analysis of this Point Design showed that while the low impedance conical front end was feasible, driving it directly by a relatively slow ($\sqrt{LC}$ = 300 ns) Marx array was inefficient and moreover overly complex and probably beyond the state of the art. This approach was therefore abandoned in favor of others using fast LTDs or based on development of faster, more compact Marx drivers, perhaps in combination with water transfer or peaking lines to be discussed later.

Direct Drive by a LTD. The Marx driven Schlitt line is complicated by the difficulty of achieving a low inductance connection to the line input terminals. The coaxial configuration of an LTD facilitates a matched impedance connection to the 250 ns Point Design front end. The front-end Point Design shown in Figure 20 has 30 coaxial input terminals connecting to the water cones. These provide for a straightforward multi-parallel connection of the coaxial output terminals of 30 LTDs as shown in Figure 28. A conceptual LTD stage was produced for this Point Design and has $\sqrt{L \bullet C}$ = 300 ns at 5.8 MV. Capacitors are based on existing high-energy designs and the switches derive from Russian multichannel-multigap designs. Figure 29 sketches the design concept for LTD stages, using the capacitor case as part of the cavity conductor. The attachments and component layout permit easy exchange of capacitors or switch replacement. The coaxial transmission line is oil insulated. The capacitor orientation was chosen to permit least distance separation of LTD centerlines and by clocking successive stages 90° they better utilize available volume. However, this Point Design is limited by peak capacitor and switch current to 1 MA per LTD or 30 MA in a module. Higher drive current could result from more LTDs in parallel connected to a larger front end interface further from the source. As PRS modeling improved, the need for higher current (~37 MA) was recognized. LTD module current higher than 1 MA was not deemed reasonable, and because accommodating more modules required increasing front end length, and therefore electrical pulse transit time to considerably more than the 75 ns required for current pulse waveshaping, this point design was abandoned.

Figure 28. LTD coupling to 100 kJ/250 ns water cones and front end.

39

2 μF

2 μF

2 μF

C̶L

V_TRIG

+Ve   -Ve

⊖   Capacitor

Multichannel
Planar Switch

Core

I

Coax

C̶L

200 kV (−100), 2 μF - 1 MA, ~35 nH STAGE

Figure 29. Conceptual 1 MA LTD stage for 30 MA, $\sqrt{LC}$ = 300 ns LTD driver system.

MGD with Water Pulse Compression. The front end design shown in Figure 20 and used as a basis for the previous Point Designs is a logical and feasible means of achieving the four 100 kJ yield modular configuration if a compatible driver can be identified. Drivers previously considered were too large to mate with this front end. This limitation can be alleviated by interposing a transfer capacitor or peaking capacitor stage, permitting more volume for the MGD at a larger radius from the load and achieving higher power and therefore smaller volume at the front end interface. To evaluate this possibility an assessment of a Point Design using a Water Capacitor Transfer stage was first performed. The Transfer Capacitor Point Design was based on the direct drive Point Design, modified as follows:

- Incorporate the $\sqrt{L \bullet C}$ = 300 ns Marx stage designed for the Direct drive case as the primary energy store
- Use 35 one-meter diameter, switched, water coax transfer capacitors with their length limited to 100 ns so that their output pulse width would be shorter than the implosion time
- Based on the system analysis presented in Section 3.1, target $\sqrt{L \bullet C}$ = 150 ns at the output of the transfer capacitors
- Connect the 35 transfer capacitors to the water cone ports shown in Figure 20
- Reduce front-end, vacuum inductance from 22 nH to 15 nH based on a lower inductance for the gas puff load and more aggressive magnetic insulation criteria
- Target load currents of 37 MA.

To achieve the required 37 MA load current, the equivalent circuit of the transfer capacitor driver for the front end must look like; 1.5 μF and 15 nH (15 nH is based on a feasible ≤ 500 nH per transfer capacitor output gas switch) at a 6.2 MV charge voltage. With the transfer capacitor electrical length limited to 100 ns for efficiency, their total capacitance is only 1 μF if the system is to be kept matched to the water cones at 0.1 Ω. While more could be added in parallel this would necessitate extending the front end water cones back to produce a larger interface area for the larger number of transfer capacitors and the water cone pulse transit time of ~75 ns would become excessive (≈105 ns). This approach was also abandoned.
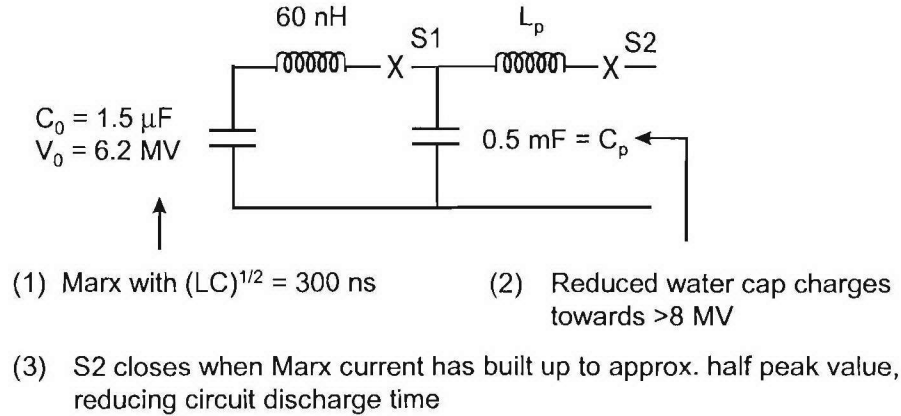
MGD With Water Peaking Capacitor. The reduced transfer capacitance possible in the previous Point Design suggested the possibility of a peaking capacitor configuration where a smaller capacitor is resonantly charged by the Marx driver and switched out earlier than in a matched transfer capacitor scheme.

An assessment of a Water "Peaking" Capacitor Point Design was performed. A simplified peaking-style circuit is shown in Figure 30. As in the previous assessment, we coupled this driver to the front end shown in Figure 20 with the vacuum inductance reduced to 15 nH. We targeted 37 MA for the load current and looked at sensitivity to:

- Peaker length
- C_o
- C_p

- L_p
- Voltage closure set-point for S2.

As part of the assessment, we also looked at peaker stress.

$$60 \text{ nH} \qquad L_p$$

(1) Marx with $(LC)^{1/2} = 300$ ns

(2) Reduced water cap charges towards >8 MV

(3) S2 closes when Marx current has built up to approx. half peak value, reducing circuit discharge time

Figure 30. Simplified circuit for Peaking Capacitor Point Design, indicating operation of S2 to reduce discharge time from 300 ns to 150 ns.

Results of running the circuit model of Figure 30 are shown in Figure 31. This Point Design achieves 37 MA, 250 ns load current with a peaking capacitor characterized by $C_p = 0.5$ µF and $\sqrt{L \cdot C}$ as long as 100 ns (L_p as much as 20 nH) using the same Marx parameters as before, 6.2 MV, 1.5 µF, 60 nH. We found only a weak dependence of current on peaker length, C_o, and L_p. S2 typically needs to close at 5-5.5 MV, which results in 190 ns peaking capacitor charge, for an 86 ns t_{eff} (63%). From Figure 31, it can be seen that tube voltage is only 4.2 MV because the peaking circuit can produce a more level tube voltage with our selection of 15 nH for the vacuum inductance. (Note: the peaking capacitor wave impedance is 7 Ω/35 = 0.2 Ω net, ~ impedance of water cones. This suggests the system is operating more like a pulse-sharpening section (plus re-reflection contribution) than a peaking circuit.)

The water peaking capacitor based Point Design appears to be feasible for the 100 kJ/250 ns case. The 35 water peaking capacitor diameters conveniently fit the input terminals of the front end water cones. The use of water eliminates the need for an oil-water barrier at that point. With a water peaker length of 100 ns (~3 m) the Marx driver interface is now located further from the source and approximately four times the area is available, as shown in Figure 32, and affords greater flexibility in connections. Mating Marx generator modules to two rings of water cones will be complex and depend upon the Marx configuration developed for the $\sqrt{LC}_{MG} = 300$ ns requirement. Variants of the schemes conceptualized for the monolithic designs discussed later have application here.
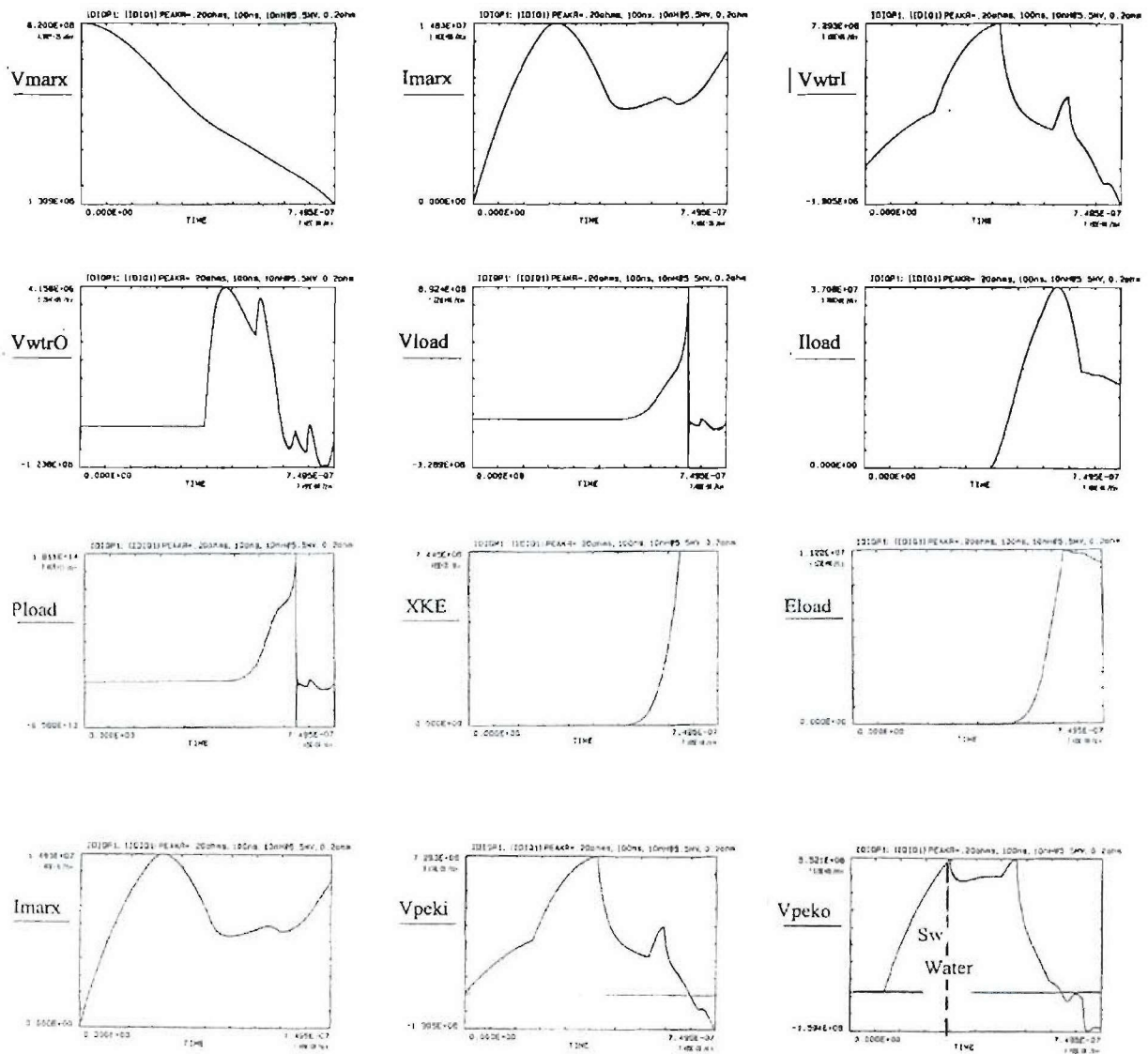
Figure 31. Waveforms using 1.5 µF, 6.2 MV, 60 nH Marx with 0.5 µF Peaker (35 each, 100 ns, 7 ohms) switched out at 5.5 MV through 10 nH.
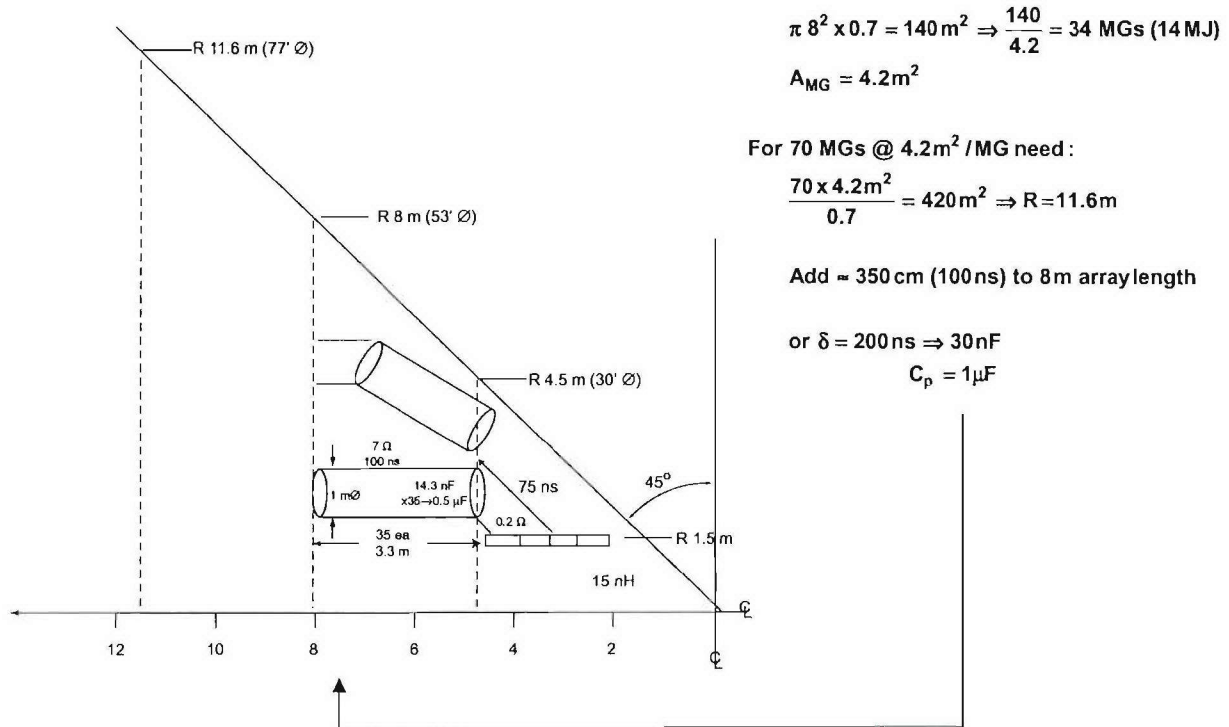
Figure 32. Sketch indicating how peaking capacitors can be connected to the front end shown in Figure 20.

$\sqrt{L \cdot C} = 175$ **ns Point Designs.** The previous Point Designs caused us to evaluate the interplay of electrical parameter values and consequent size and packaging of components. The $\sqrt{L \cdot C} = 300$ ns Marx driver was chosen as a feasible adaptation of present technology. Except in the peaking capacitor Point Design, the $\sqrt{L \cdot C} = 300$ ns stage driver point designs suffered from the common problem of not having sufficient real estate to connect the primary storage to the front end shown in Figure 20.

By considering the possible results of further component and configuration development, we developed concepts that appear capable of lowering intrinsic capacitor-switch stage $\sqrt{L \cdot C}$ to 175 ns with low-risk extensions of existing technology. The details of the concepts for the faster stage designs are presented in Section 6. We now present the revised Point Designs that result from using this improved driver technology.
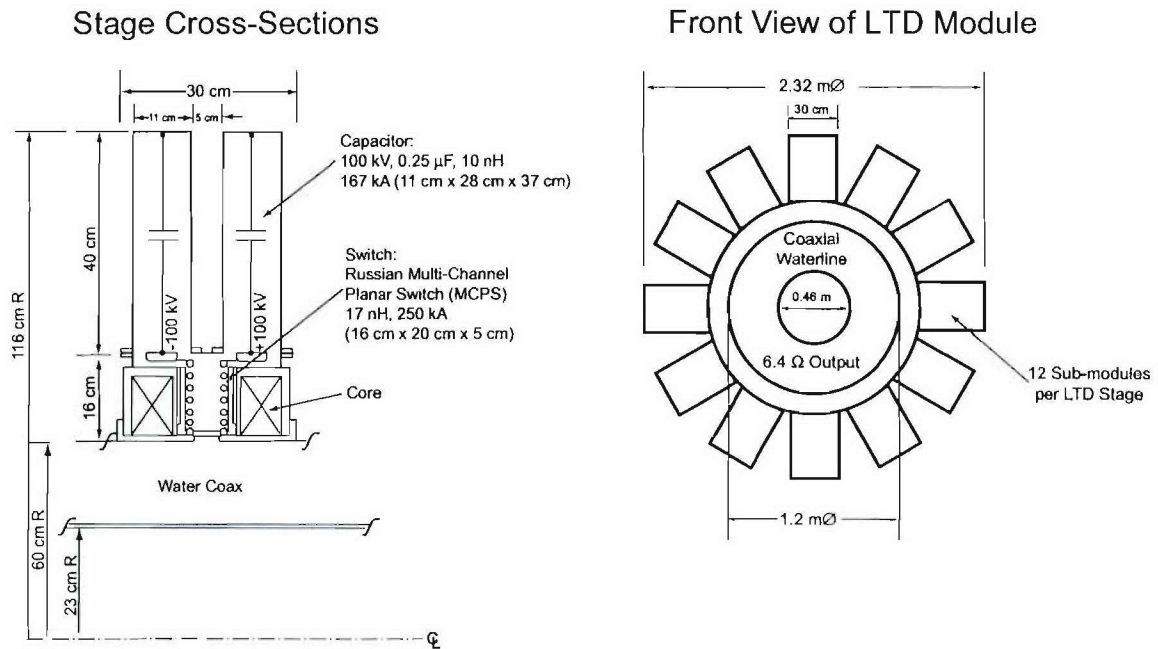
Direct Drive with Ultra-Fast Marx Generator Driver. The ultra-fast MGDs based on component and configuration development will have smaller projected terminal area and will tolerate a moderate increase in connection inductance with the result that the MGD to front end interface can be reduced from that required for the fast MGD. Figure 33 shows the relative difference for fast MGDs considered in previous ($\sqrt{L \cdot C} = 300$ ns) Point Designs and the faster MGDs discussed later.
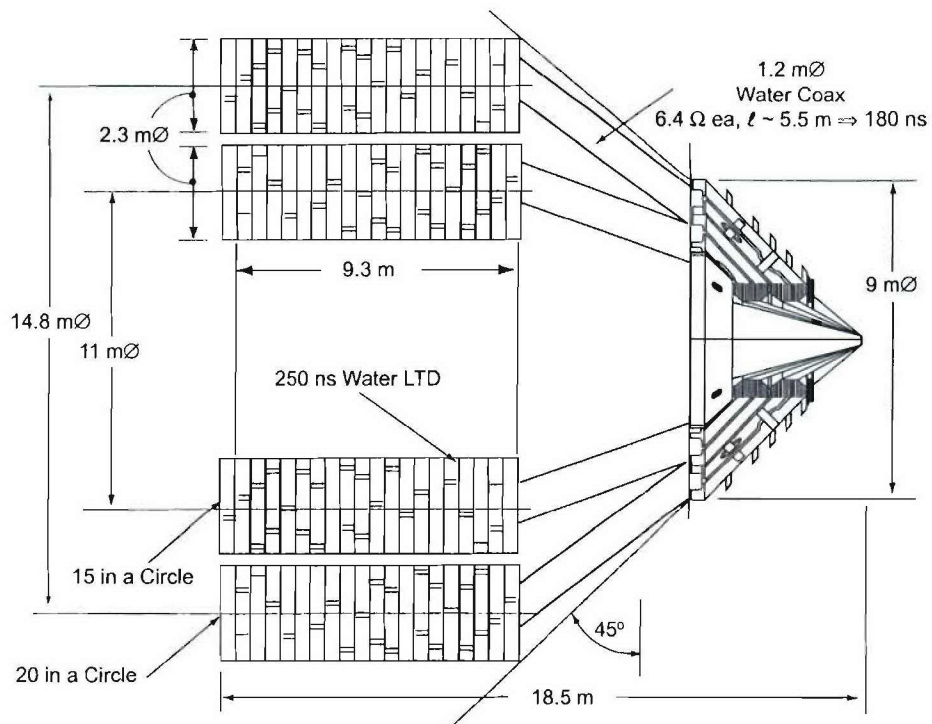
44
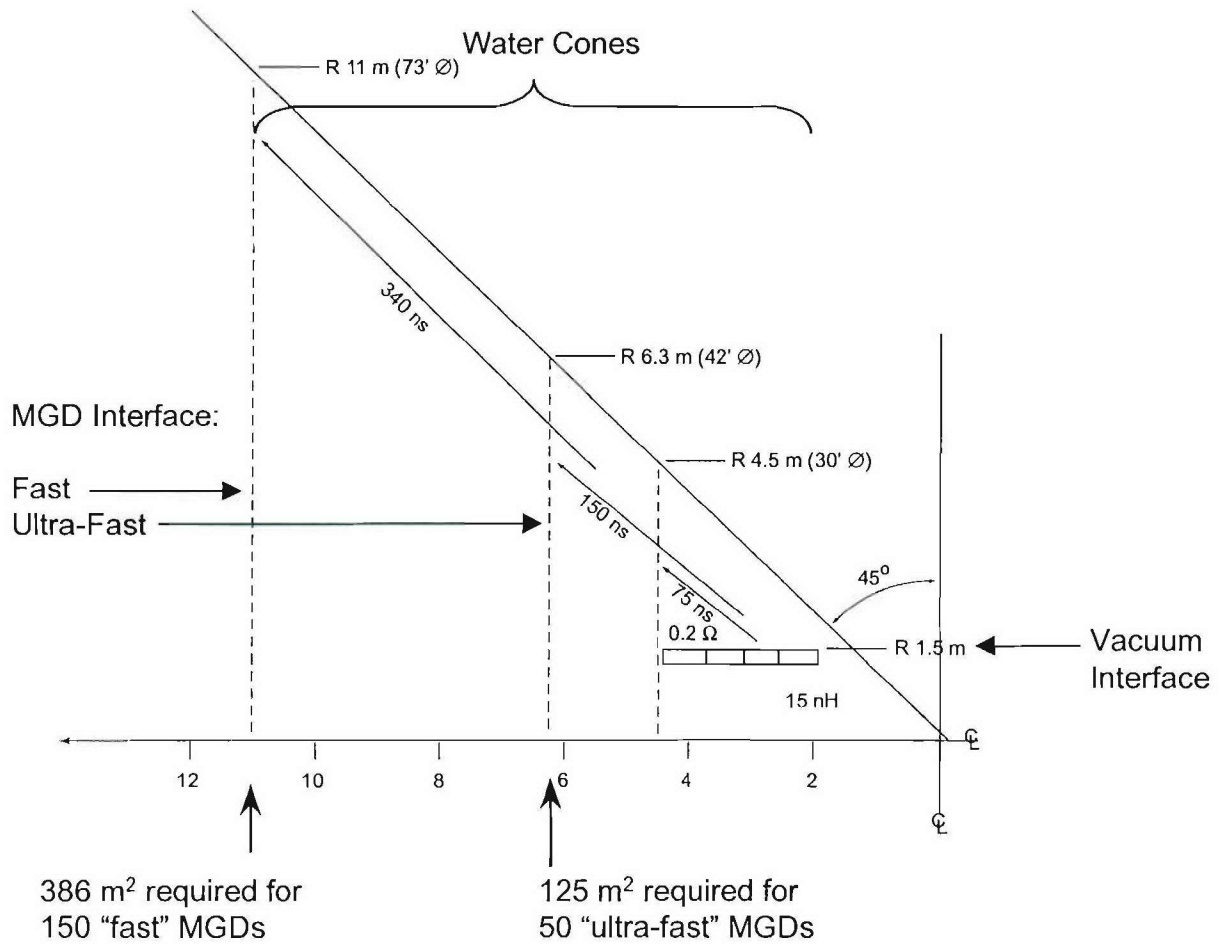
Figure 33. This sketch indicates the improvement that can be realized by reducing the $\sqrt{L \cdot C}$ of the Marx Generator driver from 300 ns ("fast") to 175 ns ("ultra-fast"). With the ultra-fast MGDs, less connection cross section area is required at the interface to the front end water cones.

Ultra-Fast LTD. Point designs for water insulated and oil insulated LTD's with $\sqrt{L \cdot C} = 175$ ns were considered for the modular 250 ns driver using components which are adaptations of present high energy storage capacitors and low inductance multichannel switches. The water-insulated fast LTD concept is shown in Figure 34. This LTD arrangement can be fit within the projected conical volume of the module by using matching coaxial water lines to connect a nested array of 35 LTDs to the front end water cones as shown in Figure 35. The performance of the scheme shown is consistent with scan predictions for a $\sqrt{LC} = 175$ ns driver, $\approx 0.2 \ \Omega$ transmission, and 15 nH vacuum inductance.

Stage Cross-Sections

Capacitor:
100 kV, 0.25 µF, 10 nH
167 kA (11 cm x 28 cm x 37 cm)

Switch:
Russian Multi-Channel
Planar Switch (MCPS)
17 nH, 250 kA
(16 cm x 20 cm x 5 cm)

Core

Water Coax

Front View of LTD Module

2.32 mØ

30 cm

Coaxial
Waterline

0.46 m

6.4 Ω Output

1.2 mØ

12 Sub-modules
per LTD Stage

Figure 34. 200 kV/Stage, $\sqrt{L \bullet C}$ = 175 ns, water-insulated LTD concept.

1.2 mØ
Water Coax
6.4 Ω ea, ℓ ~ 5.5 m ⟹ 180 ns

2.3 mØ

9.3 m

9 mØ

14.8 mØ

11 mØ

250 ns Water LTD

15 in a Circle

20 in a Circle

45°

18.5 m

Figure 35. Scheme for connecting 35 of the fast LTD's to the front end of the 100 kJ/250 ns source.

### 3.2.2 400 kJ/250 ns Monolithic Point Designs.

The concepts developed for the monolithic Point Designs are not as detailed as the modular Point Designs. We have depended on the System Analysis to set the specifications for the components (energy store, transmission line, and front-end coupler), and using the experience gained in our modular studies, sketched Point Designs with components consistent with the specifications. As indicated in Figure 36, all 400 kJ/250 ns Point Designs use cylindrically symmetric architecture. Because access to the full 2π angle allows for more parallelism, we have selected a front-end inductance of 8 nH in our Point Designs. The starting point for determining the structural configuration associated with each design involved rotating our modular designs around the full circle. For each design we have produced a simple sketch indicating sizes, impedances, and component counts associated with the Point Design. No detailed discussion is presented because such a detailed discussion would simply reproduce the parallel discussions for the associated modular design.
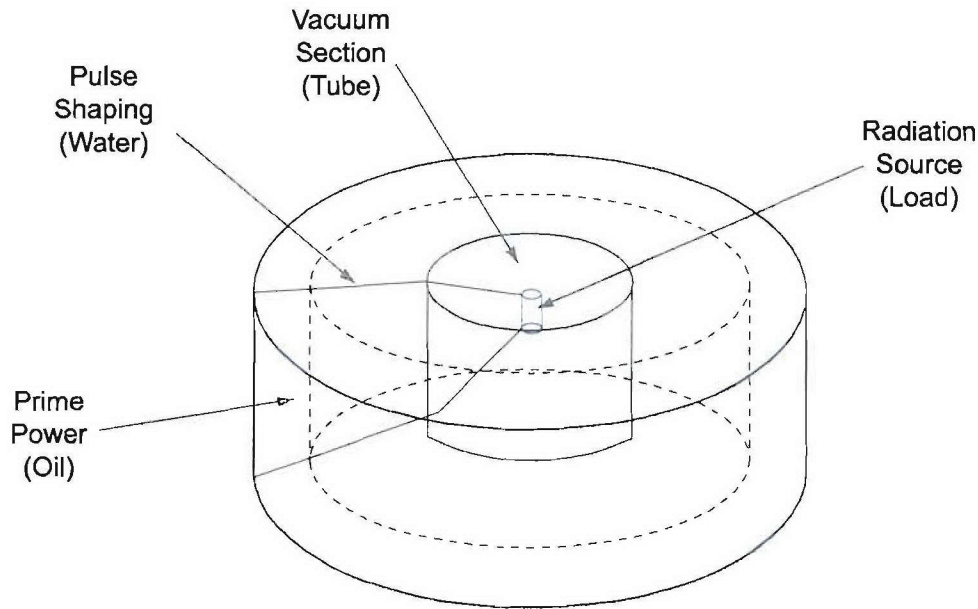
**Figure 36.** Generic layout for all 400 kJ Monolithic Point Designs.

Slow (State-of-the-Art) MGD-Transfer Capacitor. A sketch of the component layout for the slow MGD-Transfer Capacitor point design is shown in Figure 37. The dimension are as shown. The energy stored is 72 MJ in 60 slow MGD's arranged in 15 columns of 4 MGD's distributed around the circumference. Each MGD consists of eighty 3 μF-100 kV capacitors with an intrinsic stage $\sqrt{L \bullet C} \sim 500$ ns. These stages are essentially existing state-of-the art and no further details of their design will be presented. Two transfer capacitors are connected to each MGD for a total of 120. Each transfer capacitor is characterized by 100 ns, 4.5 Ω, and a switch-out voltage of 6.6 MV. This design is roughly equivalent to the Z-upgrade SNL is studying with the difference that the implosions time is 250 ns versus their target of 125 ns.
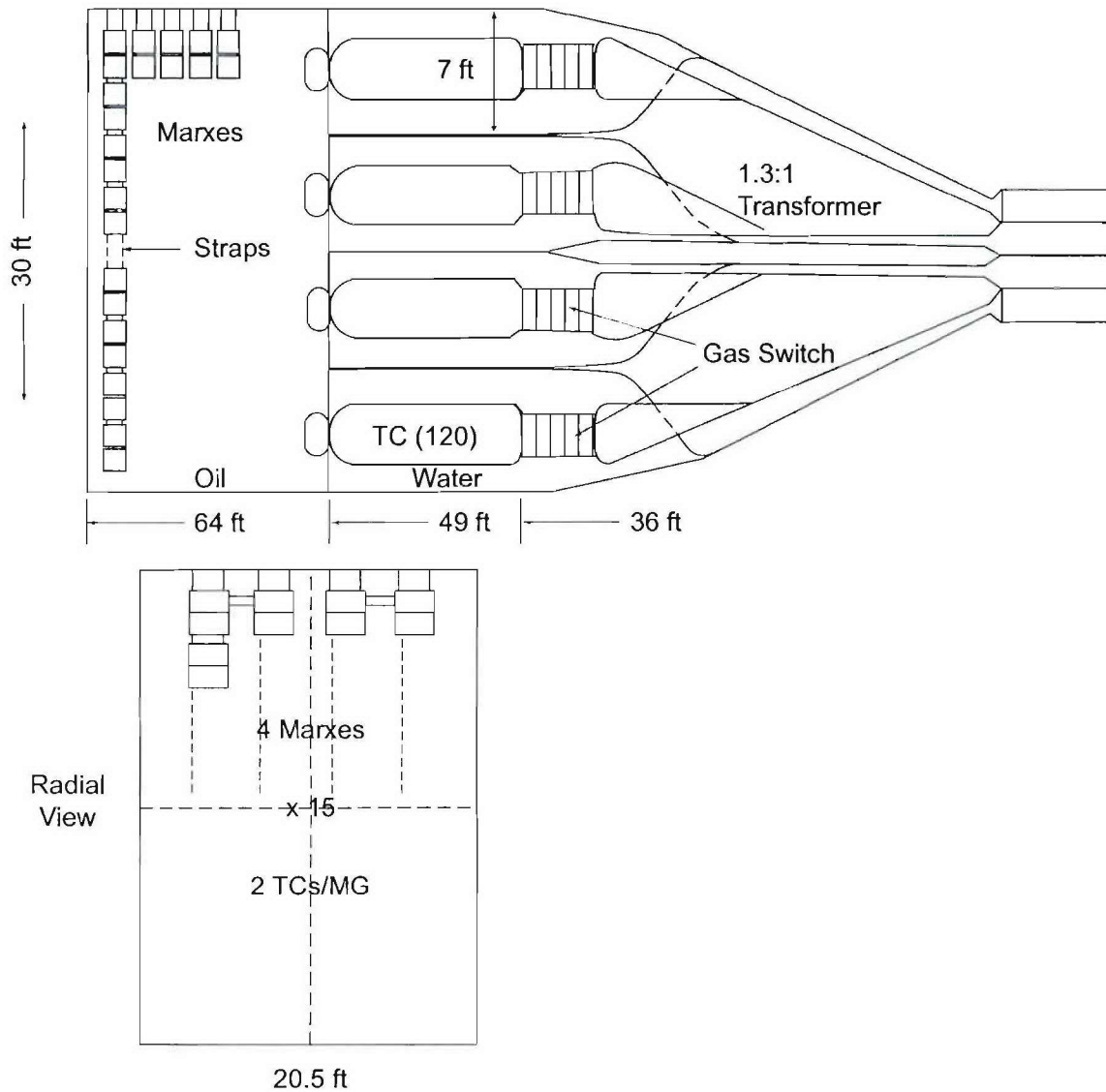
Figure 37. Slow MGD-Transfer Capacitor Point Design component layout.

Fast MGD-Peaking Capacitor. A sketch of the component layout for a $\sqrt{L \bullet C}$ = 300 ns – peaking capacitor point design is shown in Figure 38. The dimension are as shown. The energy stored is 56 MJ in 96 fast MGD's. Each MGD has 48 stages with an 8.6 MV open circuit voltage and delivers 150 kV. More details of the fast MGD stages are presented in Section 6.
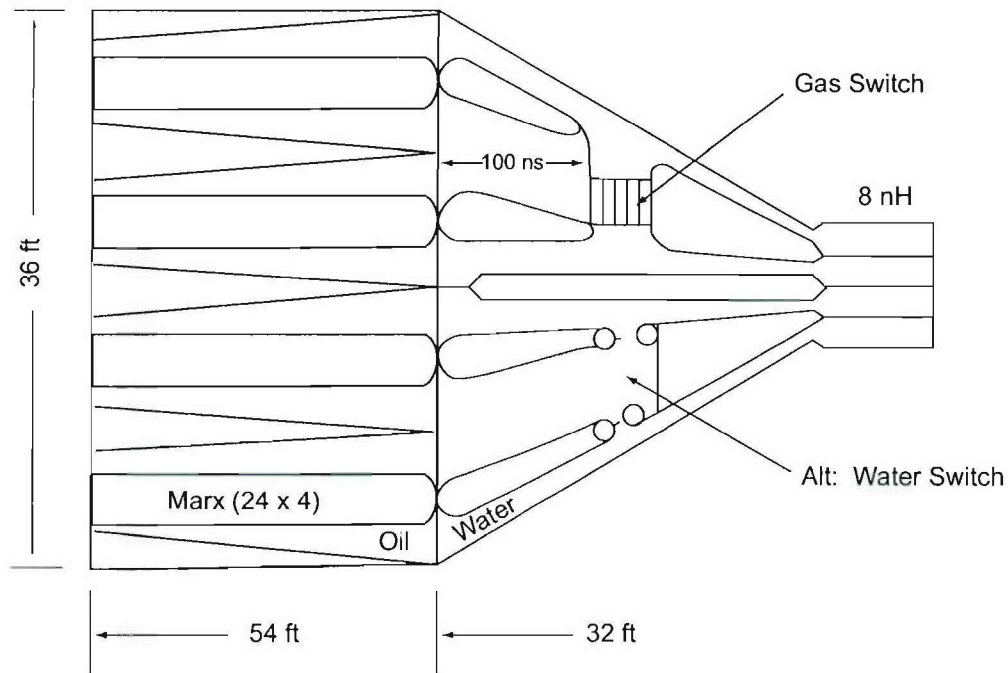
Figure 38. Fast MGD-Peaking Capacitor Point Design component layout.

Ultra-Fast MGD Direct Drive. A sketch of the component layout for the direct drive point design is shown in Figure 39. The dimensions are as shown. The energy stored is 66.8 MJ in 256 ultra-fast MGD's ($\sqrt{L \cdot C}$ = 175 ns). Each MGD has 87 stages with an 8.7 MV open circuit voltage and delivers 258 kJ. More details of the ultra-fast MGD stages are presented in Section 6.
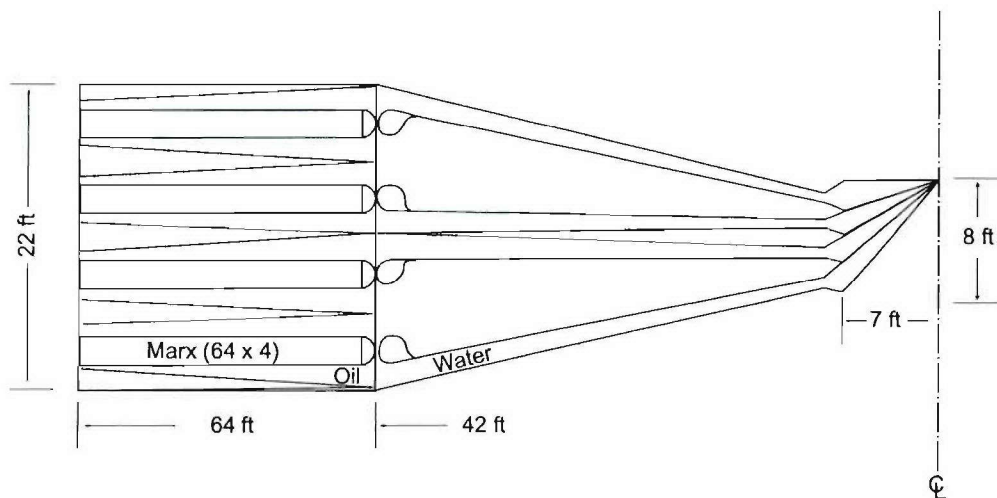
Figure 39. Direct Drive Point Design component layout.

SECTION 4
RADIATION SOURCES

Radiation source issues investigated during this system study involved:

- Selection of a model to predict krypton k-shell yield
- Choice of multiple modular sources or single monolithic source.

In this section we present discussions of both issues.

4.1 MQK MODEL FOR PREDICTING KRYPTON K-SHELL YIELD.

Because there is no experimental database for Krypton k-line yield versus current waveform, a model must be employed to predict the current waveform the driver must deliver to the PRS source. A simple O-D model for PRS line yield was put forth by Mosher, Qi, and Krishnan[2]. Subsequently, Mosher developed the following prescription and the supporting program in Table 13 to automate calculations for this study.

Table 13. Subroutine KRYIELD (m,Rf,Kt,Ym).

```
      real*4 m,K,Kt,Ni
      Z=36.                          !Krypton
      hv=10.2*Z**2                   !eV K-line energy
      Ni=3.8e23*m/Z**1.1             !ions/cm line density
      K=Kt*0.25                      !J/cm available
      CEi=4.7e-19*Z**0.82*Ni         !J/cm-eV
      CY=2.7e-31*Z*Ni**2/rf          !J-eV/cm
      T0=K/Cei                       !eV temperature for Y=0
      T1=0.                          !eV lower limit
      T=0.75*T0                      !eV 1st iteration
      do 6 it=1,25                   !iterate temperature
      Ei=CEi*T                       !J/cm internal energy
      dif=K-Ei                       !J/cm
      Yt=CY*exp(-hv/T)/T             !J/cm thin yield
      S=1.                           !escape fraction
      Y=S*Yt                         !J/cm radiated
      if(abs(Y-dif).le..01*Y) go to 3  !energy balance ok
      if(Y.gt.dif) go to 4           !too much radiation
      if(Y.lt.dif) go to 5           !too little radiation
    4 T0=T
      T=0.5*(T+T1)
      go to 6
    5 T1=T
      T=0.5*(T+T0)
    6 continue
    3 Ym=Y                           !J/cm radiated 2-level
      return
      end
```

Mosher's Prescription for NGM Krypton-Load-Performance Estimates
1/21/00

This process will perform a series of load-parameter scans covering variations in load length z_L(cm), and initial radius R_0(cm) for three implosion times t_{imp} = 100, 250, and 450 ns. As the initial radius is varied, the compression ratio to the final stagnation radius R_f(cm) remains fixed at R_0/R_f = 10, and the ratio of R_0 to the current-return radius R_W(cm) remains fixed at R_W/R_0 = 1.5. The initial load inductance/length will then be $2ln(R_W/R_0)$ = 0.81 nH/cm, and the final value at stagnation will be $2ln(R_W/R_f)$ = 5.4 nH/cm for all implosion histories. The objective is to determine the maximum yield for each implosion time and the corresponding optimum load parameters. The following procedure is an efficient means to accomplish this objective.

1. Select an implosion time and the corresponding circuit model.

2. Select a value for z_L .

3. Select a nominal value for R_0 that will be used to perform the implosion calculations in step 4 below. Nominal radius values of 2, 5, and 9 cm are physically reasonable choices for 100, 250, and 450 ns implosions, respectively.

4. For the selected nominal radius, iterate values of load mass/cm m(g/cm) and perform slug-model-implosion calculations until the selected implosion time is achieved. Implosion time is defined as the duration between the linear extrapolation of the current rise to zero and the time at which the 10:1 radial compression is achieved. Figure 40 below shows an example of implosion time determination for a simple Z-machine circuit model. Record the values of mR_0^2(gcm) and the implosion energy/length at stagnation K_t(J/cm) corresponding to the target implosion time. For slug-model implosions, K_t can be calculated from the final kinetic energy of implosion $mV_f^2/2$, where V_f is the implosion velocity at $r = R_f$, or from the work done on the plasma

$$K_t = \frac{1}{2} \int_0^{t_{imp}} I^2 \frac{dL}{dt} dt$$

where I(A) and L(H/cm) are the time-varying current and load inductance/length. The two energy calculations should give the same result for slug-model implosions. As t_{imp} and K_t depend only on the product mR_0^2 for fixed compression ratio, you will not need to run the circuit model again until z_L is changed in step 6.

5. For a given t_{imp} and z_L, the single computed values of mR_0^2 and K_t suffice to determine the optimum values of load mass m* and initial radius R_0* that maximize krypton K-shell yield. To perform the radius/mass scan, vary R_0 over a wide range (something like 1 to 20 cm) to capture the optimum. For each R_0, calculate a new load mass and new stagnation radius using $m = (mR_0^2)/R_0^2$ and $R_f = R_0/(R_0/R_f) = R_0/10$. Then, calculate the yield/cm Y_m(J/cm) for each R_0 by calling the attached fortran subroutine KRYIELD(m,Rf,Kt,Ym). This subroutine calculates Kr K-shell yield from a modified two-level model that has been benchmarked against titanium and stainless-steel wire-array experiments on Z and altered to account for additional high-atomic-number losses to softer x-rays. Extract the maximum

51

yield/cm $Y^*(z_L)$ and corresponding optimum radius and mass $R_0^*(z_L)$ and $m^*(z_L)$. The total maximum K-shell yield $Y_t(J)$ for the selected t_{imp} and z_L is given by $z_L Y^*(z_L)$.

PBFAZ Slug-Model Current
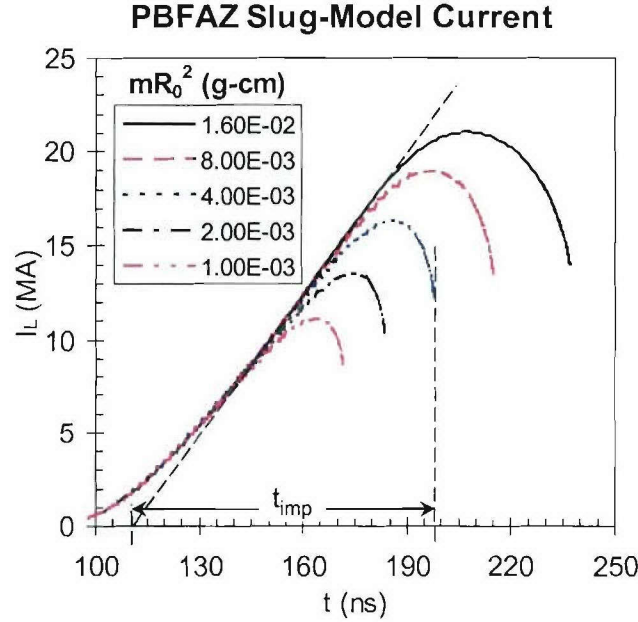
Figure 40. An example of implosion time determination for a simple Z-machine circuit model.

6. Go back to 2, iterate z_L., and repeat 3 - 5 as required to determine the optimum load length z_L^* and the largest total yield Y_t^*. The load-length-optimized values Y_t^*, z_L^*, $R_0^*(z_L^*)$ and $m^*(z_L^*)$ satisfy the objective for the selected implosion time.

7. Go back to 1 and repeat 2 - 6 for the other implosion times and appropriate circuit models.

This MQK model and process have been used in this study.

Based on the MQK model, Table 14 establishes the current requirements for different implosion times and for compression ratios of 10:1 and 15:1. The uncertainty in the calculations for this simple model is estimated to be a factor of 2.

52

Table 14. MQK model results for Kr K-shell yield.

Krypton K-shell uniform fill I-dot = constant. Conventional compression ratio 10 (τ = 100 ns)

	Y (kJ/cm)	K (MJ/cm)	%
20 MA	20	0.62	3.1
25 MA	46	0.96	4.8
30 MA	88	1.39	6.3
35 MA	148	1.89	7.8
40 MA	230	2.47	9.3
50 MA	470	3.86	12.2
60 MA	819	5.55	14.7

Argon at	30 MA,	540 kJ/cm,	1.39 MJ/cm,	38%
Titanium at	30 MA,	433 kJ/cm,	1.39 MJ/cm,	31%

Krypton K-shell uniform fill I-dot = constant. Conventional compression ratio 10 (τ =250 ns)

	Y (kJ/cm)	K (MJ/cm)	%
20 MA	9	0.62	1.46
25 MA	21	0.96	2.19
30 MA	42	1.39	3.02
35 MA	74	1.89	3.92
40 MA	120	2.47	4.86
50 MA	262	3.86	6.80
60 MA	485	5.55	8.74

Argon at	30 MA,	480 kJ/cm,	1.39 MJ/cm	35%
Titanium at	30 MA,	349 kJ,	1.39 MJ/cm	25%

Uniform Krypton fill I-dot = constant. Conventional compression ratio 15 (τ = 100 ns)

	Y (kJ/cm)	K (MJ/cm)	%
20 MA	40	0.73	5.58
25 MA	87	1.13	7.71
30 MA	160	1.63	9.79
35 MA	261	2.22	11.76
40 MA	394	2.90	13.59
50 MA	763	4.54	16.82
60 MA	1277	6.53	19.55

Uniform Krypton fill I-dot = constant. Conventional compression ratio 15 (τ = 250 ns)

	Y (kJ/cm)	K (MJ/cm)	%
20 MA	19	0.73	2.62
25 MA	43	1.13	3.84
30 MA	84	1.63	5.15
35 MA	144	2.22	6.49
40 MA	228	2.90	7.84
50 MA	474	4.54	10.44
60 MA	839	6.53	12.85

4.2   COMPARISON BETWEEN ONE PRS SOURCE AND FOUR DISTRIBUTED PRS SOURCES FOR PRODUCING 1.0 cal/cm^2 OVER 1.0 m^2.

4.2.1   Introduction.

When properly configured to match preset uniformity and area criteria distributed sources have the advantage of delivering a higher fluence area product than a single point source for the same total source strength. This higher fluence area product for the distributed source must be weighed against the disadvantages introduced by the distributed source over the single point source. If the distributed source is not uniform the degree to which the source distribution is not uniform will off set some of the fluence area product advantage of the distributed source. If the distributed source is composed of a set of individual point sources the comparison becomes even more complex. In this case the variation in the source distribution can be related to the shot-to-shot variability in the x-ray yield of the sources. The jitter in the turn-on time of the individual sources is an additional complication introduced by the distributed multiple source configuration.

Observations on existing PRS sources indicate that these sources have an asymmetric azimuthal emission pattern. As one observes the emission as a function of the angle to the axis of the line source, the apparent source strength is reduced when viewed along the axis compared with viewing the source perpendicular to the axis of the source. Hence, when exposing large area test objects this source emission characteristic must be considered when determining the source strength required to obtain a given fluence area product. This may or may not be important for a krypton PRS plasma.

The economics of making one large machine versus several smaller distributed machines must also consider source yield and cost scaling with the current required to generate the x-ray source.

4.2.2   Fluence Pattern on the Test Plane.

Single Point Source. Figure 41 illustrates a typical fluence pattern at 1.0 m from a point source with isotropic emission. The fluence is normalized to unity at the center of the pattern. This is a simple geometric projection which considers 1/R^2 from the source to the test plane and cosine of the angle between the normal to the test plane and the line of sight between the source point and the test point. If the uniformity is defined as the ratio of the minimum to the maximum fluence in the area, the area contained within a specified uniformity circle, e.g., 0.8, can only be adjusted by moving the test plane relative to the source. Once the test plane has been positioned to give a desired uniformity over a given area, the source strength must be adjusted to give the desired fluence over this area.

Figure 42 shows a set of measurements on the emission pattern made from an argon PRS source generated by BLACKJACK 5[3]. The error bars are the observed standard deviation in the relative fluence measured at the given angles relative to the fluence measured normal to the source axis for any given shot. The measurement at 22 degrees was the most difficult to make and could of had a systematic partial source obscuration. It is anticipated that each PRS source will have a similar asymmetry in the emission pattern but that each source will have its own characteristics. Even though the krypton PRS source could have a more symmetric emission

pattern than observed for argon, the observed pattern for the BLACKJACK 5 argon source will be used for most of the source analysis to be discussed. A simple analytical fit was made to the observed argon emission pattern and this fit is also shown in Figure 42.
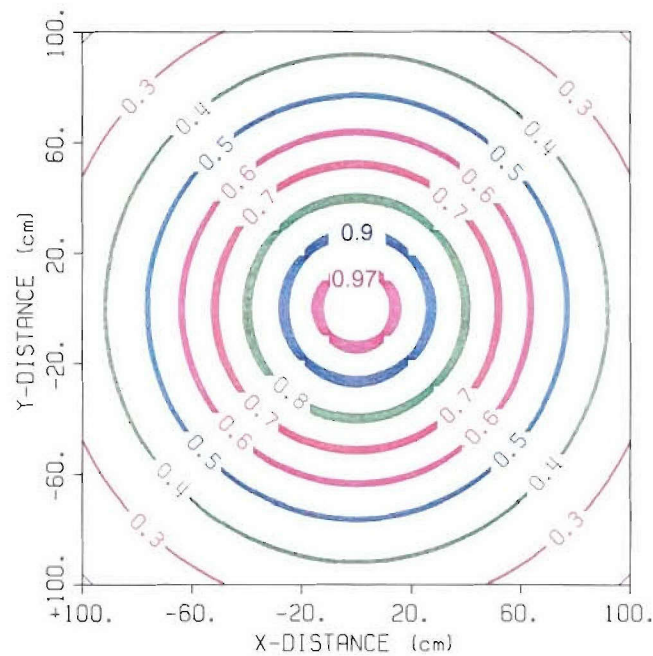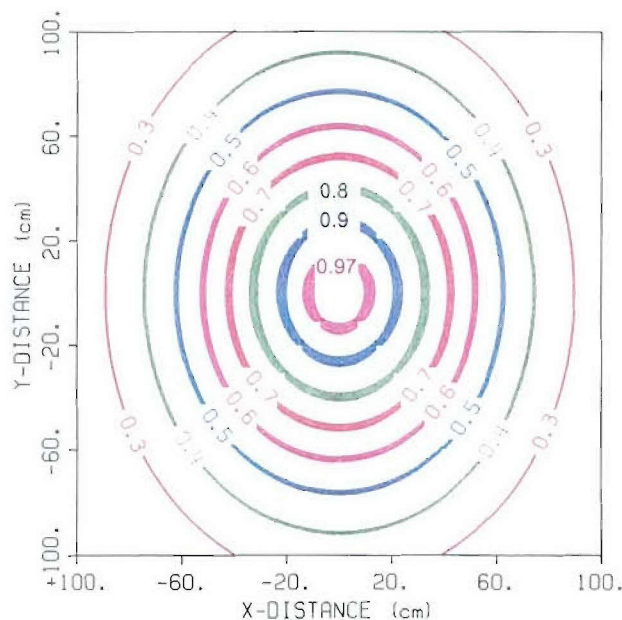

Figure 41. Isofluence lines 1.0 m from an isotropic point source.

$$Y = 0.53 + 0.47 \sin^3(\theta)$$
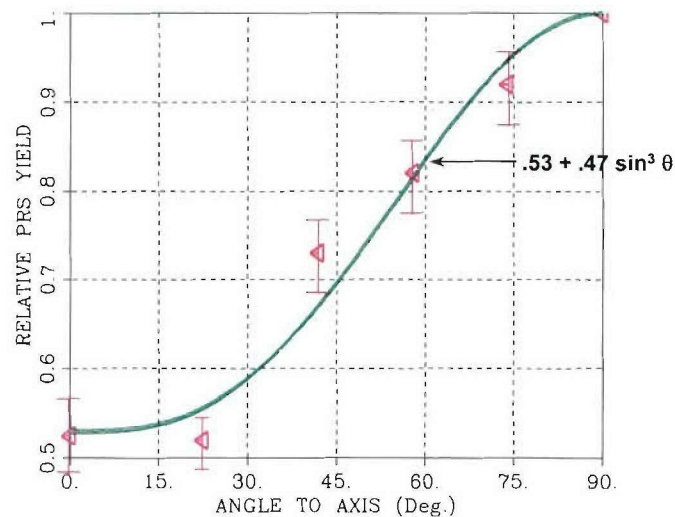
**Figure 42.** Measured variation in effective Argon K-yield with angle to axis from Blackjack 5.

55

The fluence pattern from a typical PRS point source at 1.0 m from the source is shown in Figure 43. In this case the axis of the source is aligned along the x-axis. Because of this reduction in the effective source strength with azimuth the source strength perpendicular to the source axis must be increased to obtain the same fluence area product as an isotropic source. As an example, the source strength requirements to obtain 1.0 cal/cm^2 over 1.0 m^2 for both an isotropic point and a typical PRS source are shown in Figure 44. For this particular example a factor of 1.22 more source energy is required for the PRS source than the isotropic source to obtain this fluence area product. This ratio of source energies is relatively insensitive to the desired uniformity over 1.0 m^2. This ratio is expected considering the emission pattern function and that the effective source strength dependence is one dimensional, i.e., it only depends on the azimuthal angle.


Figure 43. Isofluence lines 1.0 m from a typical PRS point source.

Four Point Sources. Under the best of conditions one might have four identical PRS sources. The fluence pattern for an optimum source spacing to give a 0.8 uniformity over an area of 1.0 m^2 is shown in Figure 45 for four identical PRS sources. In this case the two PRS sources along the x-axis are aligned to the x-axis and the two PRS sources along the y-axis are aligned to the y-axis which should be obvious from the fluence pattern. In this case the source-to-source distance was 66 cm and the distance to the test plane was 51 cm. The optimum source spacing and distance to the test plane depend on the source emission pattern, the desired uniformity, and the exposure area.
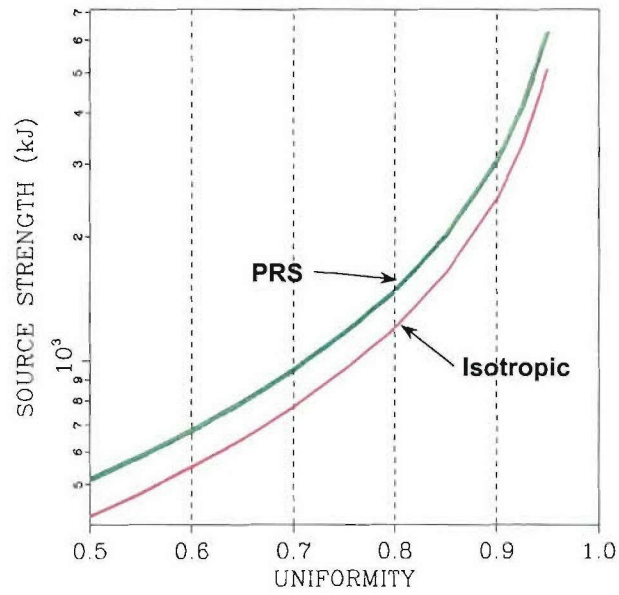
Figure 44. Comparison between isotropic and typical PRS source strength requirements to obtain 1.0 cal/cm^2 over 1.0 m^2.


SPG = 66 cm
Z = 51 cm
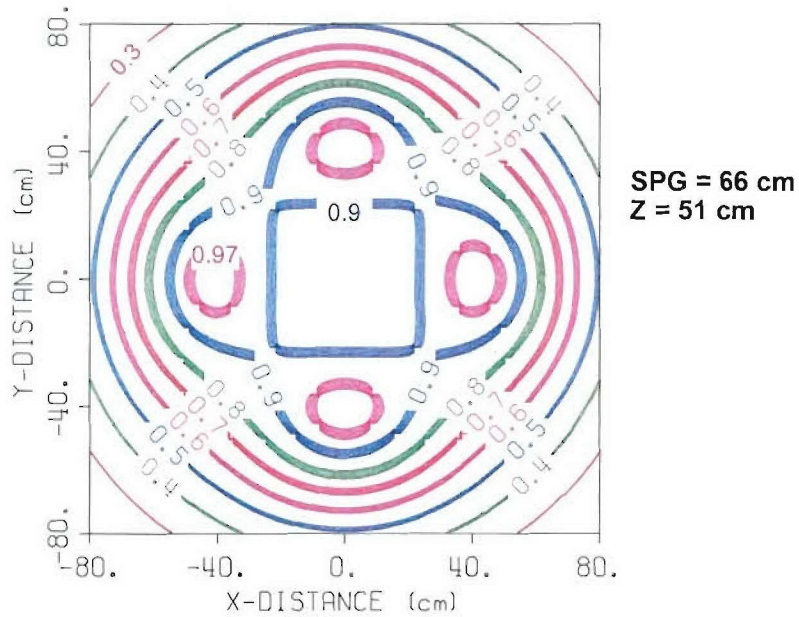
Figure 45. Four identical point PRS sources with source spacing and distance to test plane optimized to give a fluence uniformity of 0.8 over 1.0 m^2.

Real PRS sources have not proven to be truly repeatable. John Riordan states that under the best of conditions the PRS argon yield on DOUBLE EAGLE had a standard deviation of 7% over a consecutive sequence of 10 shots, in particular shots 4039 through 4048. If one selects a specific area, say 1.0 m^2, then the decrease in uniformity over that area can be estimated as a function of the source variability. This decrease in fluence uniformity is shown in Figure 46 for initial uniformities of 0.6 and 0.8. These numbers were determined by using a random number generator to select source strengths from a normal distribution with the given standard deviation. The process is repeated many times (>50) to obtain the mean uniformity and the standard deviation from the mean uniformity. Hence, one must consider the mean uniformity over the test area when discussing real PRS sources. Figure 47 shows a typical random fluence pattern from a set of four sources configured as in Figure 44 but with a 10% standard deviation in source strength. As in the case of the single point source, the source strength required to reach a given uniformity increases with the desired uniformity. This relationship is shown in Figure 48 for four PRS sources with a 10% standard deviation in source strength versus the mean uniformity under the constraint of producing 1.0 cal/cm^2 over 1.0 m^2.
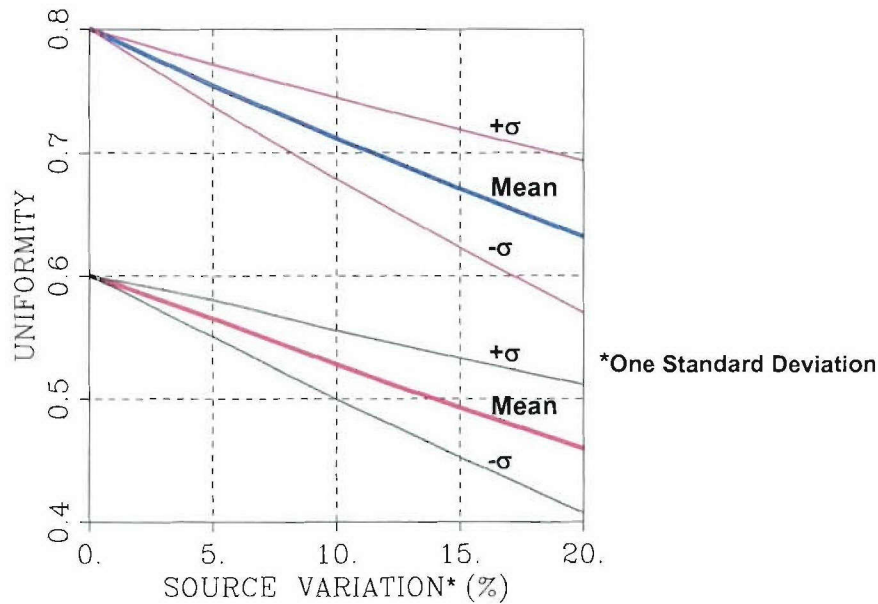
Figure 46. Degradation in fluence uniformity over a fixed exposure area from variations in the source strengths of the 4 PRS points.
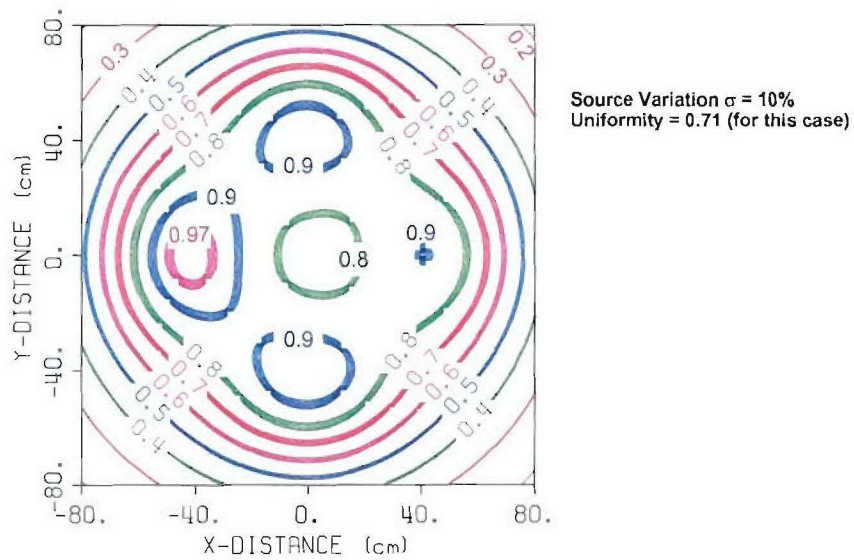
Figure 47. Typical fluence uniformity from real PRS point sources for area designed for 0.8 uniformity for identical sources.
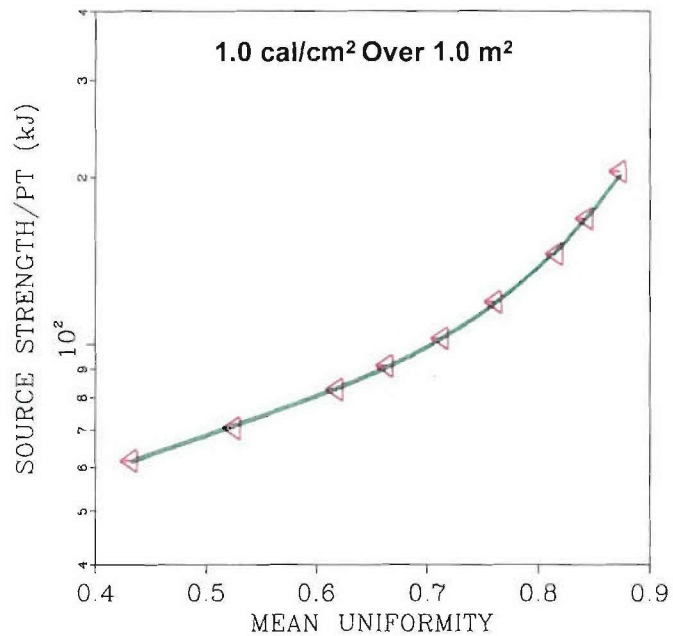

Figure 48. Source strength requirement for 4 optimized PRS points with a 10% standard deviation in source yield.

59

Comparison Between One Point Source and Four Distributed Sources. A basic geometrical difference must occur to increase the fluence area product with the distributed sources over a single point source. The test plane must move closer to the source plane for the distributed sources. A measure of this geometrical difference is the ratio of the effective exposure radius to the distance between the source and test planes, the aspect ratio. The dependence of aspect ratio on fluence uniformity is shown in Figure 49 for both a point source and for four optimized distributed sources for an exposure area of $1.0 \ m^2$. When one considers the variability in the source yields, the aspect ratio is reduced for the four distributed sources at a given uniformity. This aspect ratio has importance when designing debris shields. In any case it is doubtful that fast closing debris shields are compatible with these very large exposure areas and large aspect ratios. The most practical debris shield will probably be a layered system of low Z materials such that the final shield remains intact. The x-ray transmission of the debris shield, although designed to be minimal, may increase the source strength requirements and change the geometrical relationships between the source spacing and the test plane distance.

The ratio of the total source energy required for one point source to that required for four point sources to obtain the same fluence area product is the geometrical gain factor for the distributed source. This gain factor is shown in Figure 50 as a function of fluence uniformity for both four identical sources and four real sources. This gain factor increases as the desired uniformity increases. For a reasonable uniformity of 0.8 the gain factor is about 3.5 and 2.5 for four sources with zero and 10% standard deviations in source strength, respectively.
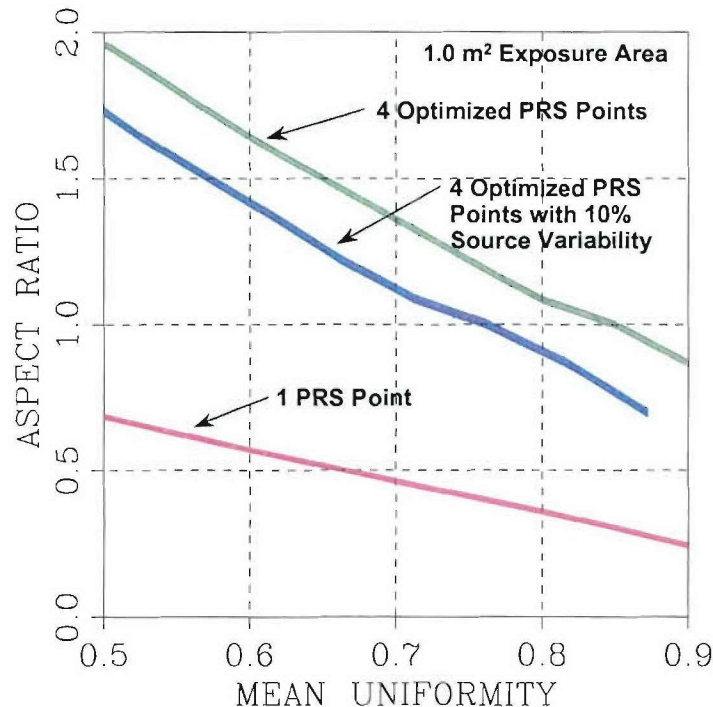
Figure 49. Ratio of the effective exposure radius to the source to test plane distance.
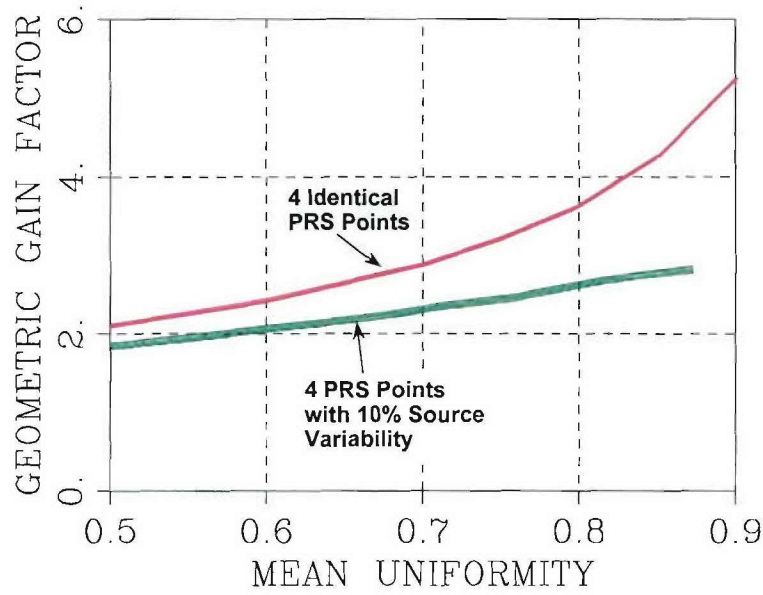
Figure 50. Ratio of the source strength required from one PRS point to the sum of the source strengths from four PRS points to obtain a fluence area product of 10^4 cal.

4.2.3 Cost Considerations.

Simple X-ray Yield Scaling With Current. The PRS K-yield typically scales as the current to a power between 2 to 4. The current to the 4th power scaling normally applies when the plasma conditions are not hot enough to effectively ionize the K shell electrons. The plasma normally becomes a strong K region emitter when the plasma has been heated to a temperature about ½ the K absorption edge energy of the plasma material. At this temperature the K-yield scales as the current squared. In general,

$$Y_{1-pt} = \alpha \left(I_{1-pt} \right)^{Py}$$

and

$$Y_{4-pt} = 4\alpha \left(I_{4-pt} \right)^{Py}.$$

For equivalent fluence area products the source yield for one point source must be the geometric gain factor times the total source yield from the 4 point sources. Hence,

$$Y_{1-pt} = F Y_{4-pt}$$

and the ratio of the currents becomes

$$\frac{I_{1-pt}}{I_{4-pt}} = (4F)^{1/Py} \quad .$$

If the value of Py is variable depending the x-ray yield, the value of Py will decrease as the yield increases. This, of course, favors making four distributed sources.

Simple Machine Cost Scaling With Current. The cost of making a PRS machine scales about as the current to the 2.5 power. Hence, if the scaling is not known precisely,

$$C_{1-pt} = k(I_{1-pt})^{Pc}$$

and

$$C_{4-pt} = 4k(I_{4-pt})^{Pc} \quad .$$

For an equivalent fluence area product

$$\frac{C_{1-pt}}{C_{4-pt}} = 1/4(4F)^{Pc/Py} \quad .$$

The breakeven cost between one point source versus four distributed point sources occurs when these two costs are equal or

$$Py = Pc*(1 + \ln(F)/\ln(4)) \quad .$$

In Figure 51 the current scaling for yield power, Py, is shown as function of the current scaling for cost power, Pc, at geometric gain factors of 2, 2.5 and 3. If the cost scaling current power is 2.5 as expected and the geometric gain factor is 2.5, the yield scaling current power must be greater than 4.2 before making a single point source machine becomes more cost effective than a distributed source with four points to arrive at the same fluence area product.
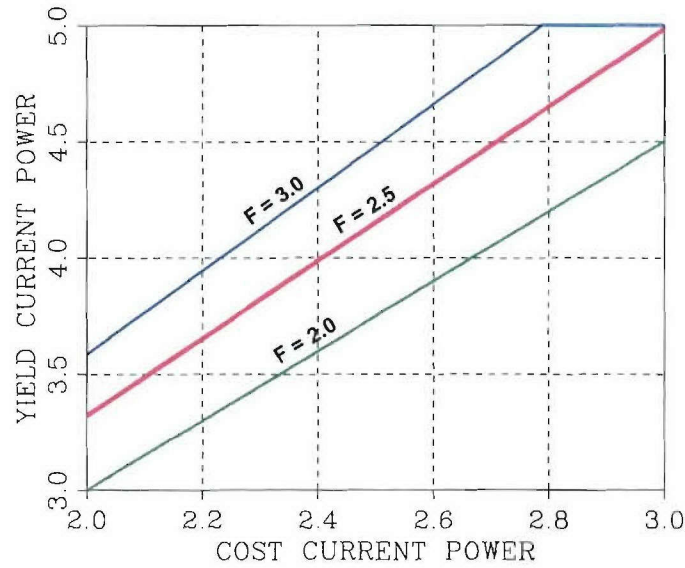
Figure 51. Cost break even lines between 1 PRS point versus 4 distributed PRS points for selected geometrical gain factors.

4.2.4 Source Timing Jitter.

There are other considerations besides the fluence area product which favor a single point PRS over a distributed four point PRS. As already mentioned the debris shield problem is exacerbated as the aspect ratio increases. However, the shine time for a krypton K source could be only of the order of one ns. If this is true, then most of the time the flux from each of the four distributed sources will arrive at separate times. Dave Kortbawi's experience with the DECADE modules and the DECADE QUAD indicate that the pulse power jitter from the four modules is 3-5 ns and that the jitter in the bremsstrahlung output from the four modules is 8-10 ns. The additional jitter between the pulse power and the bremsstrahlung output is thought to be caused by the POS. Hence, unless the technology is improved significantly the test object irradiated with the distributed PRS would receive four distinct flux pulses separated in time and space. The important question is whether this timing jitter affects the test object response. For mechanical induced response, a figure of merit is the transit time of the shock wave through some characteristic depth in the material. The e-fold penetration depth of an x ray in a specific material is the reciprocal of its linear x-ray cross section. If the depth for a relatively uniform dose is taken as 1/5 of this e-fold depth and the shock wave transit time is this characteristic depth divided by the longitudinal speed of sound, then the approximate time before source jitter affects the material response is given by

$$t_s = \frac{1}{5\mu_1 v_1} \quad .$$

The dependence of this maximum source shine time on photon energy is given for beryllium, fused silica, aluminum, and titanium in Figure 52. If the photon energy is equal to or greater

than 13 keV, low Z materials including fused silica and silicon carbide can probably be tested without the source jitter affecting the mechanical response. However, materials of higher atomic number cannot be tested without making the test results complicated by the source jitter.
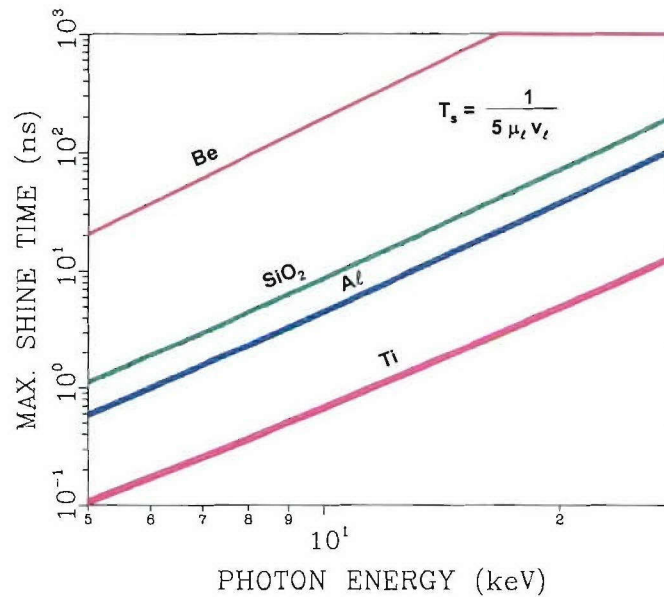
Figure 52. Approximate time before source jitter affects bulk material response.

4.2.5 Concluding Remarks.

If only the fluence area product delivered to the test object were important, then a distributed source would normally be more cost effective than a single PRS. However, there were several unknowns in this analysis which may invalidate the use of multiple distributed sources. First, we do not have a lot of data on the true shot-to-shot reproducibility of these sources, let alone the proposed krypton K source. Second, the source timing jitter from multiple sources will limit the test samples to relatively low Z materials. Third, the debris shield could become very difficult to implement for the very high aspect ratios needed for distributed sources.

4.2.6 Comments on K-Tech Assessment of Four Sources vs. One (I. Smith, PSI).

These comments address a briefing presented by K-Tech (Doug Reeder) on 13 January 2000.

The first section of the briefing is a comparison of the fluence and uniformity obtainable from four sources with those from one source that is four times as strong. The comparison is fairly straightforward; fluence and uniformity are not defined exactly and our attempts to deduce the definitions from the results give inconsistent answers, but the uncertainty is only 10 or 20%.

This section makes some clear points in favor of the four-source array, but does not bring them out. In particular, chart 5 shows that if 10 or 20% uniformity is needed then the dose area

product obtainable with four sources is 4.2 or 6.6 times as large, respectively, as with a single source. The advantage of four sources is also illustrated in chart 8, which shows (for 20% uniformity, for example) that four sources are superior to one source for exposure areas greater than 0.4 m^2, and much superior out to 2 m^2; this is the kind of area we were told was of interest. But the title of this chart is "Large Areas for Multisource Arrays Occur Only at Low Fluences." Of course, the magnitude of the fluence in the range in which the four-source array is superior to the single source depends on the spacing chosen for the four sources. K-Tech chose a 90 cm square array, and for this the fluence range for 20% uniformity is 0.8 cal/cm^2; for a 40 cm square, it would be 3.2 cal/cm^2, for example. The limit on how high the fluence could be in the optimum exposure region of four sources depends how close together you could place the sources. Whatever this fluence limit is, the single source could only obtain a quarter of it with the same area and uniformity, and could obtain the same fluence and uniformity over only a quarter of the area.

Incidentally, for 20% uniformity the 90 cm square array is shown to optimally irradiate a 20,800 cm^2 area in a plane 58 cm away. If the plane is moved back to 75 cm the fluence and fluence area product both drop by about a third (~1/r dependence). If the plane is moved in, the fluence area product falls as off a cliff, being down a factor of five at 50 cm (where the fluence at 20% uniformity is almost maximal). This must happen because at distances as small as 58 cm a 20% dip in intensity appears on axis compared with higher fluences out opposite the sources.

It may be that fluences of the order of a few cal/cm^2 are all too low to be of interest, and that to reach fluences that are of interest we need to make the sacrifice of the factor of 4.2 to 6.6 in area and some more beyond that, which takes us down in area so that only one source is practical to fit in. But this logical train of reasoning is not followed in the briefing.

Instead, the superiority of the single source is argued in a second section of the briefing that invokes current scaling, either I^2 or I^4. The charts in this section appear to underplay the difficulties of getting higher current and the fact that the energies required are going up more than linearly with I. Based on the first section of the briefing, the situation would more reasonably be stated as follows. To achieve with a single source the same fluence at 20% uniformity as an optimally-deployed four-source array, a single source must have a yield ~4.2 times that of the whole four-source array, or 17 times the yield of one of the array sources. Using I^4 scaling, the current must increase from 30 MA (K-Tech's example) to 61 MA. Using I^2 scaling requires 124 MA. The calculations we have seen using the radiation models suggest close to I^4 (though not quite); but even so, this comparison does not lead to an obvious choice of one source.

The last section of the briefing uses examples of variations in source strengths and timing to argue against multiple sources. The uniformity requirements assumed in the briefing are much greater than we have been used to. Uniformities of 20% or 10% or even less mean that the use of tailored absorbers could help a great deal, but they are not considered. It is true that they would help the single source more than the array. K-Tech also spoke in Albuquerque of variations of angle of incidence over the object as being a concern.

SECTION 5
VACUUM POWER FLOW

5.1 BASELINE VACUUM POWER FLOW DESIGN.

### 5.1.1 Schlitt-Miller Design Approach and Results.

The front end design process begins with an initial assessment of MITL lengths and gaps, tube size, allowance for tube interface connection to MITLs and water cones, and water cone lengths and electrode separations. Impedance profiles are calculated and an equivalent circuit model created. Circuit performance with an imploding shell load is modeled and voltage waveforms through the model determined. These are used to check stresses against design criteria, gaps are adjusted, impedances recalculated and the process iterated until self-consistent. Design stress criteria are

- Shell load with 10:1 compression ratio; initial load inductance was set at 2 nH.

- MITL gaps are set such that cathode fields due to the voltage pulse are to be below an emission threshold of 300 kV/cm until the current rises to the point that the dynamic impedance, V/I, is less than 1/3 Z, (Z the local geometrical impedance) assuring magnetic cutoff of emitted electrons.

- Tube insulator stress is permitted to reach 100% of "JCM" or $F\ t^{1/6}\ A^{1/10} = 175$, for the combined area of tubes in four modules, by 8 ns before the implosion time, at which point any further power flow is unusable and the interface can be permitted to flash over.

- Positive electrode stress in water is permitted to reach the level given by the expression $F\ t^{1/3}\ A^{0.058} = 0.23$ where the electrode area corresponds to that for all 4 modules in parallel by 100 ns past the implosion time. The constants in this expression (0.058, 0.230) were determined by R. Eilbert and W. Lupton at NRL in 1968 from analysis of water breakdown data by I.D. Smith and include data by J. Shipman out to ~5500 cm^2. Subsequent machine design used this criterion as predictive of breakdown and operating stresses were kept below predicted breakdown levels. Operation of more recent, larger, machines tends to show that the criteria may be too conservative and may be taken as predicting maximum permissible operating levels. However, there is the conjecture that at some point the area scaling levels off. That is, the permissible operating stress does not become arbitrarily low as the area becomes arbitrarily large. Peak stress on large area electrodes could then be determined by the spacing required to avoid point to plane breakdown from the worst case defect at the applied voltage. This possibility was considered by JDOST and identified as an issue meriting further investigation; it still is. However, it is reasonable to assume that point-plane criteria may provide a valid basis for design of very large area systems. The system size and cost advantages should be evaluated and experimental validation of this criteria is an appropriate R&D task.

- Oil stress (+ ve) $F\, t^{1/3}\, A^{0.073} = 0.48\, f$

    $f = 0.8$ max for 4 drivers (if oil insulated).

- If oil is used as insulation in, say, the driver section the applicable breakdown stress criteria (from the JDOST) based on a considerable data base is $F\, f^{1/3}\, A^{0.073} = 0.48$ where an 80% safety factor (i.e. derated by 20%) is used for an area corresponding to four modules.

Water and oil stress criteria are those agreed upon in the JDOST review for similar large machines.

Iterative computer based analysis produced a conceptual front-end model. The resulting one-line equivalent to the four parallel power flow channels is shown in Figure 53, nominally locating the centerline through water cones, 4-slot vacuum tube and MITLs, down to a two-fold posthole convolute to the load. Gap spacings satisfy design electrical stress criteria and fit within the cone. A radial dimension of 10 cm at the tube is allowed for flaring water cones to insulator stack and 25 cm allowed to connect to the MITLs (vacuum flares). Insulator length is 55 cm per slot. Inductance from tube to load is 22 nH, in large part due to the extended (~2.4 m) MITLs.
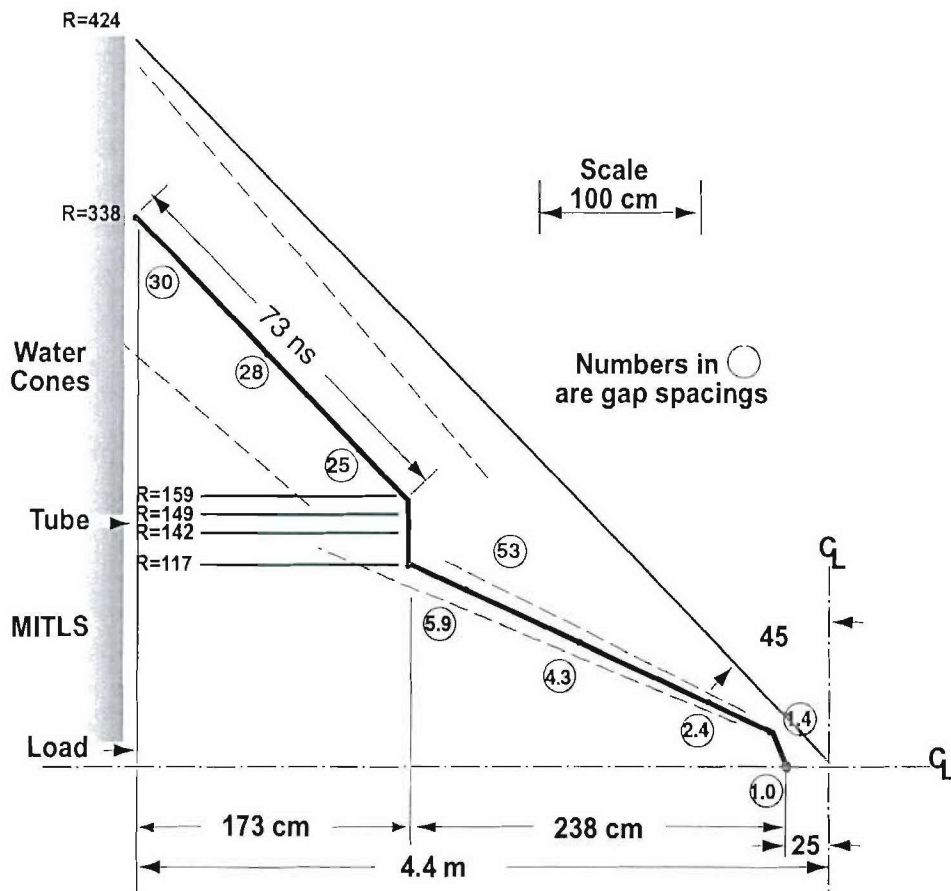
Figure 53. 250 ns Direct Drive front end conceptual model.

The next step towards a mechanical model is a layout of the four parallel power channels, centered on the four tube slots, to verify volume available to accommodate the required conductor spacings. As shown in Figure 54, the power flow channels fit within the cone. However, there is no allowance for structure, finite thickness conductors, bracing, mounting and insulation of subassemblies nor considerations of manufacturability, parts tolerances, assembly and maintenance. The power flow channels extend out to the boundary of the cone.
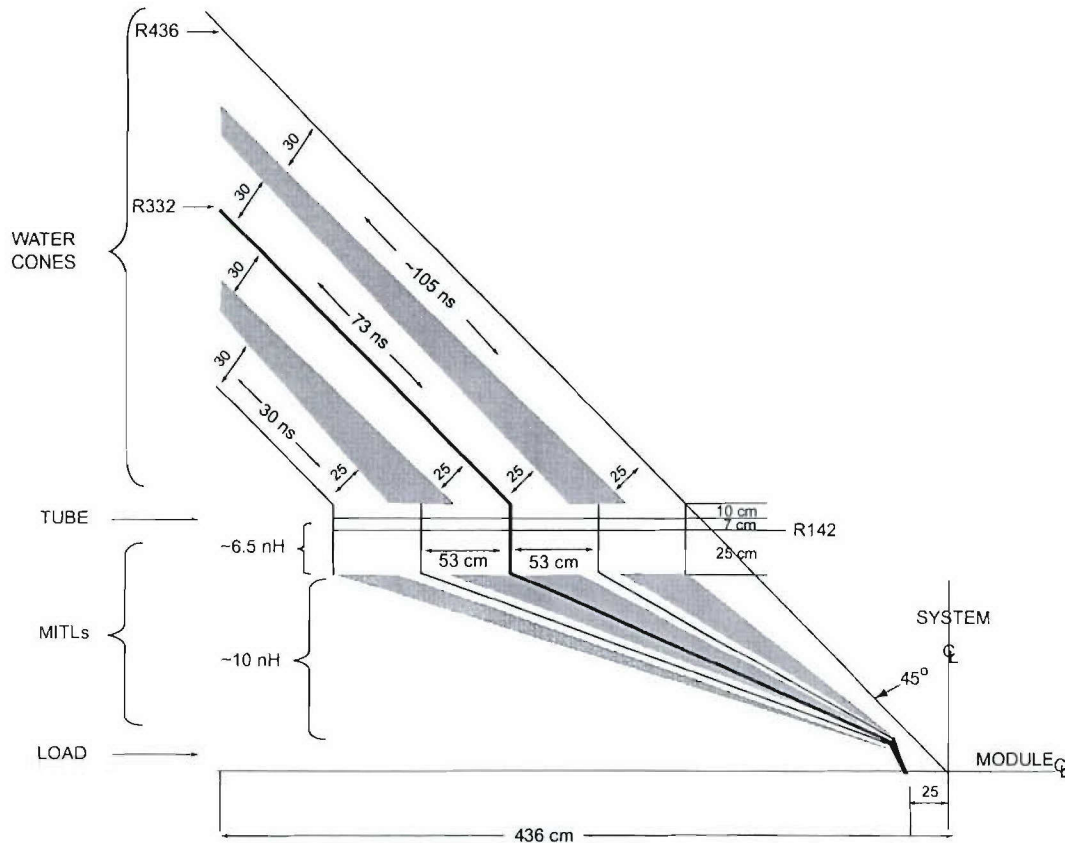

Figure 54. A layout of the four parallel power channels, centered on the four tube slots.

The preliminary structural design approximation locates the water cones, tube and MITLs within the desired conical volume. In Figure 55 separation between modules is set at 1.5 inches. The exterior conical shell is a ¼ inch plate and is rounded up and reinforced by 8 inch x 58 lb/ft wide flange. Front end supports to grade are not shown. To assist fabrication all cones have the same angle resulting in a slight spacing increase at the tube. The spacing increase raises impedance in this region with minimal effort on performance and allows higher voltage. All interior metal parts are stainless steel. Exterior is structural carbon steel and the outer shell is stainless clad carbon steel plate for economy in fabrication. The tube details are approximations, no attempt has been made to achieve grading and connection, support and mounting details have yet to be added. The inner cone structural support features provide for insulated mounting assembly and maintenance. Insulating support pylons in a number of locations position the high voltage

conductors between ground cones. Metal pylons support ground cones and reference their position to the outer shell. These pass through "hot" cones in an arrangement similar to the vacuum posthole convolutes. Initial assembly is effected by positioning the outer shell and installing the outermost hot cone which is located by the insulating pylons. The mid-ground cone is installed and supported by the outer shell by metal pylons passing through graded holes in the first hot cone. The remaining hot and ground cones are mounted in the same way. If, in operation, an insulating support were to track or arc electrically, the design is such that the affected pylon can be removed and replaced without dismantling the entire assembly. That is, the supports are redundant and can be replaced individually from outside the outer shell or inside the inner one. The input termination to the water cones is a double ring of 30 – 1.2 meter diameter insulating barriers. These would be used to separate an oil-insulated driver from the water dielectric cones. Parallelism of many small terminals reduces the net terminal inductance and eliminates the need for a single 9-meter diameter plastic barrier. Total weight of the front end assembly is estimated at 200,000 lbs of which 115,000 lbs is water.
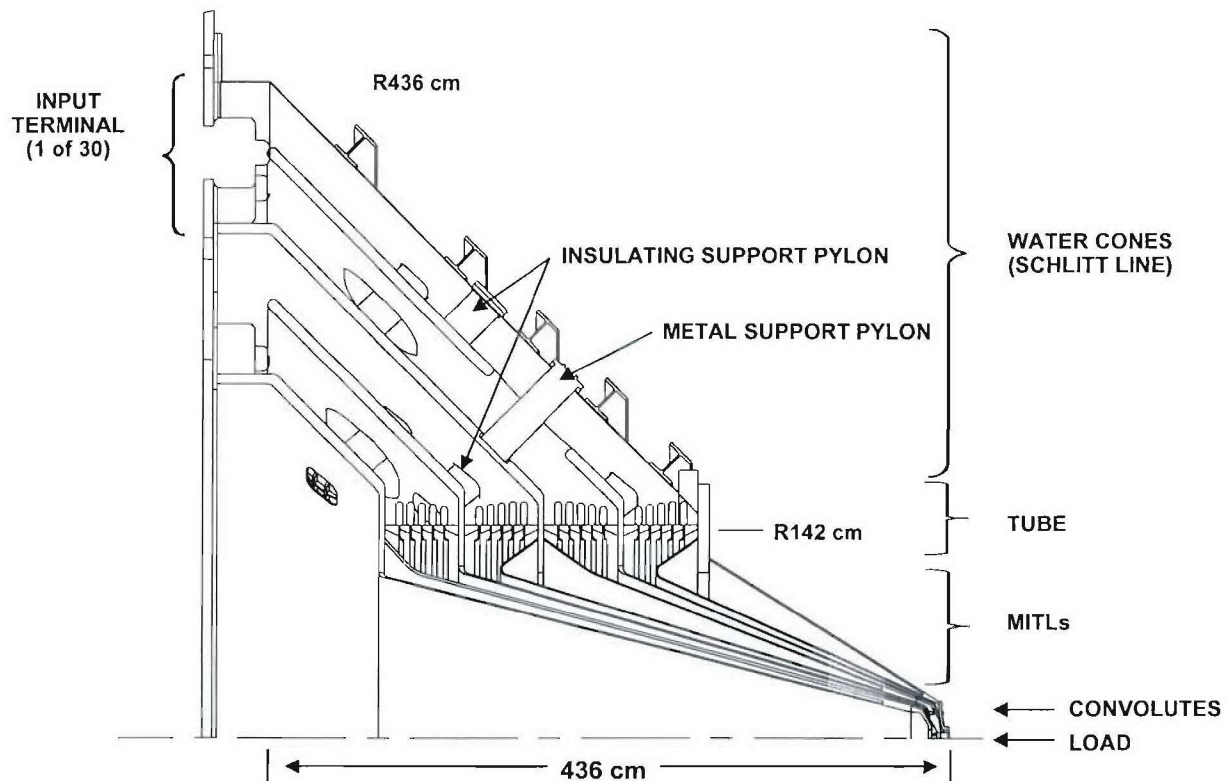
Figure 55. 250 ns modular Direct Drive front end structural design approximation and driver interface concept.

The equivalent circuit for this front end (see Figure 22 of the previous section) shows the multiple, parallel power flow from driver to load. At a driver output voltage of 6.6 MV the peak load current is 30 MA for an implosion time of 250 ns. Driver output current peaks late (≈650 ns) at ≈40 MA.

The front end design assumed a driver having a characteristic discharge time of $\sqrt{L \bullet C} = 300$ ns. This is larger than optimum and inefficient but thought to be achievable from a Marx generator. The initial front end analysis sets its charge voltage at 5.8 MV. With an output capacitance of 3 µF and series inductance of 30 nH, 50 MJ are stored and peak currents approach 30 MA. It is now understood that ≈35 MA are required and the charge voltage would be ≈7 MV. This affects consideration of the various drivers proportionally.

5.1.2 Driving Voltage and Front End Inductance Estimates From Simplified Scaling of The "Z" Stack With Voltage.

This section presents estimates for the front-end inductance, optimum stack radius, and peak load current vs. stack voltage for two of the 100 ns implosion time loads. The first load is the 40 MA, 400 kJ Kr-K, 4 cm long, 3.6 cm initial radius shell PRS load. The second is a 48.5 MA, 400 kJ Kr-K, 3 cm long, 4 cm initial radius shell PRS.

The starting point for these estimates is Ian Smith's February 1998 analysis done originally for "X-1" under SNLA funding and titled "Simplified, Optimistic Scaling of Z-Stack with Voltage." Figure 56 summarizes Ian's results and the assumptions used in the analytic scaling. The vacuum flare cross sectional area scaling is stated as optimistic in that it doesn't correspond to the reentrant anode/flat cathode flare configuration presently demonstrated on "Z". Specifically Ian proposed using a ~2/3 reentrant cathode/~1/3 reentrant anode flare. Development and demonstration of such a flare configurations is a recommended R&D topic because of its high leverage in reducing the inductance of the higher voltage tubes that will be necessary to achieve >40 MA PRS drive currents.

For the new NGM estimates: 1) The NGM load dimensions were used to set the load inductance and the radial location of the convolute, assuming a 2 cm long, 1 cm gap final radial feed. 2) The convolute was taken as a "standard" Saturn-type 1 nH DPHC with its inductance adjusted to account for a radial location different from the 10.5 cm mean radius of the 1 nH DPHC. 3) The system MITL impedance (in ohms) was adjusted to be 1/8 times the system inductance (in nH) interior to the beginning of the constant gap portion of the MITLs. [This scaling is inferred from the original MITL design optimizations for the C & D and A&B levels on "Z"]. 4) Conical MITLs were used as necessary to locate the PRS flush with the top (or bottom) of the insulator stack

Figures 57 through 61 develop the expression for the inductance of the "40 MA" 100 ns system, L being a function of V and R, the stack radius. The results is:
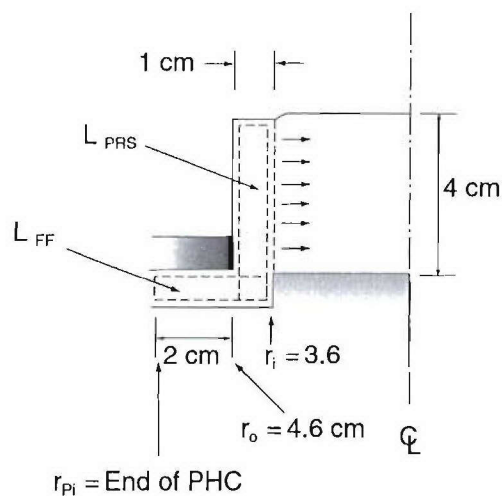
$$L_{total} \cong 4.82 + \frac{A}{2R} + 0.02 \left[(22V)^2 + (R - 2.2V - 25)^2 \right]^{\frac{1}{2}}$$

where
$$A = 12.5V^2 + 80V$$

70
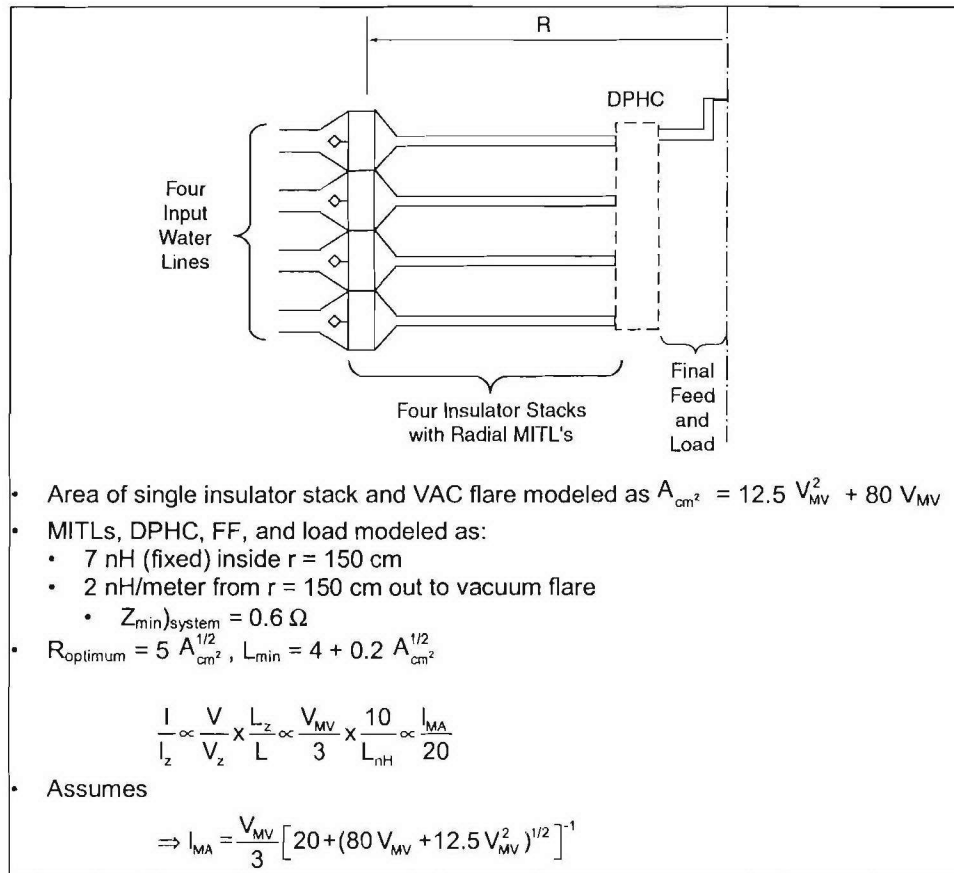
Figure 56. "Simplified optimistic scaling of Z-stack with voltage," I. Smith, 2-4-98, [work funded by Sandia National Lab].

Figure 57. 40 MA load inductance.

$$L_{DPHC} = \frac{\bar{R}_P =)_{Saturn}}{\bar{R}_P)_{Saturn}} \times L_{DPHC}) ; \frac{10.5}{8.6} \times 1nH = 1.22\,nH$$

$$\left[\begin{array}{l} N.B.\ PHC\ extends\ from\ r_{P_o} = 10.6\,cm\ to \\ \qquad\qquad r_{P_i} = 6.6\,cm \end{array} \right]$$

Figure 58. DPHC and TPHC inductance [scaled from Saturn DPHC].

DPHC Case

Inductance inside r = 10.6 cm = 4.39 nH

Z individual MITL design result translates to:

    8 Z_{MITL} (system equiv.) $\simeq$ L (system equiv.) interior to start of constant gap MITL, gap = 1 cm

Let R = radius where const. Gap MITL starts:

$$8\left(\frac{60\times1}{4R}\right) \simeq \frac{1}{4}\ln\left[\frac{R}{10.6}\right] \times \frac{60}{30} + 4.39$$

$$\Rightarrow R = 25\,cm$$
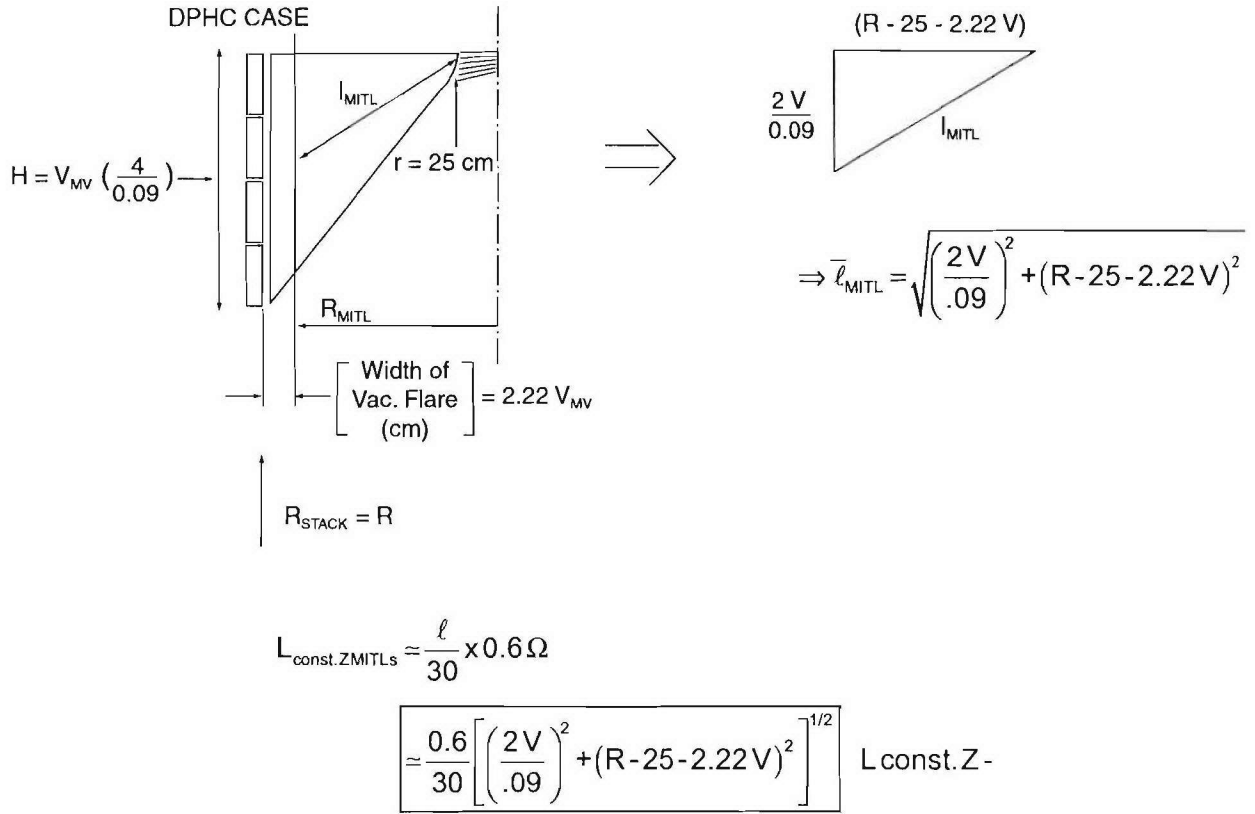
$$\Rightarrow Z_{MITL}\ (system\ equiv.) = \frac{1}{4} \times \frac{60\times1}{25} = 0.6\,\Omega$$

(by coincidence, this is the same as the Z MITLs)

Thus, L of const. Gap MITLs is:

$$\frac{1}{4}\left[60\ln\left[\frac{25}{10.6}\right] \times \frac{1}{30}\right] \sim \boxed{0.43\,nH}\ L\ const.gap$$

Figure 59. MITL inductance scaling – constant gap region.

Figure 60. MITL inductance - constant Z region.

$$\text{DPHC Case:}$$
$$L = \frac{1}{4} \times \left(\frac{2A}{R}\right) = \frac{1}{2R}\left[12.5V^2 + 80V\right]$$

(which represents no change from 2-4-98 assumption)

Figure 61. Stack Inductance Calculation.

The graph on Figure 62 plots the optimum stack radius, the minimum front-end inductance, and the current (scaled from "Z" as I= {20MA x V/3MV x 10nH/L}) as a function of stack voltage. The voltage and inductance values corresponding to the 40 MA load are 7.7 MV and 13 nH, with an optimum stack radius of 220 cm. The "gray" line shows Ian's previous result for very similar (by coincidence) impedance MITLs and central region inductance, to show the penalty for requiring conical MITLs to move the source flush with the end of the insulator stack.

73
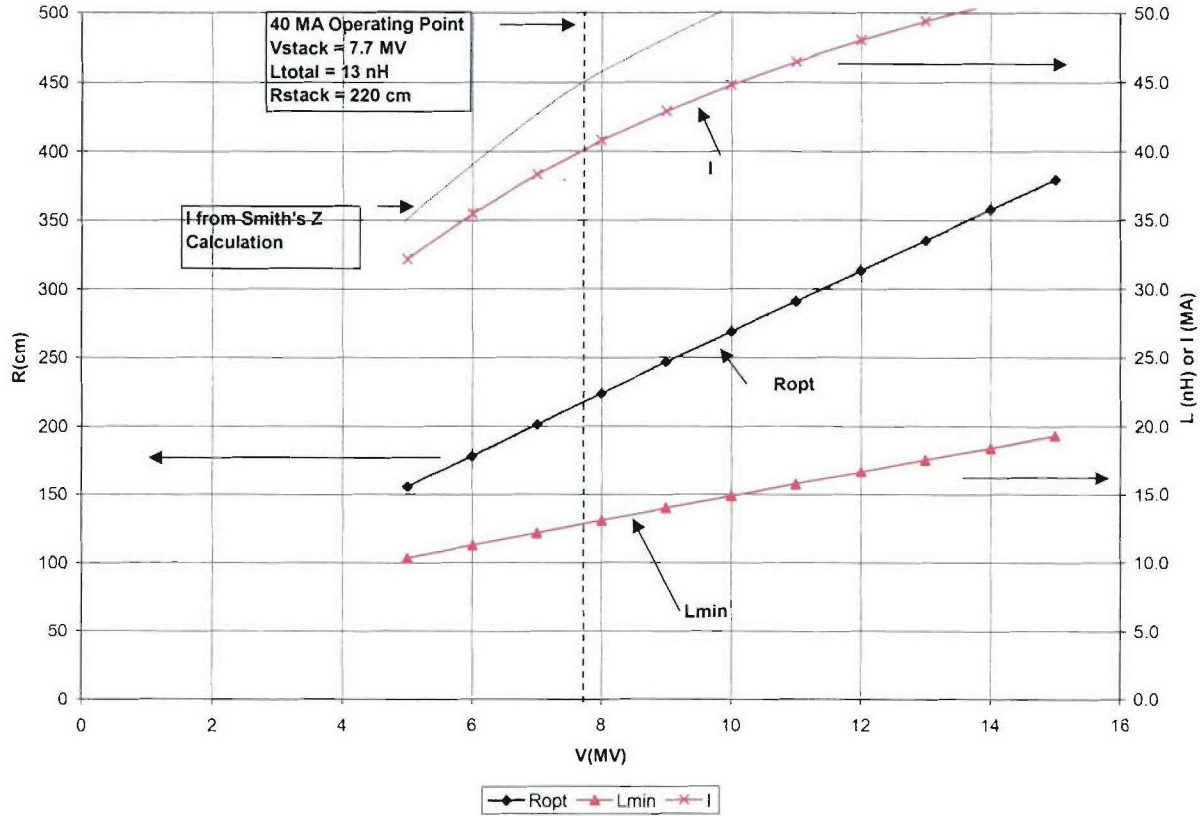
Figure 62. Inductance, current, and radius results for the 100 ns NGM case.

Next the procedure was repeated for the "48.5 MA", 3 cm long load from the 100 ns optimization scans to validate the inductance assumptions made in the scans. The results were approximately 11 MV and 15 nH, with an optimum stack radius of 320 cm. This compares with 13.3 MV for the 16 nH assumed in the scan in Section 3, where the driver $\sqrt{L \bullet C} = 50$ ns.

The model was then applied to a triple post-hole convolute (TPHC) architecture in attempt to investigate the benefits, if any, of using a six-level stack with six instead of four power flow "slots". Results for the six-slot case are 12.3 MV and 16.9 nH, with an optimum stack radius of 306 cm for the 48.5 MA load case. For these modeling assumptions there is no benefit to using the more complex six-slot, TPHC, configuration. Finally, a two-slot SPHC case was modeled. For the 48.5 MA load, a drive voltage of 22.5 MV is required for the "optimum" 640-cm radius, 30.9 nH stack. Thus the four-slot, DPHC, architecture is the best of the three post-hole convolute configurations considered.

5.1.3 Insulator Stack Inductance Reduction.

The PBFAZ machine at SNLA has demonstrated 15% higher fields for the insulator stack breakdown than the standard JCM formula would have predicted. SNLA used cross-linked

polystyrene to make the very large diameter rings used in PBFA-Z. SNLA also used the MITL theory that has been developed over the last 20 years by Creedon, Mendel and others to design the well-insulated conical MITLS also used in PBFAZ. We suggest that any future point designs should consider using these demonstrated design criteria. A rough estimate of the improvement in the point design presented here, suggests that the design inductance with the DPHC may have been reduced by about 1.25 nH. The TPHC inductance may be reduced by about 0.75 nH. The TPHC sees less of an effect since the affected components were a smaller part of the whole having 50% more of them in parallel.

5.1.4 Vane-type Convolutes.

Some vacuum inductance reduction could be realized by using vane-type convolutes instead of the Double Post Hole Convolute (DPHC) or Triple Post Hole Convolute (TPHC) configurations previously discussed. The structure would invoke many (tens) of alternating cathode and anode vanes. This configuration has two convolutes:

- Outer – for the transition from the disk feed through the insulator stack to blades
- Inner – for the transition from blades to the final radial disk feed.

The inner section vanes and convolute can be lower inductance than the DHPC equivalent, but the outer convolute may be more inductive than the DHPC, especially if it must be non-emitting. R&D will be required to further evaluate the benefit of this design option.

5.2 VACUUM POWER FLOW POWER MULTIPLICATION SCHEMES.

5.2.1 Motivation for Vacuum Power Multiplication Schemes.

Increasing the time allowed for the energy to flow through the vacuum interface reduces the pulse compression required from the pulse generator stages, and it also has the important effect of making the critical vacuum power flow elements easier to design, smaller, and cheaper. Allowing a longer implosion time for the Z-pinch is one method of increasing the time allowed for energy to flow into the vacuum, and longer duration Z-pinch drives are under development by DTRA. Pulse compression within the vacuum is an alternative; this can aid Z-pinch performance by keeping the drive time short or actually reducing it, and it can also allow other loads such as bremsstrahlung diodes to be driven.

Plasma opening switches have been developed for vacuum pulse compression but with limited success owing to the complexities of the plasma opening process. Recently, flux compression has been put forward as an alternative vacuum pulse compression scheme; flux compression again involves plasmas, but it relies mainly on the dynamics of magnetically-accelerated dense plasmas with no requirement for an opening phase. Early results of tests carried out on Z by Sandia and CEG were encouraging, generating ~19 MA with a rise-time shortened from 100 ns to tens of ns.

Another plasma switching scheme that relies only on the magnetic acceleration of dense plasmas and not on opening is the L-dot switch. This was studied by PI in the 1970's in the $\gg 1$ µs drive

time regime, but until recently has not been considered as a means of pulse compression in the sub-microsecond range, where migration of plasmas into undesirable regions is easier to avoid.

Recently several innovative concepts for Advanced Power Flow have been introduced to drive PRS loads based upon the concept of power amplification in vacuum. These concepts are based on current multiplication and magnetic field flux compression in vacuum. The current doubler (CD), a variation introduced by Dr. L. Rudakov on Dr. O. Zucker's current multiplication schemes, is a two-turn current device constructed using vacuum convolutes to realize the two turns. The flux compression (FC) schemes, introduced by CEG French researchers, consists of driving with a primary circuit, a plasma liner that compresses the flux of the secondary PRS circuit. In the case of the CD the object is to increase the magnetic density driving the PRS, and thus the kinetic energy per unit length into the PRS pinch, to obtain more efficient kinetic energy to K-shell radiation conversion. In the case of FC the objective is both to increase kinetic energy per unit length and reduce the effective implosion time, again for more efficient conversion of the kinetic energy into radiation (both total and K-shell).

A concept that combines both CD and FC, we shall label CDFC, uses a CD as the primary circuit of the FC liner, and enjoys the advantages of both. We will also describe a FC concept to drive a single wire load driven by a wire array imploding onto the wire in a conical geometry (FCSW).

The potential gains afforded by these innovations are large. For instance, preliminary 0D calculations show that the CDFC is capable of increasing three-fold the argon K-shell radiation output for DQ in the water coupler model.

Generally these innovations all share the desirable attribute that they result in very compact inexpensive devices. Their size is small, linear dimensions being of the order of a few tens of cm. These devices produce the desired vacuum power amplification by plasma motion, either from a wire array liner that turns into plasma, or in the case of the L-dot switch, from a plasma source. The need then arises to stabilize and control plasma motion, possibly by incorporating slow B_z fields produced by ancillary coils.

5.2.2 Detailed Descriptions.

L-Dot Switch

This approach for PRS loads was discussed by L. Rudakov at the 1999 IEEE Pulsed Power Conference in the paper "New Loads For Pulsed Power Generators." His paper contains the detail.

Current Doubler

The current doubler (CD) presented here is a device placed on the front-end of the pulsed power driver. The CD does not require any switches. This device includes two loops of input current I(t) from the generator. The load, an imploding shell, is a part of the two-turn current loop. The schematic for this design of CD is shown in Figure 63, with typical dimensions to appreciate its small size.
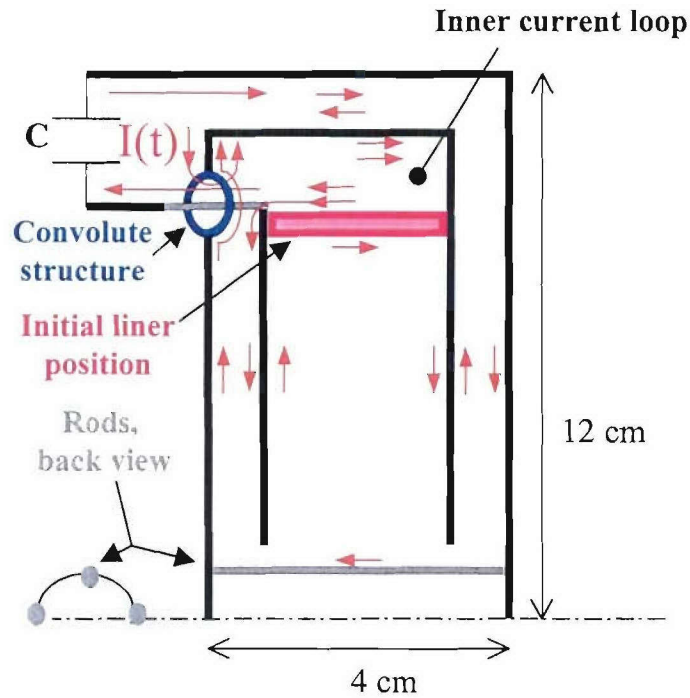
Figure 63. Conceptual current doubler configuration.

The current I(t) flows along the internal surface of the external axial and radial coaxial structure which includes the inner diameter axial rods, to the convolute structure. The current then follows an "inner current loop" which includes the outer diameter of the imploding liner load and returns through a combination radial and axial path on the inside of the external coax structure once again to the convolute structure. This path includes the inside diameter of the imploding liner. At the convolute the current once again follows a current path which includes the "inner current loop" along the outer diameter of the imploding liner load and returns to the driver via the convolute post. As a result, the load wire array is accelerated by the magnetic fields of the doubled current 2I, and decelerated by the field of a single current I. The resulting increase in the accelerating magnetic pressure is 3-fold. The accelerated shell radially implodes, moving along the parallel disc-like inner radial electrodes. At the end of acceleration, the plasma penetrates through the array of rods and stagnates on axis. The main idea of this concept is for a given driver to obtain about the same efficiency of conversion of driver energy into PRS kinetic energy, by producing similar changes in driven inductance. However, the PRS kinetic energy per unit length for the CD increases by about a factor of 3 with respect to the usual case because of the current doubling, which means that denser pinches could be produced, thus increasing the conversion of kinetic energy to K-shell radiation. (First discussed in "Novel Approach to Producing ~10 keV X-Rays with Plasma Radiation Sources Powered by Long Pulse Drivers," a White Paper by L. I. Rudakov, J. Davis and E. Waisman, submitted to DTRA in October, 1999).

Electrically Driven Flux Compression

This concept, amply discussed by the CEG French researchers in various DEA meetings is schematically illustrated by Figure 64 which shows the evolution of the currents and plasmas in both the primary and secondary of a generic flux compression configuration.
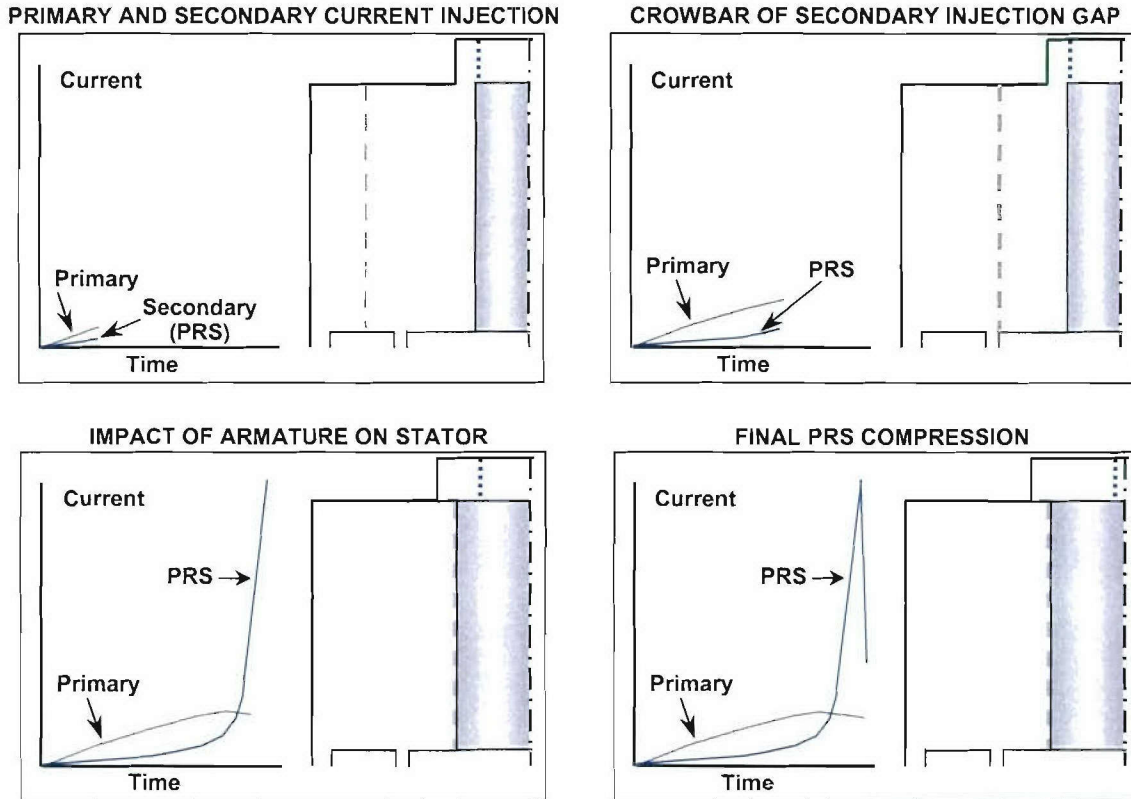

Figure 64. Steps of operation in flux compression.

To further illustrate this concept we show Figure 65 the schematic of a circuit analysis we did for DQ to show the potential for this concept. Preliminary results from the analysis are shown in Figure 66. The model predicts that implemented on DQ, argon K-shell yields could approach 133 kJ.

Under a separate contract we are currently analyzing the question of stabilization of the RT instability on the plasma armature by utilization of slow B_z component, this work is being done with NumerEx as subcontractor, utilizing the 2-D MHD code MACH2. We are also in collaboration with Sandia and CEG in following the experiments being conducted in these institutions, as well as in collaboration with CEG to modify and utilize the 2-D MHD DELTA in the study of FC devices.
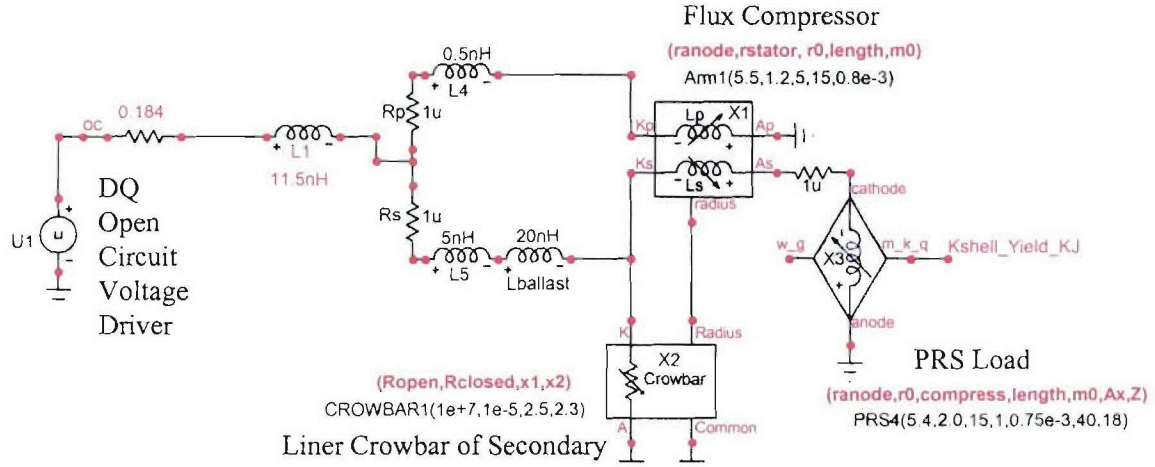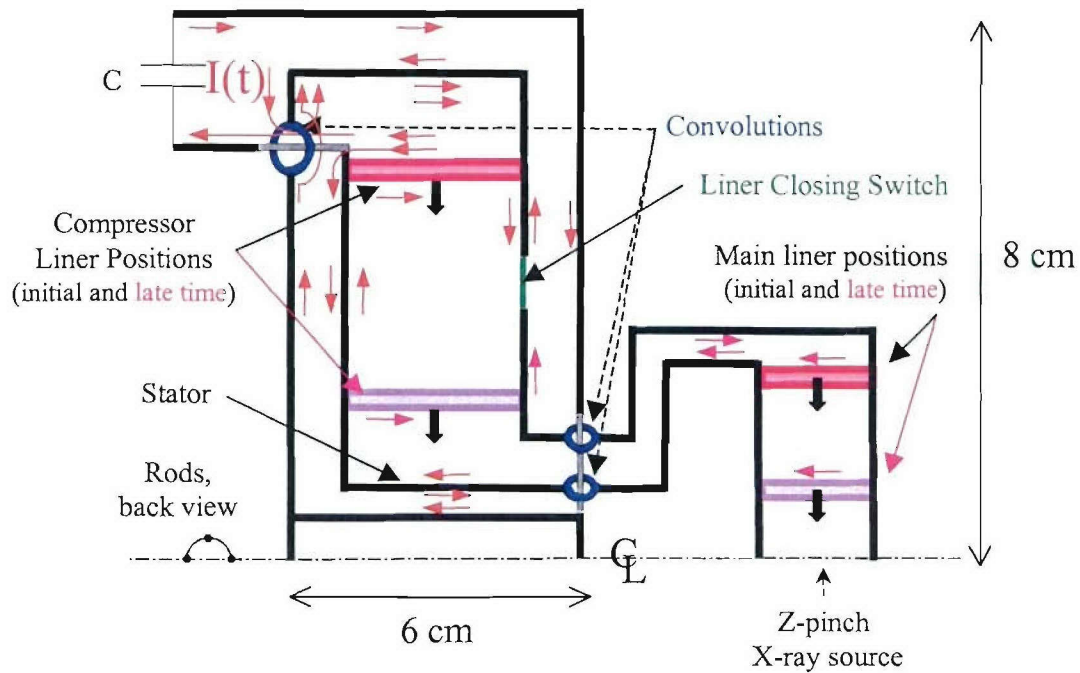
Figure 65. Equivalent circuit for an implementation of flux compression on DQ.
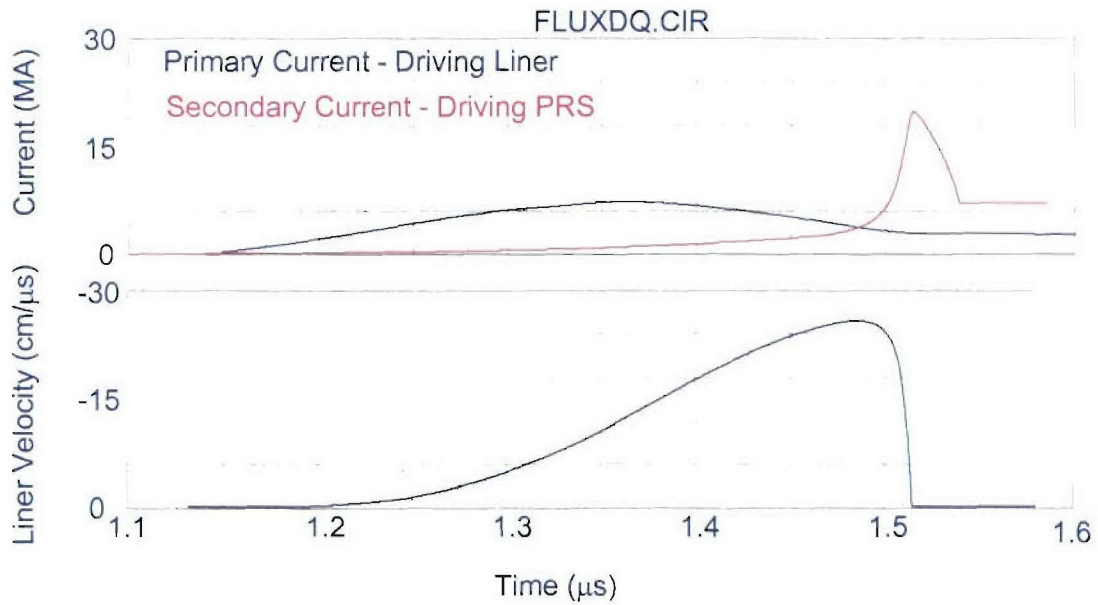
Figure 66. Preliminary result from the DQ flux compression model shown in Figure 67

Current Doubler + Flux Compressor (CDFC)

The main idea of this concept is to combine a current doubler with a flux compression device as shown in Figure 67.

Figure 67. Example of a combined current doubler and flux compression scheme.

The concept has been preliminarily investigated under a separate DTRA contract and has a number of advantages:

- A CD makes it possible to increase the magnetic pressure driving the imploding wire array liner by a factor of four. The armature (liner) length can then be reduced by a factor of four with respect to the traditional FC scheme for the same kinetic energy of the armature.

- There is no need for any special switches to shorten the current pulse. A moving plasma shell in the first section of the CDFC operates as a switch and a compressor of magnetic flux, which is captured when the shell crosses the flux gap.

- There is no need to have a separate current circuit to provide the initial magnetic flux for the compressing section. The first current loop of the CDFC induces the required magnetic flux in the compressing section through the flux gap.

- The magnetic flux compression ratio required for successful operation of the CDFC should be less than that needed for the CEG FC scheme, because of the 4-fold increase in magnetic pressure in the flux compressor. Also, since the parasitic inductance at the time of impact with the stator, due to RT instabilities is proportional to plasma length and the magnitude of the deceleration, one can expect the RT instability of the flux-compressing plasma shell to be less damaging.

- This scheme can be used efficiently for DQ-like generators and for future innovative generators to drive Z-pinch loads. A conventional, 5-10 MJ Marx generator with a nearly microsecond rise time is sufficient to drive the CDFC. Our preliminary calculations with a simplified electrical circuit predict currents for the CDFC driven by such a generator approaching that of the output of the Z machine. It is conceivable that the cost of such a generator would only be in the few tens of millions of dollars.

Figure 68 shows an equivalent model for the combination current doubler/flux compressor on DQ. Figure 69 give some preliminary result from the circuit simulation. The unoptimized modeling which utilizes a more realistic rebound of the current doubler/flux compression shell on the stator than the one used for the previously shown case of pure FC, suggests up to 105 kJ of Ar K-shell may be produced on DQ.

Our preliminary study identified magnetic insulation in the additional convolution holes from compressor to load as an important challenging issue to resolve for the CDFC scheme. And, of course, the problem of limitation of achievable magnetic flux compression ratio due to the RT instability, as in the pure FC idea remains a key issue.
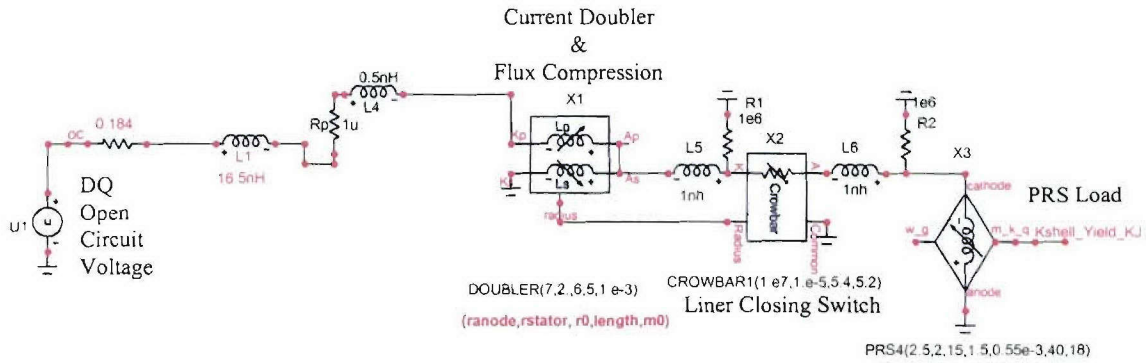
Figure 68. Equivalent circuit for a possible implementation of the combination current doubler/flux compressor on DQ.
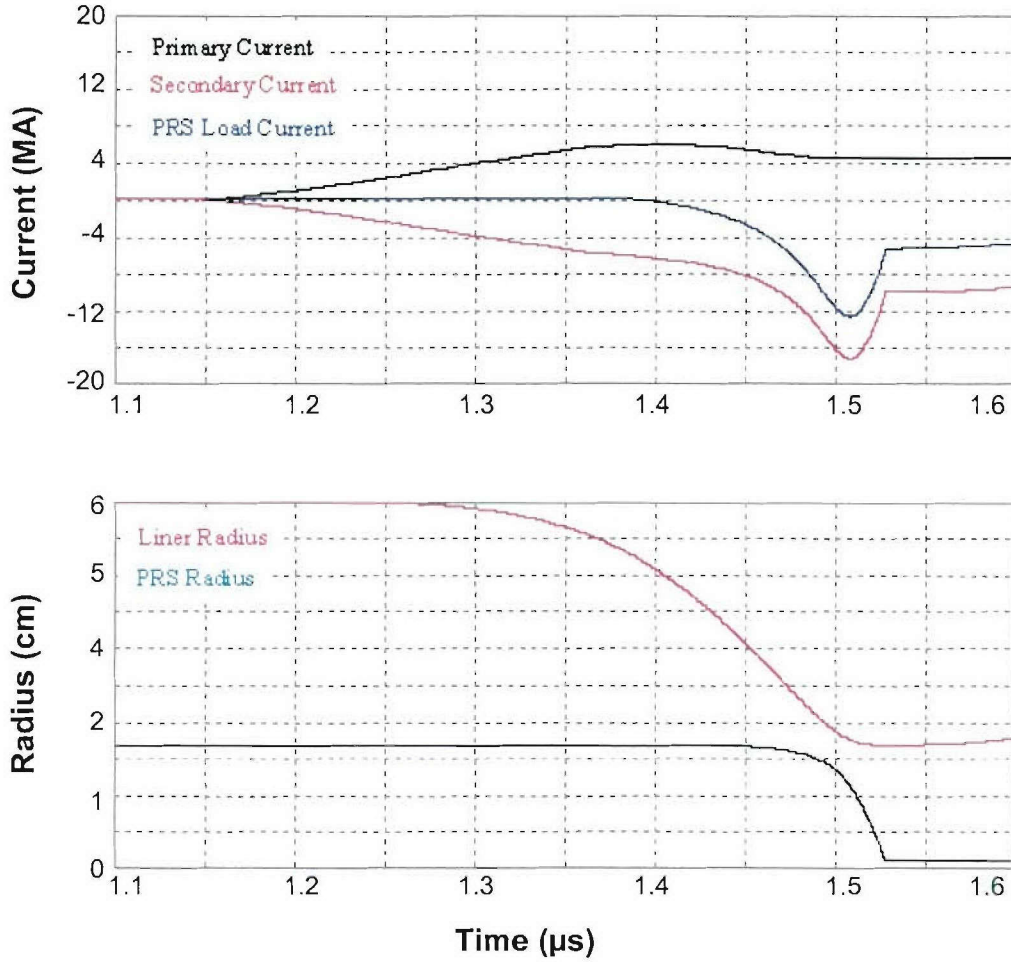
Figure 69. Preliminary results from the combination current doubler/flux compressor model for DQ shown in Figure 65.

Flux Compression on a Single Wire (FCSW)

The basic idea of the FCSW concept is to maximize flux compression by having no inherent parasitic inductance between the imploding liner, which closes the primary circuit, and the PRS load in secondary circuit. In addition, taking advantage of a convergent geometry, as shown in Figure 70, one may further increase the compression factor. This concept, suggested by J. Goyer, potentially extends the magnitude of flux compression beyond that expected via more standard FC approaches. The obtainable compression factors will likely be limited by instability induced, distributed current structures in the imploding liner and the single on-axis wire at the time of maximum compression. In addition to many of the same physics issues involved in the standard FC approaches such as liner stability, the radiation physics of the on axis wire is important, as well as time-scales for the processes. Simple 0-D modeling has suggested very short, few 100 ps to few ns time-scales for the final phase of current compression. There is the

potential that single wires in this configuration may be able to produce abundant quantities of non-thermal x-rays in the energy regime equivalent to low voltage bremsstrahlung.
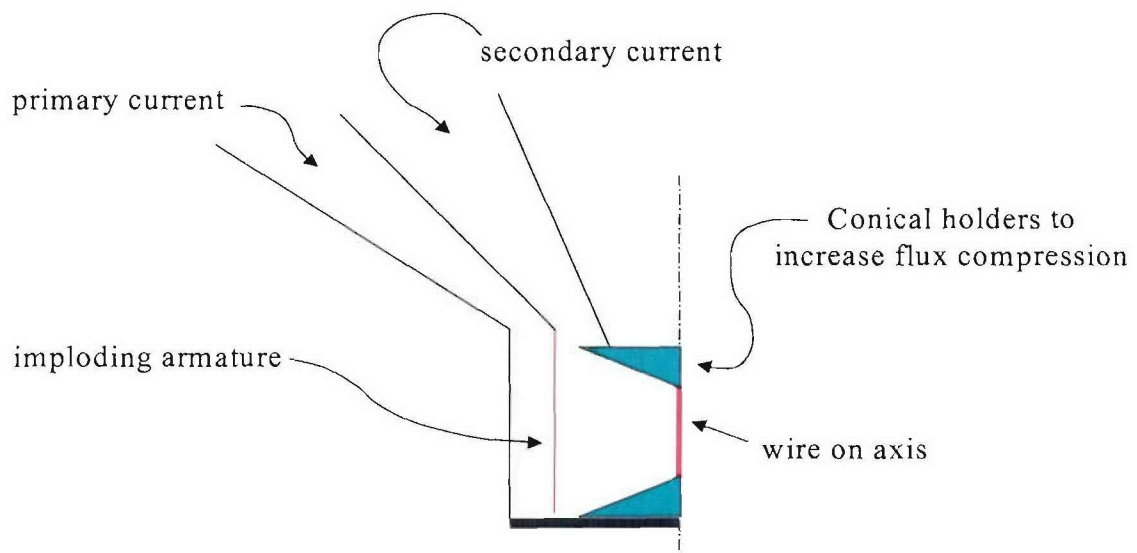
Figure 70. Cartoon exhibiting the idea of flux compression on a single wire (FCSW).
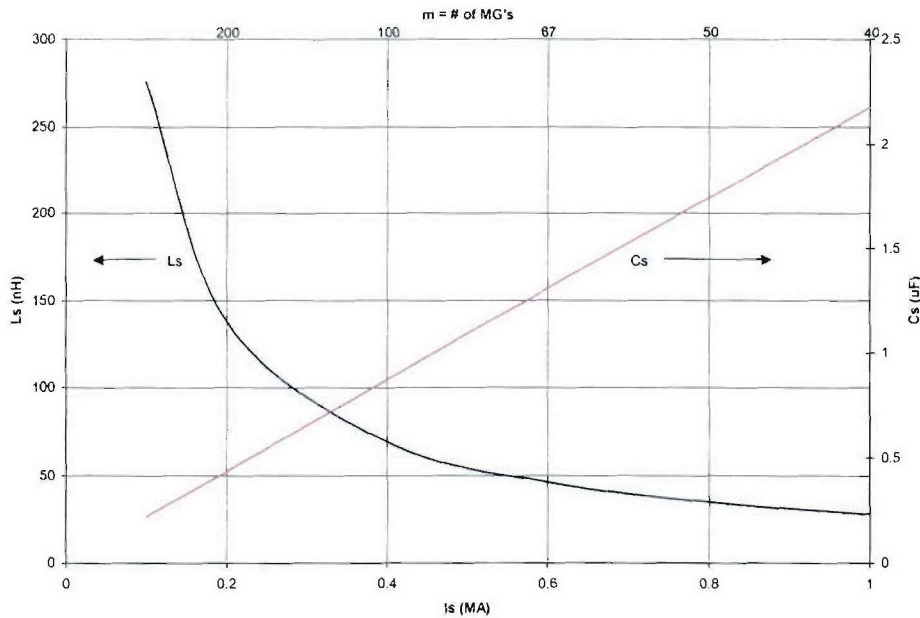
SECTION 6
DRIVER CONFIGURATIONS

As shown in Section 3, the feasibility of the Point Designs is directly affected by the $\sqrt{L \bullet C}$ time of the primary energy store. The $\sqrt{L \bullet C}$ of the prime energy store is a result of the $\sqrt{L \bullet C}$ of the capacitor-switch building block used in assembling the driver. As shown in Section 3, Table 11, a $\sqrt{L \bullet C}$ of 500 ns is approximately the state-of-the-art. Our most attractive point designs depended on development of "Fast" $\sqrt{L \bullet C}$ = 300 ns and "UltraFast" $\sqrt{L \bullet C}$ = 175 ns stages. In this section we will discuss concepts for these improved capacitor-switch stages and the associated prime energy driver configurations they enable.

6.1 $\sqrt{L \bullet C}$ = 300 ns STAGE CONCEPT.

The trade-space for a $\sqrt{L \bullet C}$ = 300 ns, 40 MA, 5.8 MV MGD is shown in Figure 71. For n series stages in each of m parallel Marxes where n is set by the desired voltage and m by the current, the required stage capacitance and inductance vary with m.

Figure 71. Trade space for stage parameters for a $\sqrt{L \bullet C}$ = 300 ns, 40 MA, 5.8 MV MGD. Calculation assumes total MG capacitance of 3 μF and MG inductance of 20 nH with 10 nH of connection inductance.

84

What Figure 71 shows is that we cannot arbitrarily utilize components (say, existing spark gaps and capacitors) to produce the required Marx driver. A high energy density capacitor is of no use if it does not have the current capability and combined switch-capacitor inductance to meet our driver requirements.

If, for example, to minimize components and complexity we consider a maximum stage current of 1 MA, m is then 40 (the ultimate peak Marx current is ≈40 MA). With 40, 5.8 MV, 29 stage (200 kV/stage) parallel Marxes, the stage capacitance is ≈2 μF to achieve a 3 μF array capacitance and the maximum allowable stage inductance is ≈30 nH. Alternatively if maximum reliable stage switch (or capacitor) peak current is a limiting factor, say 150 kA, then m = 267 Marxes are required, the stage capacitance is 0.33 μF and maximum permissible stage inductance = 185 nH. From this we see the advantage of minimum inductance architectures and high current capability switches and capacitors. Moreover, it is apparent that an optimum design will require capacitors and spark gaps specific to the application.

The conceptual design for a $\sqrt{L \bullet C}$ = 300 ns stage is shown in Figure 72. The stage parameters are:

- $L_s \leq 125$ nH
- $C_s = 0.75$ μF
- $V_s = 180$ kV (±90 kV)
- $W_s = 12.15$ kJ.

To achieve these parameters will require the use of rail gap switches, capacitor element repackaging and integrated capacitor-switch connections to produce a low inductance architecture.

An MGD built from this building block specifically for the 400 kJ/250 ns MGD-peaking capacitor Point Design is also shown in Figure 72. The properties of each MGD are:

- n = 34 @ 6.12 MV
- W_{MG} = 0.413 MJ
- m = 70
- for $W_{MG\ Total}$ ≈ 29 MJ.

6.2 $\sqrt{L \bullet C}$ = 175 ns STAGE CONCEPT.

The conceptual design for a $\sqrt{L \bullet C}$ = 175 ns stage is shown in Figure 73. To realize this stage will require an R&D effort in:

- Rail-gap switch performance
- Low inductance, high voltage connections (capacitor terminal to switch).

The associated MGD also shown in Figure 73 was used in the Ultrafast Point Designs.
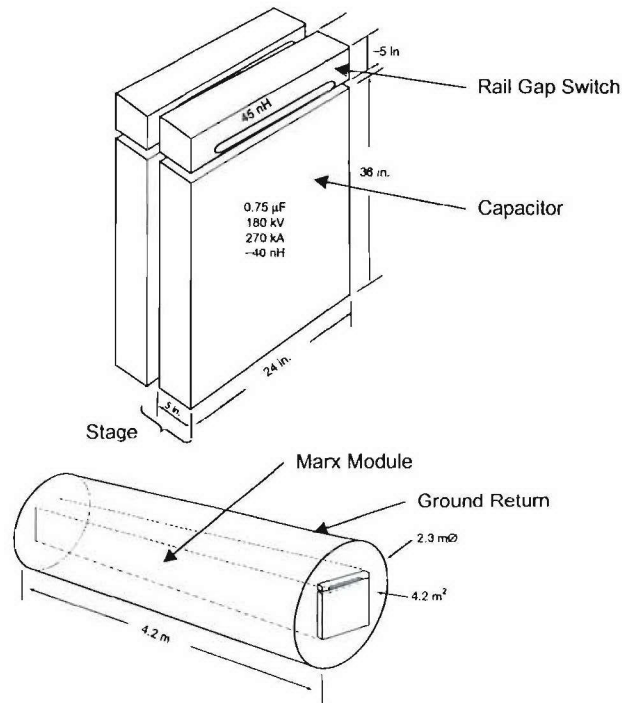
85

Figure 72. Concept for a $\sqrt{L \bullet C}$ = 300 ns stage and associated MGD.
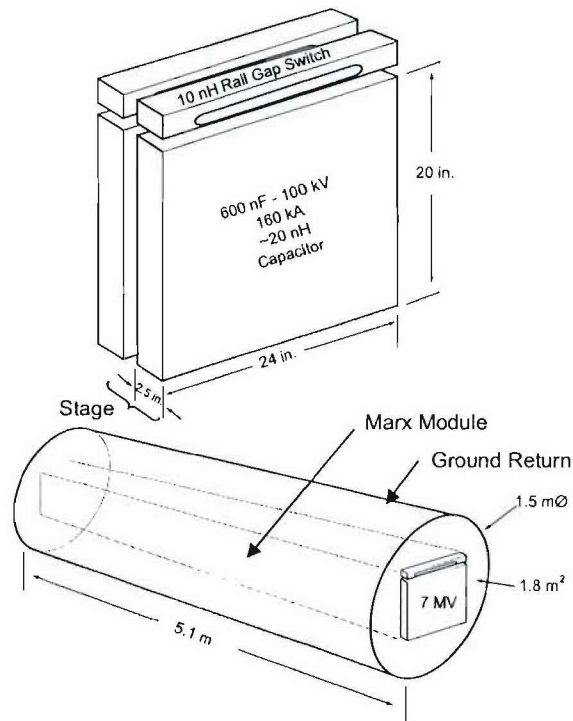

Figure 73. Concept for a $\sqrt{L \bullet C}$ = 175 ns stage and associated MGD.
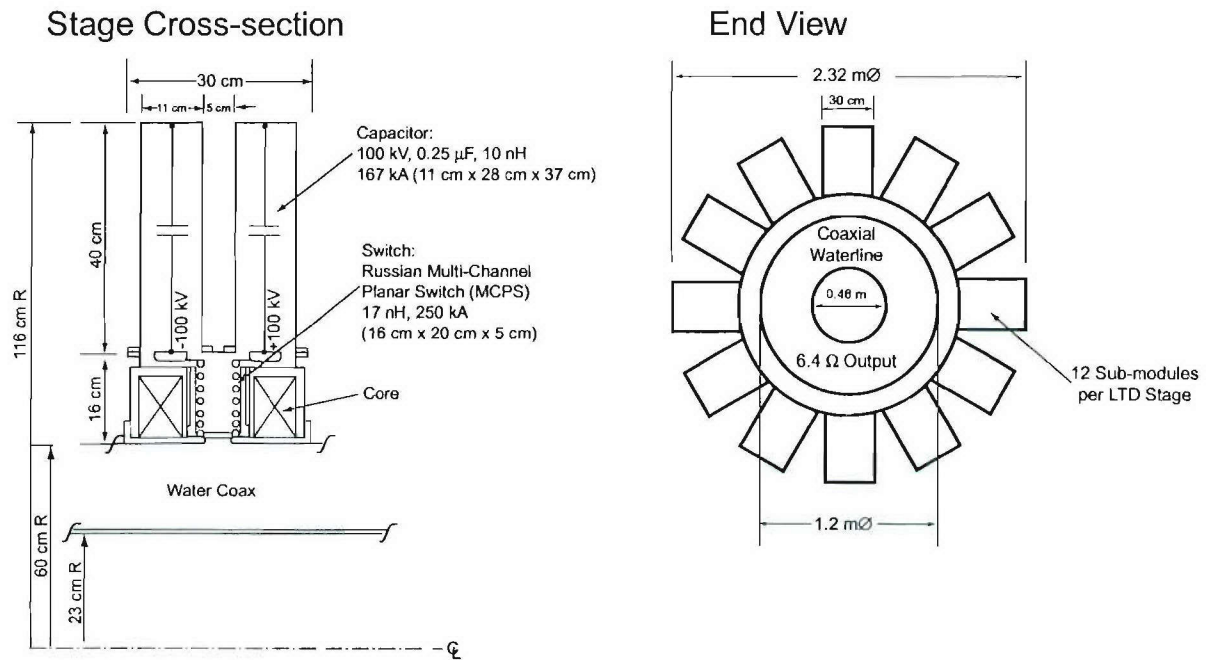
6.3 MGD STAGE TECHNOLOGY APPROACH.

The configurations of the two fast stage concepts above are similar. Both rely on the low inductance of multiparallel spark rail gaps and flat, wide capacitors with terminals compatible with direct low inductance attachment to the rail gaps. The principal difference is in the size and operating voltage affecting capacitance, inductance, and peak current capability. The smaller, lower voltage $\sqrt{L \bullet C} = 175$ ns stage has less capacitance and lower inductance, therefore lower $\sqrt{L \bullet C}$. One is a scaled version of the other, varied to meet different specific requirements. The rail gaps are adaptations of a design previously used in a lower power EMP pulser, TEMPS. Electrode size and spacings must be modified for the voltage, current and charge transfer here and suitable connections designed to mate with the stage capacitor. The capacitor is also specifically designed for this application. Its integration with the switch is a principal design determinant. The capacitor is comprised of windings (the capacitance), internal connections, case and terminal. In the two examples shown the windings are derived directly from those used in standard 3 µF/100 kV units and from ACE-FASTCAP 1.5 µF/180 kV units. What is done to produce the new capacitors is essentially to use a different quantity of the same winding elements (or pads) in a flat pack case consistent with the rail gap base size. This wider, narrower case reduces capacitor and configuration inductance. The capacitor terminal is a significant feature of this design. It is also wide, for low inductance, with very close spacings inside and outside the capacitor, to achieve minimum inductance in a structure which integrates directly with the rail gap, minimizing switch connection inductance. These features appear feasible but will require design and test.

6.4 FAST LTD.

The parameters of the ultrafast ($\sqrt{L \bullet C} = 175$ ns) LTD concept discussed in Section 3 were chosen based on the system analysis scans for driving 100 kJ/250 ns implosions. Sectional views of that conceptual LTD stage configuration are repeated here in Figure 74. The concept design is based on reasonable extensions of present component technology.

As in the ultrafast MGD stages, the capacitors derive from repackaging of windings used in standard 3µF/100 kV energy storage units. The case design is specific to the LTD application and constructed to form part of the inductive cavity. It is externally flanged to permit removal without dismantling the remainder of the stage. The output terminal is a high stress design with large transverse dimensions for low inductance.

This capacitor terminal is a "plug-in" fit with its associated spark gap. The spark gap in turn is a "plug-in" unit accessible when the capacitor is removed. The switch is a scaled version of the Kovalchuk multi-channel planar switch with its length increased for the voltage and width extended for lower inductance and increased peak current capability. The approximate scaling is from a 7 gap x 10 channel array to 10 gaps x 20 channels. The shorted turn inductance isolation is achieved conventionally with Metglas or iron cores. The stage concept shown is actually two series stages which share a part of the inductance associated with output feed interface volume, thereby reducing total inductance and number of discrete stages. The plus-minus charging also results in a higher voltage per unit length of the LTD, reducing the axial length per megavolt.

Stage Cross-section

30 cm

11 cm · 5 cm

116 cm R

40 cm

-100 kV   -100 kV

16 cm

Core

Capacitor:
100 kV, 0.25 µF, 10 nH
167 kA (11 cm x 28 cm x 37 cm)

Switch:
Russian Multi-Channel
Planar Switch (MCPS)
17 nH, 250 kA
(16 cm x 20 cm x 5 cm)

Water Coax

60 cm R

23 cm R

₵L

End View

2.32 mØ

30 cm

Coaxial
Waterline

0.46 m

6.4 Ω Output

1.2 mØ

12 Sub-modules
per LTD Stage

Figure 74. 200 kV/Stage, $\sqrt{L \bullet C}$ = 175 ns, water-insulated LTD concept.

SECTION 7
RECOMMENDATIONS

Our approach of constructing Point Designs succeeded in identifying several areas where research is needed to optimize simulator design. We list the following specific issues that a research program for advanced simulators should address before an optimum design can be selected.

7.1   REQUIREMENTS DEFINITION.

Much discussion in developing Point Designs revolved around questions about the requirements. In order to select a design, the simulator builder needs clear guidance on:

- Fluence-area requirements
- Spectral content
- Temporal constraints
- Acceptable debris environment
- Delivery schedule
- Shot rate
- Cost
- Priority of each requirement.

Having specifications for the needed capabilities will enable the designers to proceed. The best example of where these specifications are required is the trade analysis to select between four modular and one monolithic source. Simulator builders can provide input based on testing experience, but DTRA must make the call on the requirements issue.

7.2   SOURCE MODEL VALIDATIONS.

Experimentally determining krypton k-shell yield scaling with current and implosion time will reduce the factor of two uncertainty in the required current the drivers are required to provide. Reducing the factor of two uncertainty to a $\pm15\%$ band by radiation source experiments and analysis will enable the process of evaluating point designs.

7.3   DEBRIS REDUCTION/MITIGATION.

Along with requirements for the debris environment, research into the limits imposed by technology for reducing debris is required to develop a more capable simulator. Improvements in debris reduction and mitigation should translate directly into reductions in the pulse power driver requirements.

7.4   VACUUM INDUCTANCE LIMITS.

The pay-off in reducing vacuum inductance from 24 nH to 8 nH was illustrated in Figure 14 (70 MJ versus 45 MJ stored) for the 400 kJ/250 ns case. At a nominal cost of $2M/MJ, investing

in reducing front-end inductance can save significant cost. Testing schemes to minimize vacuum inductance on existing simulators should be very cost effective. Specifically, the degree to which the JCM limits can be exceeded and the effect of vane-type convolutes deserves attention.

## 7.5 PULSE FORMING LINE SWITCHES.

During the discussion of the MGD-Transfer Capacitor and MGD-Peaking Capacitor configurations, the inductance of the switches in the pulse forming lines became a limiting parameter. DTRA should experimentally establish the limits and investigate any innovative approaches. This research area could also have an impact on SNL simulator programs.

7.6 FAST COMPONENTS FOR MGD AND LTD.

Developing and demonstrating capacitor-switch stages with $\sqrt{L \bullet C}$ <175 ns will enable affordable designs for the MGD-Schlitt Line and LTD Schlitt Line configurations. These designs are not feasible at the current $\sqrt{L \bullet C} \approx 500$ ns state-of-the-art. The penalty extracted in only extending the state-of the art to $\sqrt{L \bullet C} \approx 300$ ns is illustrated in Figure 10 where the required Marx energy increases from 65 MJ at $\sqrt{L \bullet C} = 175$ ns to 165 MJ at $\sqrt{L \bullet C} = 300$ ns. For the high pay-off "Direct–Drive" designs, developing $\sqrt{L \bullet C}$ <175 ns stages is a very high priority. A review of existing driver components and evaluation of fast driver performance requirements has resulted in conceptual designs for faster Marx and faster LTD stages where the components result from extensions of existing capacitors and switches.

The recommended development adapts and extends the present state of the art to produce components which are specific to fast drivers. This progression is shown in Figure 75. The spark gap switch and capacitor representing the state of the art are typical of many large Marx drivers and have served contemporary applications well. However, even in an optimally configured stage comprised of these components, with an inductance of ≈ 250 nH and capacitance of ≈ 1 μF, the characteristic time is $\sqrt{L \bullet C} \approx 500$ ns. Times like 300 to 150 ns can be achieved by significant reductions in switch and capacitance inductance and by lowering stage capacitance. A feasible approach to this is to use rail-gap switches or to adapt the emerging multichannel spark gap technology pioneered at HCEI by Kovalchuk et al. Rail gap switches have been used in capacitor banks (e.g., SHIVA, CHECMATE) and in Marx generators (TEMPS, ACE 1 and 2) for their low inductance in high current applications.

The need here is to re-engineer them for fast driver applications with specific operating voltage, triggerability and current and charge transfer requirements. Since switch to capacitor connection inductance is often significant, the switch and capacitor combination must be developed together. Integration of these stage components is needed to obtain maximum performance. Typical conventional spark gaps are about 100 to 150 nH with as much as 50 nH connection inductance. Rail gaps or multichannel planar switches (MCPS) have 10 to 20 nH and connection inductance can essentially be eliminated by attaching directly to the capacitors.
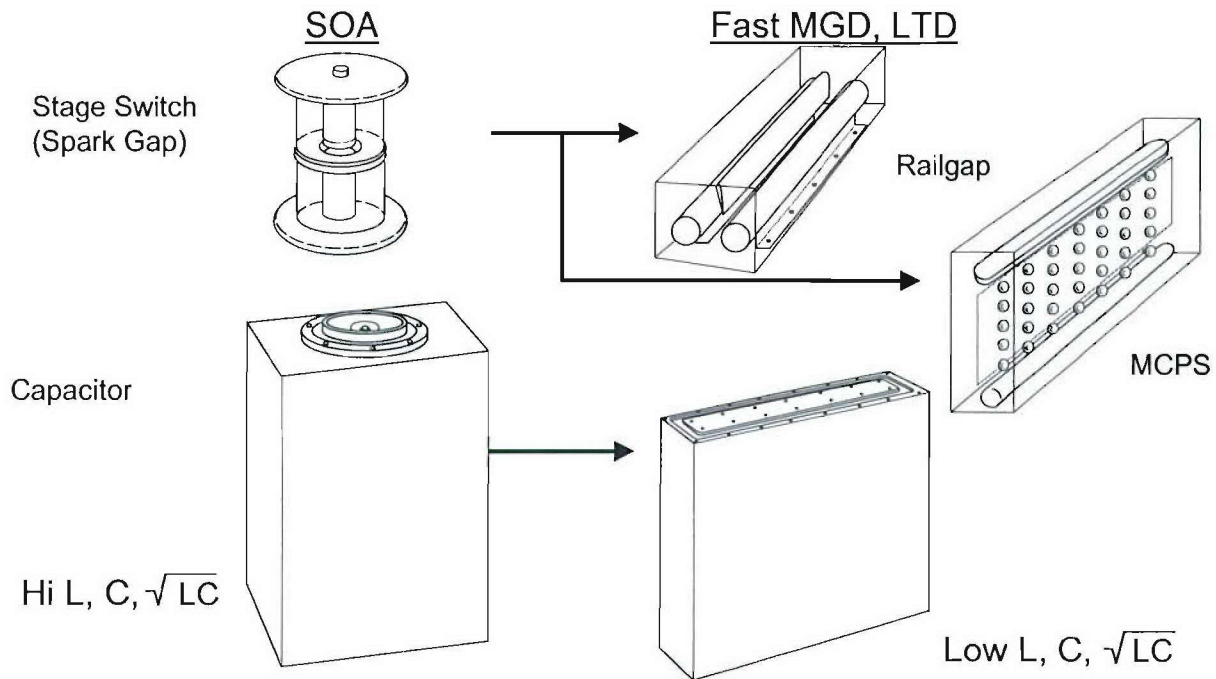
Figure 75. Component development for fast drivers.

Capacitor inductance is a result of internal conductor configuration in the windings (the energy storage elements) and in the terminal connections. The terminal usually constitutes the bulk of the inductance (e.g. $\approx$25 nH versus $\approx$ 5 nH for the windings) in a conventional low inductance capacitor. Therefore the biggest gain would result from new specialized terminal designs.

Present terminal designs are conservative and simplified to avoid special high voltage insulation considerations. By changing from a large aspect ratio coaxial terminal to wide, closely spaced, parallel connections compatible with wide rail gaps, terminal inductance can be lowered appreciably. The challenge then is to produce adequate, reliable high voltage insulation in the low inductance design.

The results of this component development would enable building the fast Marx drivers shown in Figure 76. Two drivers are implied here having different characteristic times; 300 ns (fast) for indirect (transfer capacitor) drive and 175 ns (ultra-fast) for direct drive. While there is one basic configuration, the capacitor and switch size and current capabilities differ as does the energy per stage. By engineering specific parameters a family of components can be produced to cover a range of application requirements. In the configuration shown, low inductance results from making the current path through capacitor and switch wide and short and with a close fitting ground return.
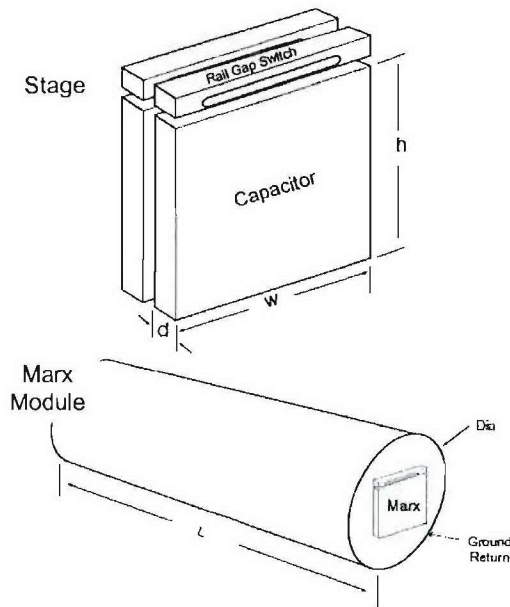
$\sqrt{LC}$	175 ns	300 ns
V_{STAGE}	100 kV	180 kV
C_{STAGE}	600 nF	750 nF
L_{CAP}	20 nH	40 nH
L_{GAP}	10 nH	45 nH
I_{STAGE}	160 kA	270 kA
W_{STAGE}	3 kJ	12 kJ
Dimensions		
d	2.5 in	5 in
w	24 in	24 in
h	20 in	36 in
dia	1.5 m	2.3 m
L	5.1 m	4.2 m

Figure 76. Fast Marx driver stages ($\sqrt{LC}$ = 175 ns, 300 ns).

Similar components may be used in the LTD concept shown in Figure 77. The LTD stage in this concept is + to − charged to double the stage voltage and 12 capacitor-switch sets are used to produce a stage impedance matching the coaxial output line. Wide, flat capacitors reduce inductance due to the capacitor and shorten the axial length of a stage and therefore the overall driver length. Multichannel planar switches are shown. These are flat and thin with wide transverse dimensions to couple directly to the capacitors and the output port with low inductance. Rail gaps could also be used. In this concept the capacitors are mounted externally and their cases become part of the stage cell wall conductor. Capacitors can be exchanged for maintenance without dismantling the entire assembly. Similarly the switches are plug-in modules, removable when a capacitor is removed.

The development of these components is necessary to enable faster drivers for smaller, more efficient systems. Development efforts would also provide insights on cost, reliability, and operation issues. Performance tests would show achievement of inductance and speed goals in simulated driver stage configurations.

7.7 PULSED POWER DRIVER DEMONSTRATIONS.

Sub-scale demonstrations represent the best approach to validate the point design assumptions and validate the pulsed power component and vacuum inductance developments. Demonstrations are recommended on two levels:

- Perform MGD and LTD demonstrations at the bank level involving ≈ 5 stages.
- Demonstrate bank performance/validate vacuum power flow assumptions at 5 MA level.
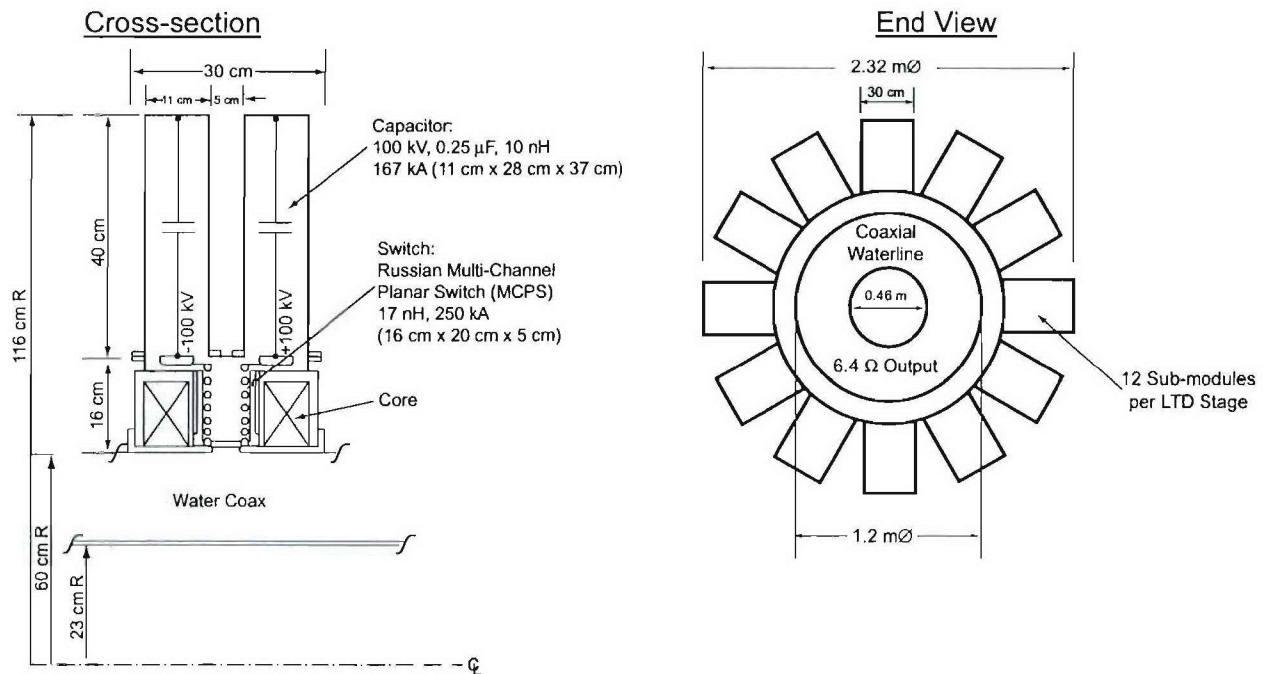
Figure 77. Ultrafast (125 ns) stage concept for LTD.

Completion of these demonstrations should minimize the risk associated with building a simulator at the 35 MA or higher level.

7.8   VACUUM POWER FLOW POWER MULTIPLICATION.

The vacuum power flow power multiplication concepts present in Section 5.2 represent breakthrough approaches that could reduce the cost of 400 kJ krypton simulators by factors of 5 or more. There is too much technical risk associated with any of these approaches to enable even a point design now, but the potential high payoff justifies a parallel program to investigate the feasibility of all of these approaches. A program focusing on modeling and sub-scale experiments until physics issues are resolved is recommended.

SECTION 8
REFERENCES

1. P. Sincerny, et al., "Concepts for an affordable high current imploding plasma generator," *Proceedings of the 12ᵗʰ IEEE International Pulsed Power Conference*, pp. 479-483, 1999. (UNCLASSIFIED)

2. D. Mosher, N. Qi, and M. Krishnan, "A two-level model for K-shell radiation scaling of the imploding Z-pinch plasma radiation source," *IEEE Trans. Plasma Sci.*, vol. 26, pp. 1052-1061, June 1998. (UNCLASSIFIED)

3. R. Grandey, et al., "Advanced Simulation Technology Program", DNA-TR-87-195, Maxwell Laboratories, Inc., San Diego, CA, 13 June 1987. (UNCLASSIFIED)

DEPARTMENT OF DEFENSE

DEFENSE TECHNICAL
INFORMATION CENTER
8725 JOHN J. KINGMAN ROAD,
SUITE 0944
FT. BELVOIR, VA 22060-6201
2 CYS   ATTN: DTIC/OCA

DEFENSE THREAT REDUCTION
AGENCY
8725 JOHN J. KINGMAN ROAD,
STOP 6201
FT. BELVOIR, VA 22060-6201
2 CYS   ATTN: TDNA/R. DAVIS

DEPARTMENT OF DEFENSE CONTRACTORS

ITT INDUSTRIES
ITT SYSTEMS CORPORATION
1680 TEXAS STREET, SE
KIRTLAND AFB, NM 87117-5669
2 CYS   ATTN: DTRIAC
          ATTN: DARE

TITAN CORPORATION
2700 MERCED STREET
SAN LEANDRO, CA 94577-0599
          ATTN: P. SPENCE